Development of Improved Materials for Continuous Steel Hot-Dipping Processes

Final Technical Report

Submitted in fulfillment of contract for

DOE Project Award Number

DE-FC36-01ID14042

Period Covered by Project
April 1, 2001 – June 30, 2005

List of Tables

List of Figures

Table of Contents

1. Project Administration and Contacts

Recipient Organization:

West Virginia University Research
Corporation
886 Chestnut Ridge Road
Morgantown, WV 26506

Technical Point of Contact:

Carl Irwin (Administration PI) West Virginia University (304) 293-7318 ext. 5403 Carl.Irwin@mail.wvu.edu	Ever J. Barbero (Technical PI) West Virginia University (304) 293-3111 ext. 2337 (voice) (304) 293-6689 (fax) Ever.Barbero@mail.wvu.edu

Research Partner:

Oak Ridge National Laboratory

Principal Investigator
Vinod Sikka, Ph.D.
Materials Processing
One Bethel Valley Road , P.O. Box 2008 MS6083
Oak Ridge, TN 37831-6083
(865) 574-5112
(865) 574-4357 Fax
sikkavk@ornl.gov

Research Organizations:

International Lead and Zinc Research Organization, Inc. Frank Goodwin, Sc.D. Vice President, Materials Science P.O. Box 12036 Research Triangle Park, NC 27709-2036 (919) 361-4647 x 3018 (919) 361-1957 Fax fgoodwin@ilzro.org	**Industries of the Future – West Virginia** Carl Irwin, Ph.D. WVU National Research Center for Coal & Energy West Virginia University P.O. Box 6064 West Virginia University Morgantown, WV 26506 (304) 293-2867 (304) 293-3749 Fax Carl.Irwin@mail.wvu.edu

Industry Participants:

Partner	Contact Information	Partner	Contact Information
AK Steel Corp.	Paul Janavicius (513) 425-2670 Paul_Janavicius@aksteel.com	Metaullics	Mark Bright (440) 349-8810 mabright@metaullics.com
Praxair Surface Technologies	Stephen Wichmanowski (317) 240-2699 Stephen_Wichmanowski@praxair.com	California Steel Industries Inc.	John Wray (909) 350-6165 jwray@californiasteel.com
Duraloy Technologies Inc.	Roman Pankiw (724) 887-5100 techmgr@duraloy.com	Teck Cominco	Keith Zhang (905) 822-2022 x265 keith.zhang@teckcominco.com
Vesuvius McDaniel	Edward Dean (724) 843-8300 ext. 269 Ed.dean@vesuvius.com	ASB Industries	Charles Kay (330) 753-8458 cmkay@asb-ind.com
Deloro Stellite	Jim Wu (314) 983-0266 jwu@stellite.com	Ellison Surface Technologies	
ILZRO	Frank Goodwin (919) 361-4647 ext. 3018 fgoodwin@ilzro.org	Nucor – Berkeley, SC	Allen Rogers (843) 336-6448 rogersa@nucorsteel.com
Weirton Steel Corp.	Brian Lester (304) 797-3993 brian.lester@weirton.com	Wheeling Nisshin Steel Corp	Frank Mollica (304) 527-4893 FrankM@wheeling-nisshin.com
Fontaine Engineering	Andres Gast-Brey (304) 842-8718 agb@foen.com	Stoody Company	Ravi Mennon (270) 781-9777 x2009 ravi_menon@thermadyne.com

2. Restrictions and Limitations

Acknowledgements

This material is based upon work supported by the U.S. Department of Energy under award number DE-FC36-01ID14042.

Disclaimer

Any opinions, findings, and conclusions or recommendations expressed in this material are those of the author(s) and do not necessarily reflect the views of the Department of Energy.

Patented Material

Sub-task 4.3.1 details a novel roll and bearing design for a stabilizer roll and is pending patent approval according to U.S. Patent Pending,# 0/695551-102803. “Bearing Life Extender for Conveyor Type or Zinc Pot Roll”.

3. Executive Summary

The process of continuous galvanizing of rolled sheet steel includes immersion into a bath of molten zinc/aluminum alloy. The steel strip is dipped in the molten bath through a series of driving motors and rollers which control the speed and tension of the strip, with the ability to modify both the amount of coating applied to the steel as well as the thickness and width of the sheet being galvanized. There are three rolls used to guide the steel strip through the molten metal bath. The rolls that operate in the molten Zn/Al are subject to a severely corrosive environment and require frequent changing. The performance of this equipment, the metallic hardware submerged in the molten Zn/Al bath, is the focus of this research. The primary objective of this research is to extend the performance life of the metallic hardware components of molten Zn/Al pot hardware by an order of magnitude.

Typical galvanizing operations experience downtimes on the order of every two weeks to change the metallic hardware submerged in the molten metal bath. This is an expensive process for industry which takes upwards of 3 days for a complete turn around to resume normal operation. Each roll bridle consists of a sink, stabilizer, and corrector roll with accompanying bearing components. The cost of the bridle rig with all components is as much as $25,000 dollars just for materials. These inefficiencies are of concern to the steel coating companies and serve as a potential market for many materials suppliers. This research effort served as a bridge between the market potential and industry need to provide an objective analytical and mechanistic approach to the problem of wear and corrosion of molten metal bath hardware in a continuous sheet galvanizing line. The approach of the investigators was to provide a means of testing and analysis that was both expeditious and cost effective. The consortium of researchers from West Virginia University and Oak Ridge National Laboratory developed several test apparatuses that were designed to work in concert so that the process of developing and evaluating new materials and material combinations could be carried out in the most effective manner.

ORNL focused on the long-term effects of static and dynamic corrosion on the hardware. Their efforts have yielded corrosion data in terms of mass loss for a large database of materials for immersion times in excess of 6000 hours. In addition, they have developed a new series of alloy, designated ORNL Alloy 4-x. Several variants of Alloy 4 were tested for corrosion and wear performance. Another effective method for protecting bearing components is through the use of weld overlays or laser cladding. ORNL worked with several project partners to develop a weld overlay process for cladding of 316L stainless steel with metallic materials that are much more corrosion and wear resistant. This method provides super-alloy performance that is more affordable.

WVU was tasked to study wear of the bearing materials along with mechanisms of dross buildup on the roll surface. A small scale screening test apparatus was developed for the purpose quickly evaluating wear performance of candidate superalloys, ceramics, and coatings through the use of a ball-and-seat testing combination. This combination uses a fraction of the material used in full-scale bearing applications. With this system, WVU has been able to conduct hundreds of tests on various combinations of

materials that mimic a wide variety of operating conditions for the galvanizing lines. The small scale wear tester was used to perform both direct correlation to galvanizing line conditions and to act as a screening mechanism for prototype-scale testing at WVU's airport bearing materials testing facility. In addition, the studies on the effect of contact pressure and velocity on the bearing wear rate lead to the design and subsequent patent application for a fixed-shaft roll design that has the potential for increasing the bearing life by a factor of 2. The prototype-scale bearing test apparatus was donated by one of our project partners and was relocated to the WVU airport hanger at Morgantown Municipal Airport. This test apparatus uses full-scale sleeve and bushing dimensions and is designed to more accurately mimic the galvanizing line conditions.

Through the combination of corrosion, wear, and dross buildup testing, as well as material modeling and thermodynamic analysis, the research team has been able to show that an order of magnitude improvement in material performance is a realistic goal.

Component line trials are a culmination of research performed in the IMPH project to study the mechanisms of wear, corrosion, and dross buildup on materials tested under laboratory scale conditions at WVU and ORNL. From small-scale and prototype-scale testing, wear and corrosion measurements of various candidate materials have been made. WVU, ORNL have worked with steel partner A to conduct the trial of Supplier A 2012 XT bearings as the sink roll and stabilizer roll bearings. There have been 8,034,724 feet of steel strip passed through the galvanizing bath during the trial, which is more than twice of the conventional Stellite 6 bearing's service life. The detail examination of the Supplier A bearing shows that only less than 1/3 of the total thickness of the 2012 XT bearing was worn after the trial, as compared to the Stellite 6 bearings were totally worn through after one campaign, which means that the bearing can be re-used two more times, to triple the service life of the bearing. Therefore, it is safe to conclude that as one of the results of this IMPH project, the newly 2012 XT bearings have at least six times of the service life than the conventional Stellite 6 bearings.

Life improvement of molten metal bath hardware in continuous galvanizing lines is projected to result in an extension of component life by an order of magnitude and estimated energy savings of 2 trillion BTU/year and cost savings of approximately $46 million/year for the 57 galvanizing lines operating in the United States.

4. Summary of proposal objectives and goals

The original proposal for this work outlined a single primary goal: To develop new bulk materials and surface treatments/coatings for life improvement of molten metal bath hardware in continuous galvanizing lines which result in an extension of component life by an order of magnitude and estimated energy savings of 2 trillion BTU/year and cost savings of approximately $46 million/year for the 57 galvanizing lines operating in the United States.

The process set forth in the proposal to achieve this lofty goal was broken down 11 conceptual objectives that needed to be understood:

1. Understanding of the current pot hardware systems
2. Materials Process Modeling
3. Wetting Behavior of Material Surfaces
4. Super Meniscus Intermetallic Climb (SMIC)
5. Corrosion Resistance in Static and Dynamic Bath Conditions
6. Wear Resistance in Molten Bath Environment
7. Alloy Design
8. Coatings
9. Mechanical Properties
10. Manufacturability and Reparability of Monolithic or Coated Materials
11. Identification of Monolithic Ceramics or Ceramic-Ceramic Components.

The research plan that was developed based on the need to explore these 11 concepts and the following research plan and subsequent work task breakdown was developed:

Task 1 Failure Analysis and Materials Characterization

This task consisted of two components:

1. Industrial survey submitted to the steel industry partners will be taken in order to assess the current state of the industry in terms of materials selection and typical line management practices
2. Industrial partners will submit spent hardware from the galvanizing lines and the research team will perform a failure analysis in order to determine failure mechanisms

Task 2 Materials/Process Modeling

Thermodynamic data will be used to predict the phase formation at the substrate/liquid interface. A new set of experimental thermodynamic data will need to be generated for some of the molten metals of concern in this proposal. The thermodynamic phase predictions will be verified by coupon testing in the laboratory. Materials and modeling predictions along with the data from Task 1 will become the basis for alloy and coating design.

Task 3 Materials Development

Two types of materials will be developed: Bulk materials for hardware such as sink and stabilizer rolls and coatings for bearings and other surfaces more resistant to corrosion and wear conditions.

Task 4 Corrosion and Wear Testing/Analysis

This task will deal with corrosion and wear measurement of bulk materials and coatings for both existing materials used commercially and for newly developed materials stemming from Task 3. Corrosion testing will be carried out in two steps: static and dynamic in both laboratory and in-plant molten metal baths. Wear testing will be carried out on small-scale material specimens and a prototype scale 500 lbf zinc bath.

Task 5 In-plant Testing and Trials

The best performing materials based on static/dynamic corrosion and wear testing will be subjected to in-plant production line tests

Task 6 Meetings and Technical Reports

There will be at least two technical review meetings per year for the entire group of researchers and industrial partners. Quarterly and final reports will also be issued.

		Timetable for completion of project tasks/sub-tasks											
Task	**Activity**	Year 1				Year 2				Year 3			
		Q1	Q2	Q3	Q4	Q1	Q2	Q3	Q4	Q1	Q2	Q3	Q4
1	**Failure Analysis and Materials Characterization**												
1.1	Industrial Survey and review												
1.2	Failure analysis of spent pot hardware												
2	**Materials/Process Modeling**												
2.1	Thermodynamic and kinetics modeling												
3	**Materials Development**												
3.1	Bulk alloys												
3.2	Surface treatments/coatings												
4	**Corrosion and Wear Testing/Analysis**												
4.1	Coupon testing												
4.2	Lab scale dynamic testing												
4.3	Friction and wear testing												
5	**In-Plant Testing and Trials**												
5.1	Pilot scale materials testing												
5.2	Component testing												
6	**Meetings and Reports**												
6.1	Hold two technical meetings per year												
6.2	Complete final report												

Table 1: Proposal work breakdown

5. Summary of Project Activities

The basic structure of the proposal work breakdown and structure was followed without significant modifications. From the initial kickoff meeting with the research team and industrial partners, it was determined that materials developed by ORNL or submitted by the material suppliers be tested in three Series:

Series I. Existing materials and combinations used in commercial applications
Series II. New materials and combinations (monolithic)
Series III. New materials and combinations (coatings/treatments)

This breakdown will provide the industrial partners a significant database of baseline material data for the test rigs at WVU so as to better quantify the extension of material life that can be seen from new materials and process. Therefore, the amended work breakdown, which was also used to generate Form DOE F 4600.3A – Milestone Log, is listed below:

		Timetable for completion of project tasks/sub-tasks											
Task	**Activity**	Year 1				Year 2				Year 3			
		Q1	Q2	Q3	Q4	Q1	Q2	Q3	Q4	Q1	Q2	Q3	Q4
1	**Failure Analysis and Materials Characterization**												
1.1	Industrial Survey and review												
1.2	Failure analysis of spent pot hardware												
2	**Materials/Process Modeling**												
2.1	Thermodynamic and kinetics modeling												
3	**Materials Development**												
3.1	Series I - Existing Materials												
3.2	Series II - New monolithic materials												
3.3	Series III - New surface treatments/coatings												
4	**Corrosion and Wear Testing/Analysis**												
4.1	Series I-III Lab scale corrosion testing												
4.2	Series I-III In-plant dynamic corrosion testing												
4.3	Series I-III Friction and wear testing – Small Scale												
4.4	Series I-III Prototype scale wear testing												
5	**In-Plant Testing and Trials**												
5.1	Pilot scale materials testing												
5.2	Component testing												
6	**Meetings and Reports**												
6.1	Hold two technical meetings per year												
6.2	Complete final report												

Task 1 Failure Analysis and Materials Characterization

The objective of this initial task of the project was to assess the current state of the industry with regard to the types of materials used for pot hardware components, i.e. sink/stabilizer rolls, bearing sleeves, bushings, etc. In addition, the research team

solicited spent roll and bearing materials from the steel galvanizing industrial partners in order to perform a failure analysis, the intent of which was to drive the new material development in subsequent tasks.

Sub-Task 1.1 Failure analysis of spent pot hardware

The industrial partners generously donated a wide variety of spent pot hardware and dross samples from a wide variety of industrial conditions. Steel partner B donated stabilizer roll, completely intact, for use with this project. In addition, steel partner C, steel partner D, and steel partner A also donated spent bearing materials for visual inspection and microstructure analysis.

Dross formation on rolls

Early in the examination of pot roll materials, it became clear that dross buildup occurred in areas where the pot roll surface does not touch the strip. This is seen in the picture of a spent sink roll from steel partner D in Figure 1. Even small areas of non-contact between the strip and roll surface becomes a location where dross buildup occurs. For the failure analysis, the research team performed microstructure analysis on sections of the roll that were cut from the donated specimens (See

Figure 2). When buildup first occurs, the dross particles are isolated from each other by the surrounding liquid zinc. With time, additional dross particles build up and the roll surface changes to an area with increasingly less liquid zinc fraction. As dross particles build up upon each other the liquid fraction moves progressively outward to the new contacting surface. Cross sections of dross buildup on rolls that have been in service for a time thus show a completely solid layer of built up dross at the roll/dross interface. Moving outward toward the built up surface, the liquid fraction becomes increasingly higher, out to the roll surface where a dilute mixture of interconnected dross particles are mixed with the galvanizing alloy. This is the surface condition that steel strip sees when it passes over the pot rolls in areas of buildup – the dross particles in the semi-solid pot roll surface layer can occasionally break off and adhere to the strip surface, or compact and be more massive, depending upon local equilibrium conditions. This is shown graphically in Figures 2 and 3where bottom dross on both the sink and stabilizer rolls is apparent.

Two stabilizer rolls, one virgin and one spent, were donated for analysis by steel partner B, as can be seen in Figures 3 through 5. The spent roll was cut into pieces for analysis by the research teams at WVU and ORNL. Figures 6 through 8 show optical micrographs of the inner and outer diameters of the roll, along with specimens of dross adhered to the outside of the roll. Figures 9 through 12 show the SEM images of various faces of the spent roll.

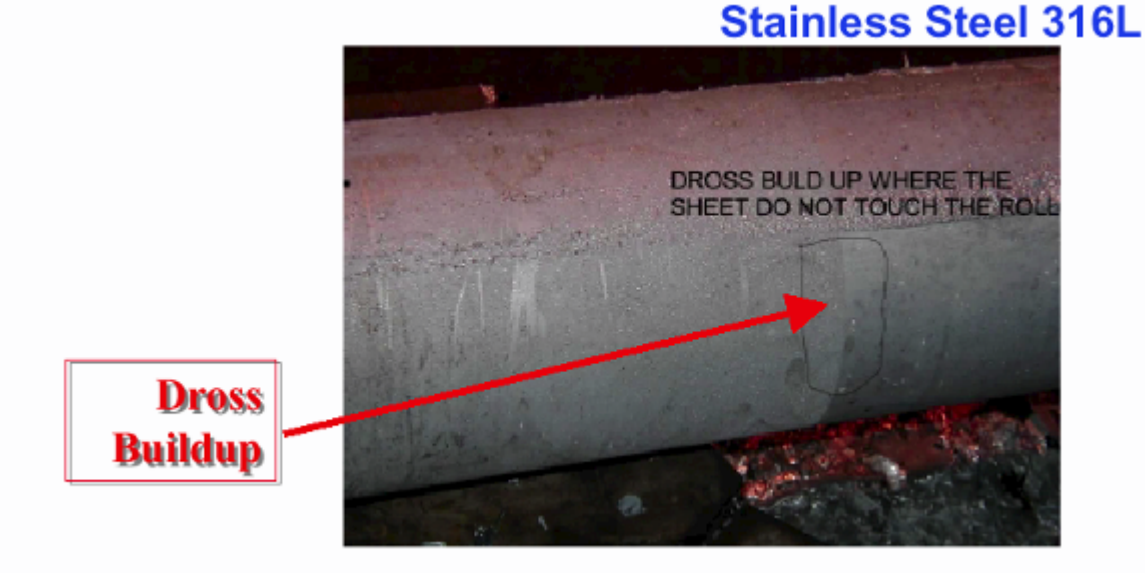

Figure 1: Roll surface showing the dross formation outside the steel strip region

Figure 2: Specimen of a sink roll from steel partner C

Figure 3: Stabilizer rolls from steel partner B

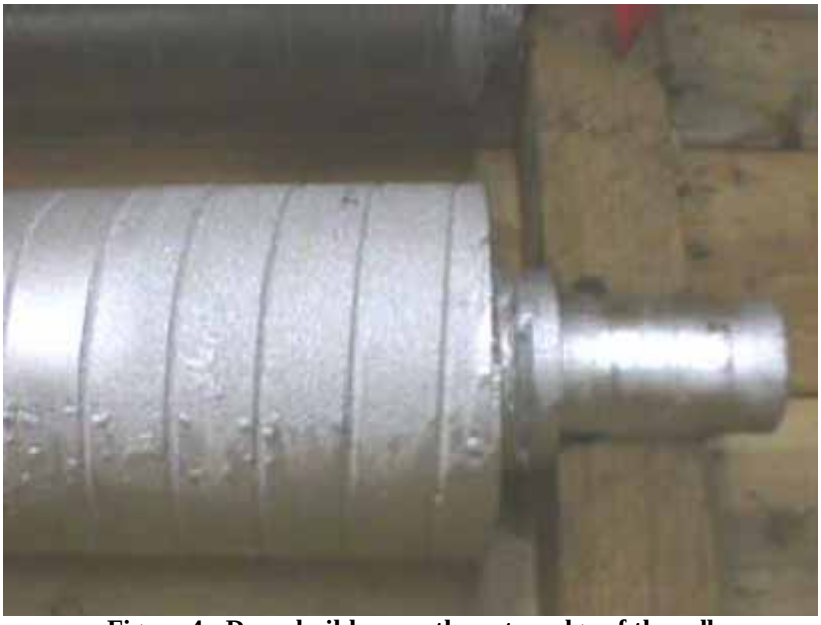

Figure 4: Dross build-up on the outer edge of the roll

Figure 5: Close up of dross formation

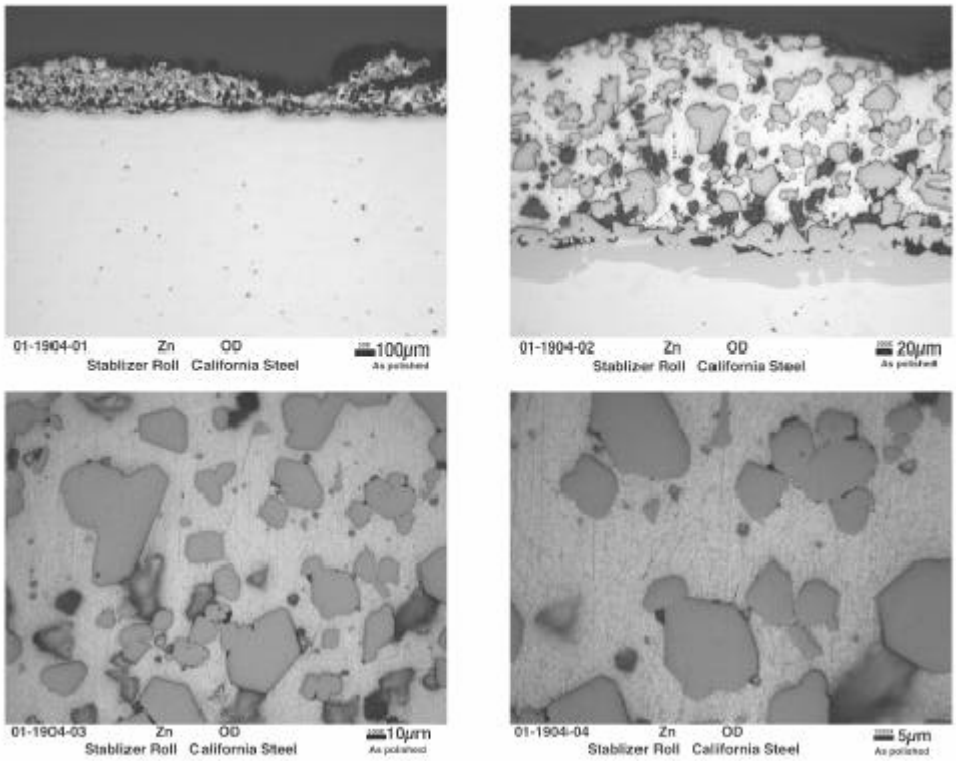

Figure 6: Optical Micrographs of Zinc Attack on the OD of Type 316L Stabilizer Roll Received from steel partner B

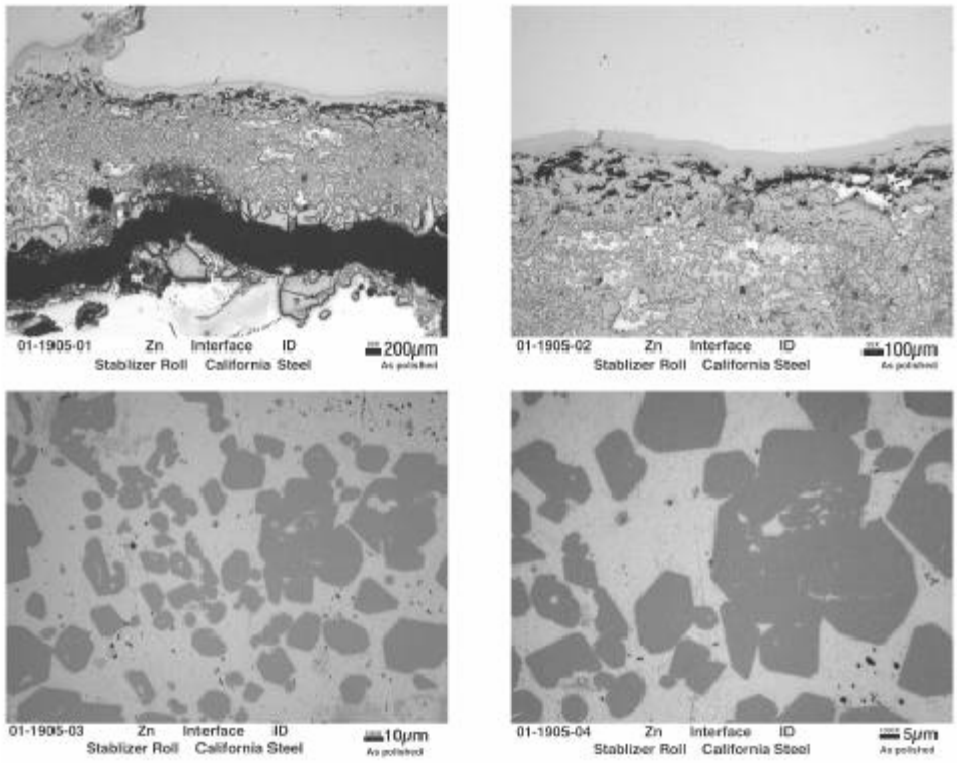

Figure 7: Optical Micrographs of Zinc Attack on the ID of Type 316L Stabilizer Roll Received from steel partner B

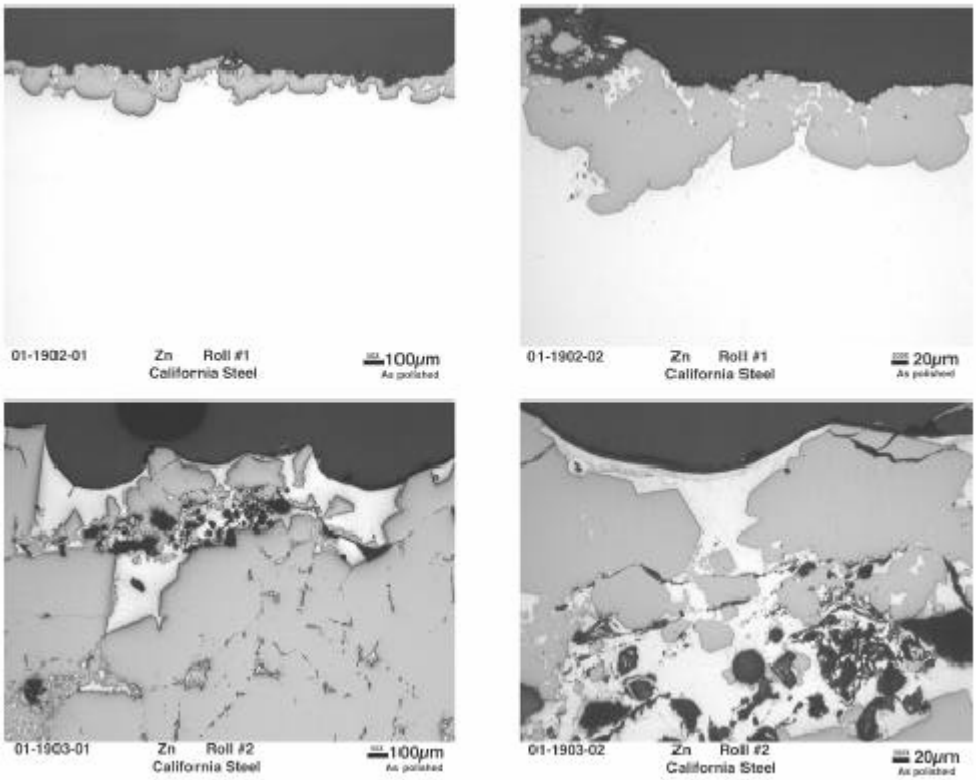

Figure 8: Optical Micrographs of Dross Removed from the Ends of the Two Type 316L Stabilizer Rolls

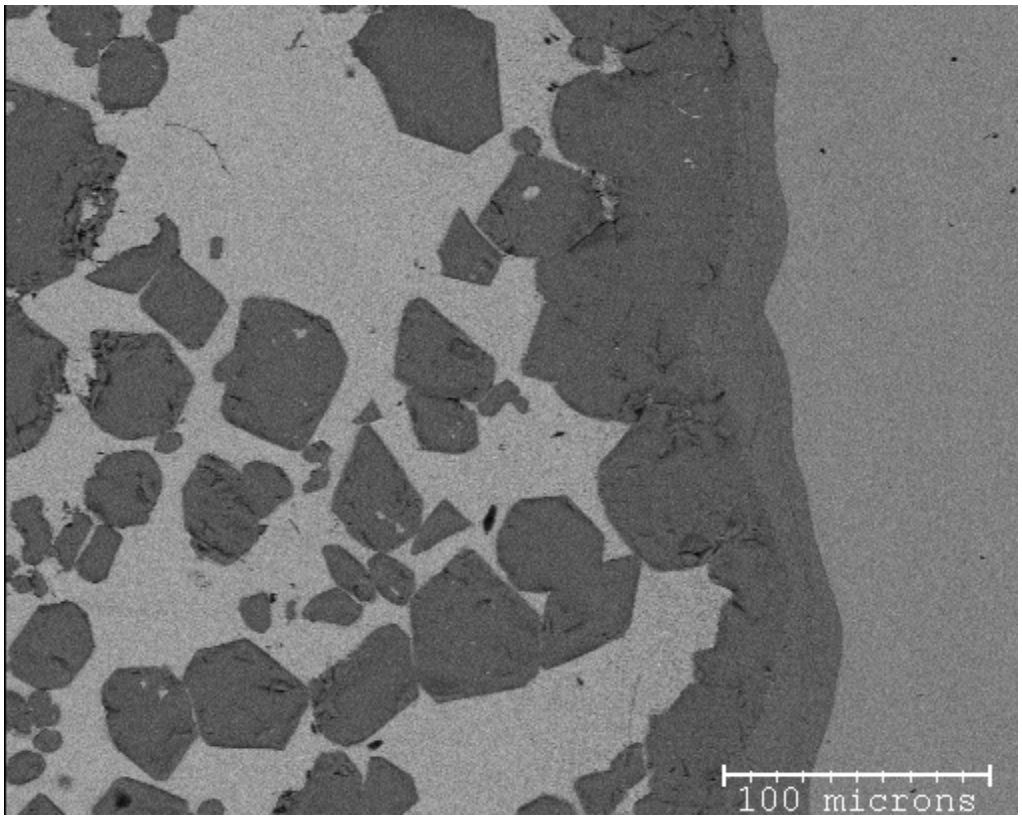

Figure 9: Dross Formation on the steel partner B stabilizer roll in a GI bath

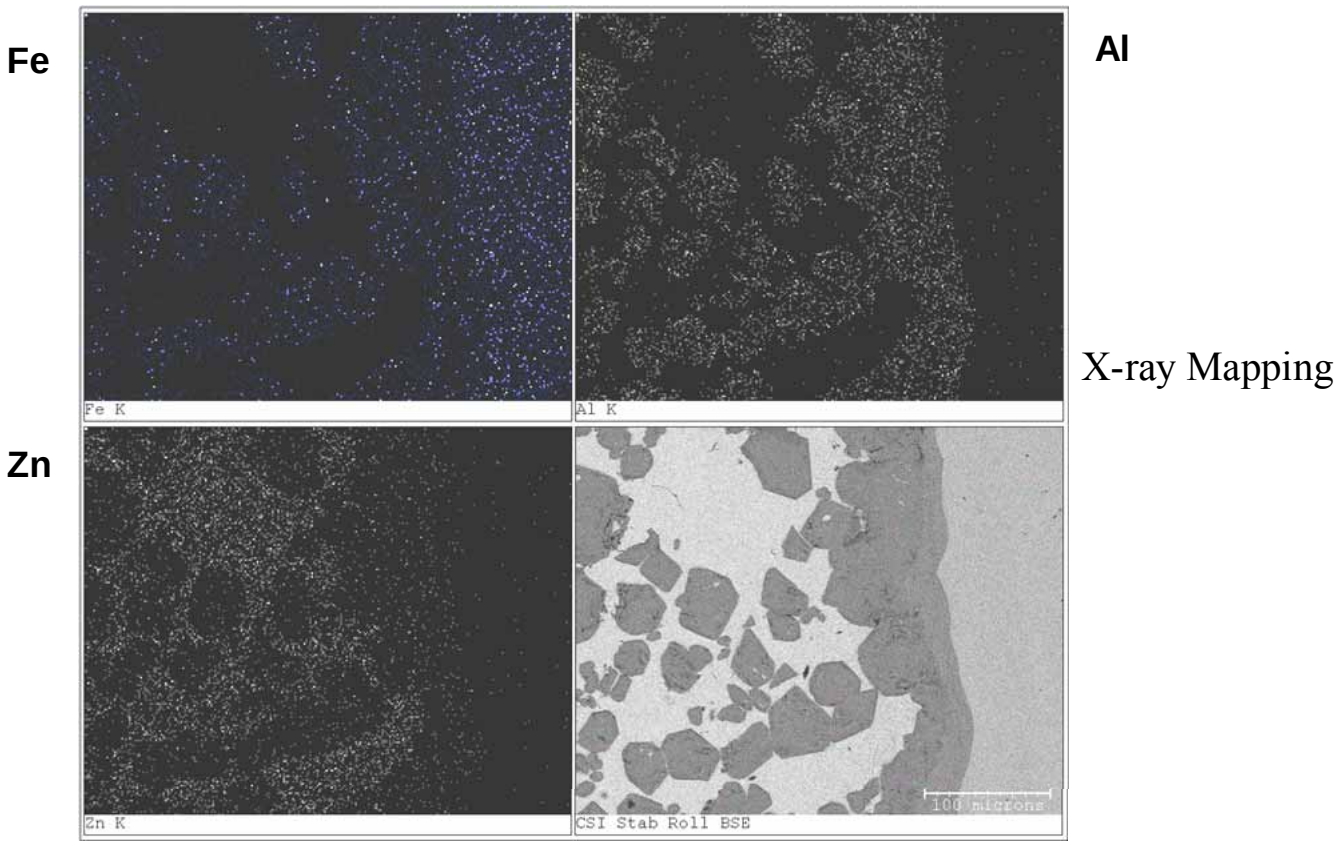

Figure 10: X-Ray Mapping of the Dross

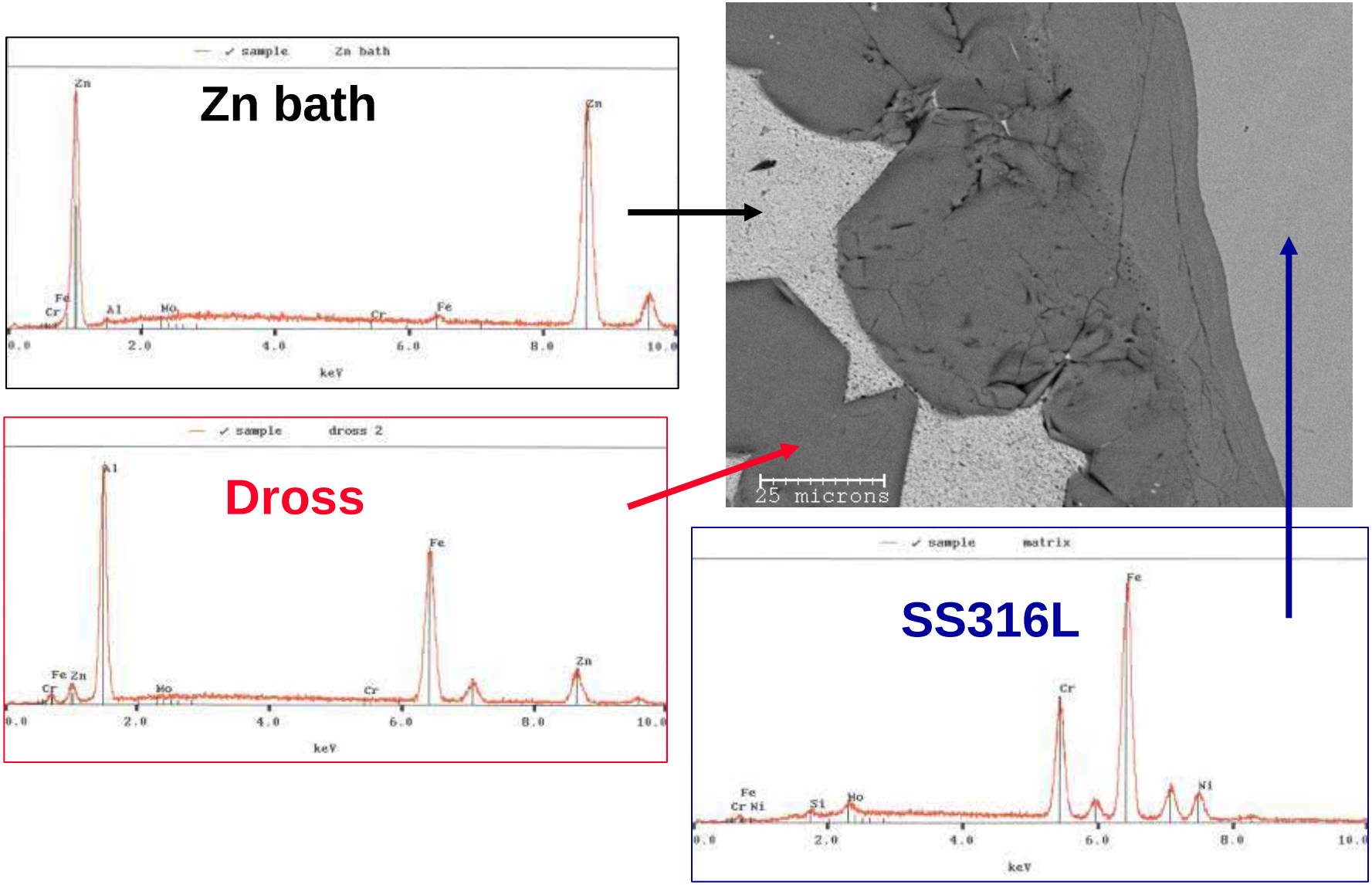

Figure 11: Phase Identification of the STEEL PARTNER B Roll with Dross

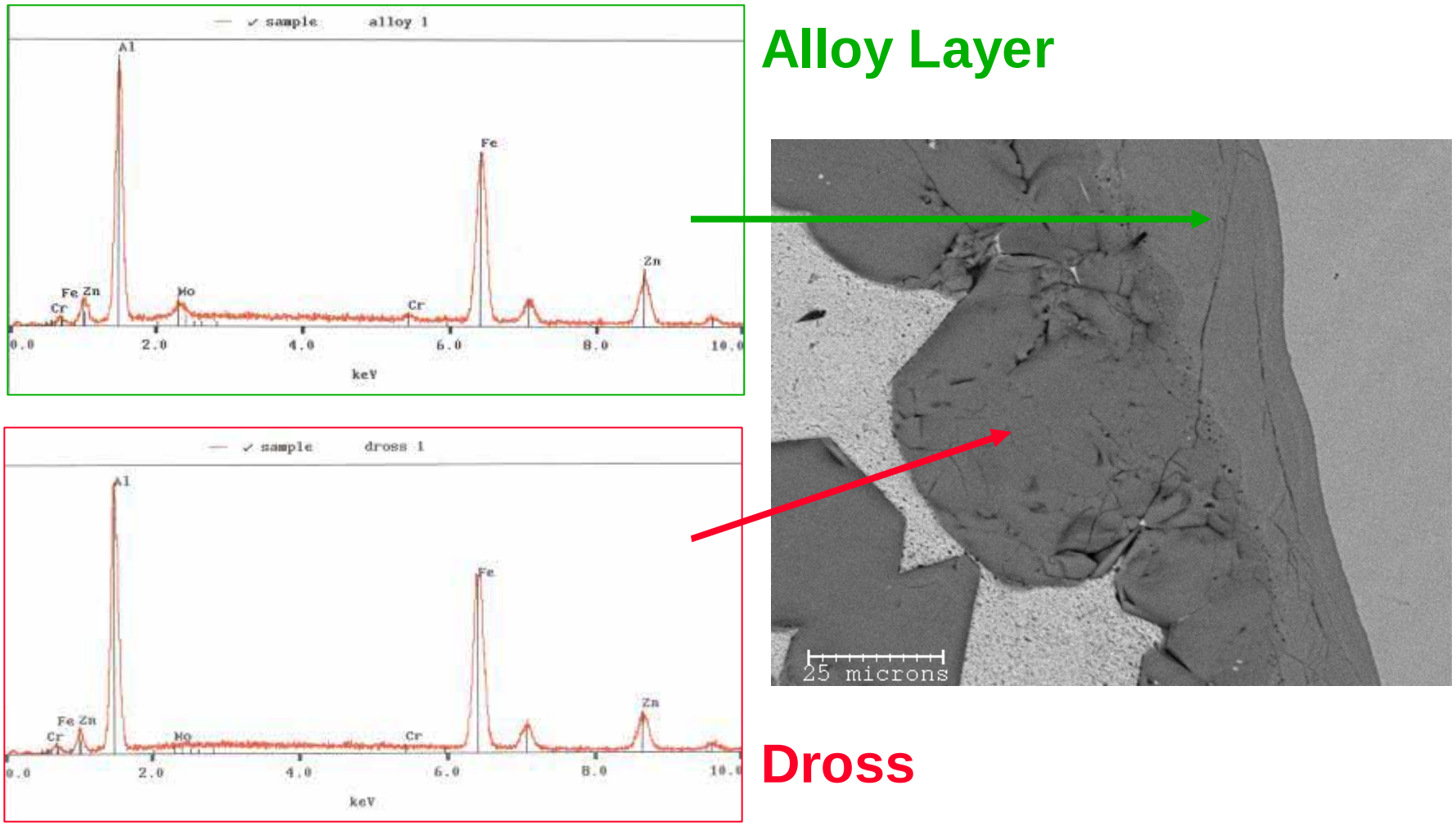

Figure 12: Corrosion Layer of the STEEL PARTNER B Roll

Wear of the journal bushing and sleeve components

Spent bearing components, stationary sleeves and rotating journal bushings, were submitted by several industrial partners for analysis. These materials show a variety of wearing conditions, which include abrasive, adhesive, and fatigue wear depending on the material and geometry used.

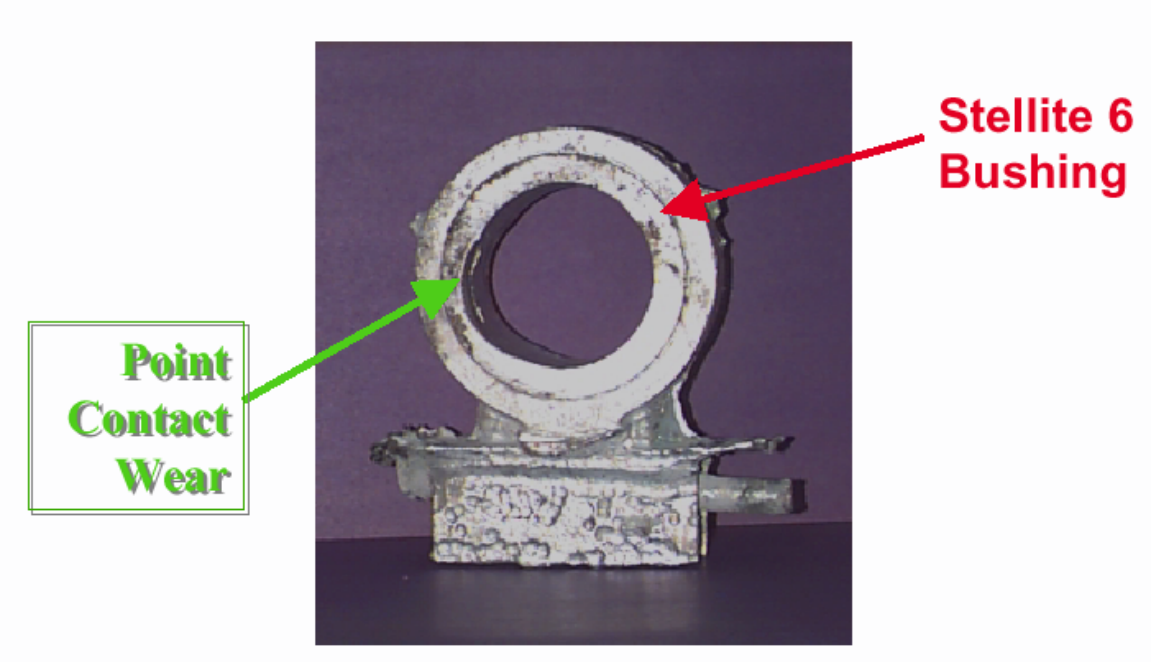

Figure 13: Spent Stellite 6 bushing from steel partner D

Sub-Task 1.2 Industrial Survey

In addition to the failure analysis of spent bushing and roll materials, a comprehensive and confidential industrial survey was conducted for commercial hot dip coating companies around the world. The research teams at WVU and ORNL partnered with the International Lead Zinc Research Organization (ILZRO) and Tech Cominco in Canada to refine and distribute their industrial survey on bearing designs for continuous sheet galvanizing of steel. In addition, a new survey on pot roll surface maintenance was developed and distributed to the industrial partners of this project, along with the worldwide network of companies that work with ILZRO. The results of the Pot roll surface maintenance survey are reported herein.

Survey on Pot Roll Surface Maintenance - ILZRO/WVU

Samples from 12 companies on 20 lines
N. America (15) others (5)

Same material and **Same** coating for sink roll and stabilizer rolls.

Roll Alloy: 316L S.S.
one company uses Resalloy without coating

Coating: Sink Roll	Yes (14)	No (6)
Stabilizer Roll	Yes (12)	No (8)

All use WC coating

Roughness specification	Yes (11)	No (9)
Polishing roll surface	Yes (3)	No (17)

one company with less dross buildup
Other two claim no difference

Groove specification	Yes (18)	No (2)

each company has its own design.

Dross removal
(10) Manual scraping
(9) Build-in devices
(9) Removal of roll

How often?
GI/GA roll check and scrape if there is dross buildup
no scrape until roll change (~2-4 weeks)
GL every weld (build-in devices)

Task 2 Materials and Process Modeling

A detailed literature review was carried out to determine the current use and selection of materials for galvanizing hardware. In this task, we also demonstrated a binary phase diagram-based material selection process and initial calculations using ThermoCalc™ modeling.

Literature review revealed that the poor quality of sink roll can lead to scratching of the strip. This can happen from: (1) roll not turning, (2) sink roll groove marks appearing on the galvanized strip, and (3) dross spots appearing on the galvanized strip. The most common materials used for sink and stabilizer rolls are of type 316L stainless steel and many use WC/Co-coated type 316L rolls.

In the last 50 years, little systematic work has been published on bath hardware materials performance. The following is a brief description from some of the key publications:

Imhoff (1943) used carbon steel of 0.45% C, 0.65% Mn, 0.04% P, 0.04% S, and 0.05% Si in the normalized and tempered conditions. He noted that with good continuous operating condition, rolls needed remachining every eight months.

Bablik (1950) found that Armco iron with low C and Si showed the lowest attack. He further noted that forged material was better than cast material. The major cause for Zn bath hardware deterioration was identified as overheating. Bablik noted that Fe dissolved in Zn linearly between 500 to 520ºC and parabolically below this temperature. A light controlled oxidation after machining was suggested to have beneficial effect for cast irons.

Munson (1970) investigated coatings of Titania, graphite paint, plasma-sprayed W, and torch-sprayed Ni-Cr, Ni-Cr-WC, and Co-Cr-W. He noted that the W-bearing coating was not wetted by the liquid Z and performed well. Iron-oxide scale on low Si ductile iron was investigated, but once scale was penetrated, breakdown occurred.

Michael and Young (1979) reviewed mechanisms of liquid Zn attack on stainless steels. They noted that dissolution of stainless steel in Zn was the prevailing mechanism. Zn diffusion into stainless steel occurred preferentially along the grain boundaries.

Terai and Kohno (1983) studied corrosion in molten Zn at 460ºC for 39 days. They found that 12Cr-18% Si steel performed well as sink roll.

Antony and Srivastava (1987) tested at 455ºC different stainless steels and Fe-N-Cr-Co alloys and made the following observations:

1. Types 316, 309, and 304 stainless steels underwent intergranular attack.
2. Haynes 556 (Fe-Ni-Cr-Co) showed small weight loss.
3. Haynes 188 (40% Co-22% Ni-22% Cr-10% W) also showed less weight loss than stainless steel.

Tomita et al. (1993) indicated that durability of WC/Co varies according to its powder preparation process. They used sprayed dried (SD) and sintered and crushed (SC) powders in their study. In the SD coating, the binder phase Co dissolved in molten Zn.

In the SC coating, the binder phases formed Co_3W_3C and Co_6W_6C and the coating microstructure did not change after 96 h.

Kurimoto et al. (1994) examined WC-125 Co in the sealed and unsealed conditions, and coatings such as Al_2O_3, $CaO\text{-}SiO_2\text{-}ZrO_2$, and $Al_2O_3\text{-}ZrO_2$. They found that HVOF coatings of WC-12% Co were somewhat better than plasma-sprayed. Furthermore, the sealed coatings of WC-12% Co and Al_2O_3 were not wetted by molten Zn.

Brunnock (1997), Ph.D. thesis, conducted an extensive study of steels and coatings. Some of the key observations from his work include the following:

1. Attack in molten Zn occurred in austenitic and martensitic steels but not in ferritic stainless steels. This difference was suggested to result from surface finish rather than the Cr content.
2. Addition of 18% Cr to Fe is deleterious, but 9% Ni improves the resistance and Fe-18% Cr-9% Ni is better than unalloyed iron.
3. Finer grain size is attacked faster.
4. Increasing the Si in type 316 from 0.4 to 0.5 wt % increases the life time of bath hardware.
5. Plasma nitride coating on type 316 and low carbon steel (LCS) was detrimental. This was due to poor thermal stability of the coating. The coating was porous and the formation of Cr-nitride most likely prevents the formation of semi-protective chromium oxide.
6. Application of TiN to type 316 completely eliminated attack in molten Zn. This was suggested to occur because of a better adhesion and thermal stability of the coating.
7. The cubic BN on type 316 prevented its wetting.
8. WC/Co-coated type 316 works well in Zn when sealed with boride compound. If not sealed, Co-Zn intermetallics will form.
9. WC/Co coating of 100 μm on type 316 is not affected by the CTE mismatch. However, 150-μm coating spalls off.
10. WC/Co coating on LCS has a better CTE match and spallation is not critical.
11. A ceramic coating of Al_2O_3, SiO_2, and Cr_2O_3 was effective on LCS and type 316 stainless steel.

In summary, literature review showed that many solutions have been proposed, but industry is still not getting the extended performance that is highly desirable for continuous, low-cost, energy saving operations. In this task, we have taken a more scientific approach for identifying possible solutions with desired benefits. Our approaches included: (1) a review of binary phase diagrams to identify the reactivity of Zn with various elements, (2) ThermoCalc™ modeling, and (3) effects of preoxidation.

Binary Phase Diagram Review

The binary phase diagram review of Zn with other elements showed the formation intermetallic phases and the extent of solubility in Zn (see Table 2 for details). Data in Table 2 show that molten Zn will attack all elements. Tungsten is reported not to be

attacked by molten Zn, but no phase diagram is available for W-Zn system.

Alloy System	Intermetallic Phases	Amount of Zinc Dissolved
Ag-Zn	AgZn, Ag_5Zn	Ag 4% + 96% Zn Liquid
Al-Zn	Eutectic 94% Zn MP – 381˚C	Al 32% + 68% Zn Liquid
As-Zn	Zn_3As_2, $ZnAs_2$	As 0% + 100% Zn Liquid
Au-Zn	Au_5Zn_3	Au 10% + 90% Zn Liquid
B-Zn		No phase diagram
Ba-Zn	$Zn_{13}Ba$	Ba 1.2 + 98.8% Zn
Be-Zn		No phase diagram
Bi-Zn	Eutectic with 1.9% Bi MP = 416˚C	Bi5 + 95% Zn
Ca-Zn	$CaZn_2$, $CaZn_5$, $CaZn_{11}$, $CaZn_{13}$	Ca 0% = 100% Zn
Cd-Zn	Eutectic with 17.4% Zn MP – 266˚C	Complete dissolution
Ce-Zn	CeZn, $CeZn_2$, $CeZn_3$, $CeZn_{3.67}$, $CeZn_{4.5}$, $CeZn_{5.25}$, $CeZn_7$, Ce_2Zn_{17}, $CeZn_{11}$	Ce 1% + 99% Zn
Co-Zn		Co < 0.1% + Zn

Table 2: Phase formation at 460°C in molten zinc with various alloying elements

Alloy System	Intermetallic Phases	Amount of Zinc Dissolved
Cr-Zn	Eutectic with 0.3% Cr MP = 415˚C	Cr 0.8% + Zn
Cs-Zn		No phase diagram
Cu-Zn	No intermetallics	Cu 4% + 96% Zn
Er-Zn		No phase diagram
Eu-Zn		No phase diagram
Fe-Zn	$FeZn_{13}$	Fe ~ 0.1 + Zn
Ga-Zn	None	Ga MP ~ 29.7˚C Complete misability
Gd-Zn	None	No phase diagram
Ge-Zn	Eutectic with 94.2% Zn MP =394˚C	Ge 12% + Zn 88%
Hg-Zn		Complete solubility
Ho-Zn		No phase diagram
In-Zn		Liquid complete solubility
Ir-Zn		No phase diagram
La-Zn	$LaZn_{13}$, $LaZn_8$, $LaZn_4$, $LaZn_2$, LaZn Also La-Zn eutectic at 530˚C	La <0.1% Zn

Table 2 continued

Alloy System	Intermetallic Phases	Amount of Zinc Dissolved
Li-Zn	$LiZn$, Li_2Zn_3, Li_3Zn_7, $LiZn_4$	Li-2% + 98% Zn
Mg-Zn	Mg_7Zn_3, $MgZn$, Mg_2Zn_3, $MgZn_2$, Mg_2Zn_{11}	Mg-5% + 95% Zn
Mn-Zn	$MnZn_{13}$ and others	Mn-3% + 97% Zn
Mo-Zn	$MoZn_7$, $MoZn_{22}$	Mo (~0%) + 100% Zn
Na-Zn	$NaZn_{13}$	Na (~0.5%) + 99.5% Zn
Nb-Zn	$NbZn_{15}$, $NbZn_7$, $NbZn_3$, $NbZn_2$, Nb_2Zn_3, $NbZn$	Nb (~0.5%) + 99.5% Zn
Nd-Zn	$NdZn_{11}$, Nd_3Zn_{22}, $Nd_{13}Zn_{48}$, Nd_3Zn_{11}, $NdZn_3$, $NdZn_2$, $NdZn$	Nd (~0.5%) + 99.5% Zn
Ni-Zn	$NiZn$, Ni_5Zn_8, $NiZn_{13}$	Ni (1%) + 99% Zn
Os-Zn		No phase diagram
Pd-Zn	Several intermetallics	Pd (2.5%) + 96% Zn
Pt-Zn	$PtZn_8$	Pt (4%) + 96% Zn
Rb-Zn	$RbZn_{13}$	Rb: MP = 39.5°C
Re-Zn		No phase diagram
Rh-Zn		No phase diagram
Ru-Zn		No phase diagram
Sb-Zn	Sb_3Zn_4, Sb_2Zn_3	Sb-10% + 90% Zn

Table 2 continued

Alloy System	Intermetallic Phases	Amount of Zinc Dissolved
Si-Zn	Eutectic with 99.981 Zn MP = 419.33˚C	Si-Zn (100%)
Sn-Zn	None	Sn 91.2% + 8.8% Zn Eutectic at 91.2˚C
Sr-Zn	$SrZn_{13}$, $SrZn_2$, SrZn	Sr-1% + 99% Zn
Ta-Zn		No phase diagram
Tc-Zn	$Zn_{15-18}Tc$, Zn_6Tc	Tc-0% + 100% Zn
Te-Zn	TeZn (MP = ~1290˚C) Te = 450˚C MP Zn = 420˚C MP	Te-1% + 99% Zn
Th-Zn	Th_2Zn_{17}, $ThZn_4$, $ThZn_2$, Th_2Zn	Th-2% + 98% Zn
Ti-Zn	$Zn_{15}Ti$, $Zn_{10}Ti$, Zn_5Ti, Zn_3Ti, Zn_2Ti, ZnTi, $ZnTi_2$	Ti-2% + 98% Zn
Tl-Zn	Misability gap	Tl-3% + 97% Zn
U-Zn	UZn_{12}, U_2Zn_{17}	U-1% + 99% Zn
V-Zn	VZn_3, V_4Zn_5	V-0% + 100% Zn
W-Zn		No phase diagram
Y-Zn	Y_2Zn_{17}, YZn_5, YZn_4, YZn3, YZn_2, YZn	Y-0% +100% Zn
Zn-Zr	$Zn_{14}Zr$, Zn_8Zr, Zn_3Zr, Zn_2Zr, ZnZr, $ZnZr_2$	Zr-1% + 99% Zn

Table 2 continued

ThermoCalc™

A ThermoCalc™ analysis was used to validate the available data for predicting various phase diagrams (see Figures 14 and 15 for Al-Zn and Fe-Zn). These and other analyses show that except for Al-Zn binary alloy system, predictions are in poor agreement with the published phase diagrams for Zn-Cr, Ni-Zn, Fe-Zn, and Mo-Zn. A further review showed that there is a need for substantial thermodynamics optimization work using PAROT software to evaluate the thermodynamic data from published binary diagrams and devise methodologies to extend the binary thermodynamic data. Only limited information is published on ternary systems and the available data are from Tang and Ostward et al.

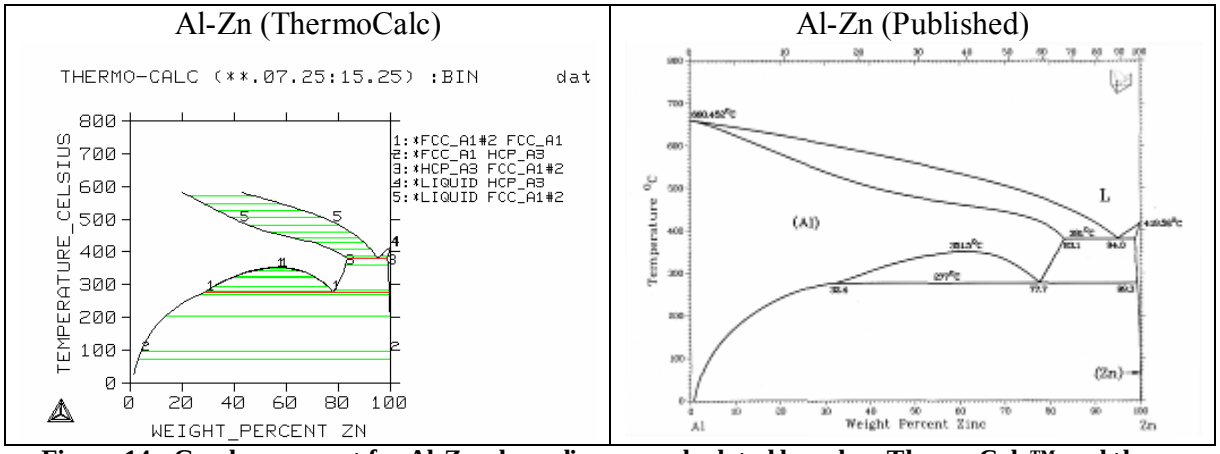

Figure 14: Good agreement for Al-Zn phase diagram calculated based on ThermoCalc™ and the published diagram.

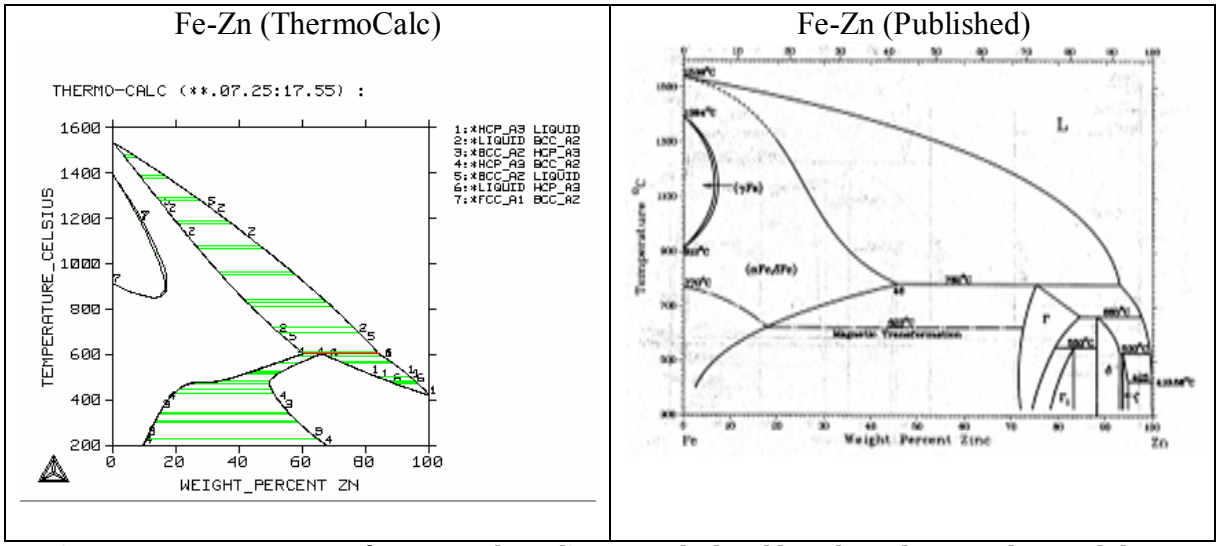

Figure 15: Poor agreement for Fe-Zn phase diagram calculated based on ThermoCalc™ and the published diagram.

Task 3 Materials Development

The task of materials development was a joint effort with ORNL and the industrial partners to come up with new metallic and ceramic materials that can be used for bearing and roll applications. Series I materials consist of those currently used in coating applications. Series II materials are monolithic alloys and ceramics that have been developed by ORNL. Series III materials are weld overlay coatings.

Sub-Task 3.1 Series I Development

In the early stages of the project, a broad range of materials were selected for screening using the static corrosion test at the Oak Ridge National Laboratory (ORNL). A complete list of materials, its source, and material condition used are presented in Table 3. In most cases, a sample of ~ 0.5 × 0.5 × 0.25 in. was used. However, there were many cases where such sample size was not possible. In each case, the sample was immersed in a molten bath of Zn-0.16 Al-0.013 Fe at a temperature of 465ºC. Detailed chemical analysis of the bath at the test start and after various test times for ORNL alloy 4 series is shown in Table 4. Samples were removed from the bath at various times, acid cleaned (50% HCl), and weighed to record the weight change. The weight change after 500 h for materials tested in the machined condition is compared in Figure 16. Similar comparison after preoxidation is shown in Figure 17.

Item No.	Material Description		Material Source	Material Condition
	Designation	Type		
1	2-1	Type 316L	Steel partner B [a]	Section from stabilizer roll rolled to ~ 0.25 in. thickness
2	2-1A	Type 316L	Steel partner B [a]	Rolled/machined sample preoxidized in air for 1 h at 1000ºC
3	2-1B	Type 316L	Steel partner B [a]	Rolled/machined sample preoxidized in air for 2 h at 1000ºC
4	A2	Tool steel A2	Commercial supplier	Machined sample
5	D2	Die steel A2	Commercial supplier	Machined sample
6	4	Fe20Cr4.5Al	ORNL	Extruded/machined sample
7	4A	Fe20Cr4.5Al	ORNL	Preoxidized in air for 1 h at 1100ºC
8	4B	Fe20Cr4.5Al	ORNL	Preoxidized in air for 2 h at 1100ºC
9	4-1	Fe20Cr4.5AlY	ORNL	Extruded/machined sample
10	4-1A	Fe20Cr4.5AlY	ORNL	Preoxidized in air for 1 h at 1100ºC
11	4-1B	Fe20Cr4.5AlY	ORNL	Preoxidized in air for 2 h at 1100ºC
12	4-2	Fe20Cr6.5AlY	ORNL	Extruded/machined sample
13	4-2A	Fe20Cr6.5AlY	ORNL	Preoxidized in air for 1 h at 1100ºC
14	4-2-B	Fe20Cr6.5AlY	ORNL	Preoxidized in air for 2 h at 1100ºC
15	4-3	Fe20Cr8.5AlY	ORNL	Extruded/machined sample
16	4-3A	Fe20Cr8.5AlY	ORNL	Preoxidized in air for 1 h at 1100ºC
17	4-3B	Fe20Cr8.5AlY	ORNL	Preoxidized in air for 2 h at 1100ºC
18	4-4	Fe30Cr6.5AlY	ORNL	Extruded/machined sample
19	4-4A	Fe30Cr6.5AlY	ORNL	Preoxidized in air for 1 h at 1100ºC
20	4-4B	Fe30Cr6.5AlY	ORNL	Preoxidized in air for 2 h at 1100ºC
21	2012	Unknown	Supplier A	As machined
22	2020	Unknown	Supplier A	As machined

Table 3: Material description, source, and condition prior to testing

Item No.	Material Description		Material Source	Material Condition
	Designation	Type		
23	Alloy 5	W-20 Mo	Deloro Stellite Group, Ltd.	As-weld overlaid
24	Alloy 6	W	Deloro Stellite Group, Ltd.	As-weld overlaid
25	ACD	Ceramic	Vesuvius	As-received condition
26	1B	Tribocor™	MATTEC	Machined and uncoated
27	1A	Tribocor™	MATTEC	Nitrided at 1600ºC
28	1C	Tribocor™	ORNL	Nitrided at 1100ºC
29	Type 316L	Sheet	ORNL	As rolled
30	Type 316L	Sheet	ORNL	Rolled plus preoxidized in air for 2 h at 1000ºC
31	Al weld overlay	Type 316	ORNL	Preoxidized in air for 2 h at 1100ºC
32	Al weld overlay	D2 Steel	ORNL	Preoxidized in air for 2 h at 1100ºC
33	4-2 weld overlay	Type 316	ORNL	Preoxidized in air for 2 h at 1100ºC
34	DC carbide	WC/Co binder	Rogers Tool Works	As machined
35	DC carbide	WC/Co-Ni-Cr-Mo	Rogers Tool Works	As machined
36	Stellite 6	Co-Cr-W alloy	ORNL	Cast and as machined
37	Stellite 6	Co-Cr-W alloy	Stellite	HIPped powder and as machined
38	Tribaloy T800	Co-Cr-Mo-Si alloy	Stellite	HIPped powder and as machined
39	Type 316L nitrided	Type 316L nitrided	Mohan	Sheet as nitrided (no machining)
40	4-2C	Fe-20Cr-6.5Al-0.2Y	ORNL	Extruded, machined, and preoxidized in air for 2 h at 1100ºC
41	4-2D	Fe-20Cr-6.5Al-0.2Y	ORNL	Extruded, machined, and preoxidized in air for 2 h at 1100ºC
42	4-2YE	F-20Cr-6.5Al-0.2Y	ORNL	Extruded, machined, and preoxidized in air for 2 h at 1100ºC
43	4-2MME	Fe-20Cr-6.5Al-0.2MM	ORNL	Extruded, machined, and preoxidized in air for 2 h at 1100ºC

Table 3 continued

	Al %	Cu %	Fe %	Pb %	Cd %	Si %	Zn %
Zinc Start-up Material							
Bulk Material	0.1593	0.0005	0.0131	0.0019	0.0010	<0.0003	99.82
Static Test							
Alloy 4 500h	0.1688	0.0005	0.0156	0.0022	0.0010	<0.0003	99.81
Alloy 4-1 500h	0.1689	0.0004	0.0163	0.0021	0.0008	<0.0003	99.81
Alloy 4-2 500h	0.1674	0.0004	0.0147	0.0020	0.0007	<0.0003	99.81
Alloy 4-4 500h	0.1723	0.0005	0.0167	0.0022	0.0010	<0.0003	99.81
Dynamic Test							
Top Dross 48h	0.4400	0.0004	0.0169	0.0019	0.0009	<0.0003	99.54

Average (n=3)

Table 4: Chemical composition analysis

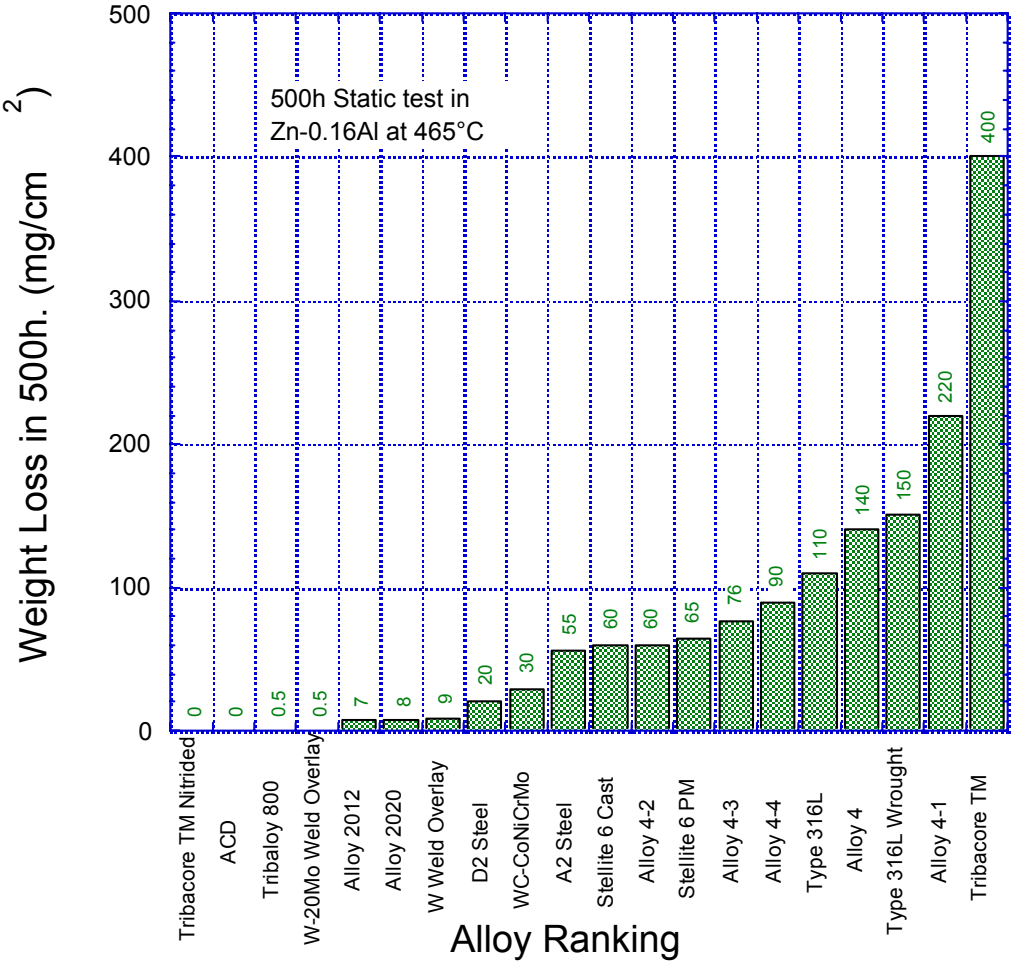

Figure 16: Materials ranking in machined conditions.

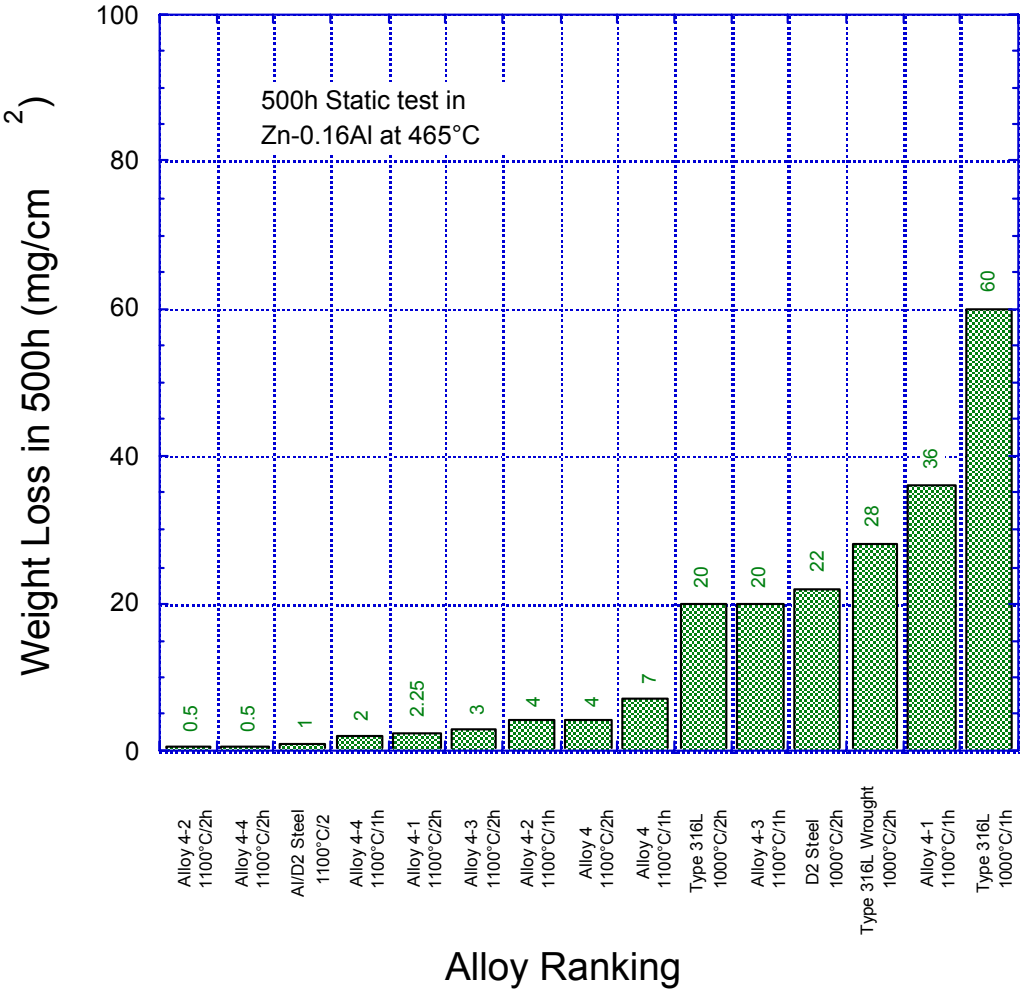

Figure 17: Materials ranking with preoxidation treatment.

Data in Figures 16 and 17 for materials tested in the machined and pre-oxidized conditions showed the following:

1. An order of magnitude improved resistance of an advanced material in Zn-0.1-0.02 Al at 465ºC will require corrosion weight loss rate of ≤ 10 mg/cm^2 (given that type 316L is 110 mg/cm^2) in 500-h exposure.
2. With < 10 mg/cm^2 in 500-h criteria, most desirable materials are Tribacore™ nitrided, ACD ceramic, Tribaloy 800, weld overlay of W-20Mo on type 316L, 2012, 2020, and weld overlay of W on type 316L.
3. Choice of metallic materials that are economical and can be fabricated under current commercial conditions, the list reduces to Tribaloy 800, weld overlay of W-20Mo on type 316L, 2012, 2020, and weld overlay of W on type 316L.
4. Among the ceramics, ACD clearly is the choice.
5. With ≤ 10 mg/cm^2 in 500-h criteria, most desirable materials are alloy 4 series (alloys 4-2, 4-4, 4-1, 4-3, 4) and aluminum weld overlay on D2 tool steel.
6. Confirm results on two of alloy 4 series (4-2 and 4-4).
7. Based on Al weld overlay on D2, also attempt Al weld overlay on type 316L.

Based on data in Figures 16 and 17, as well as the observations listed above, the following recommendations were made, which lead to Series-II materials described in the next section.

1. Need further understanding of 2012 and 2020 alloys. Can they be used as weld overlays?
2. Can Tribaloy 800 be used as weld overlays?
3. Confirm results on two of alloy 4 series (4-2 and 4-4).
4. Based on Al weld overlay on D2, also attempt Al weld overlay on type 316L.
5. Confirm the choice of these materials under dynamic condition (ORNL and WVU/Duraloy tests).
6. Develop procedure for weld overlay of Al on D2 or type 316L (if this looks good) for prototype components.
7. Further optimize the preoxidation process for consistent performance and for prototype components.

Sub-Task 3.2 Series II Development

Based on results presented in Figures 16 and 17, materials that matched or exceeded the corrosion performance of type 316L were chosen for long-term corrosion testing. These down-selected materials were designated as Series II. Based on the corrosion testing of Series II, a summary table of corrosion rates of various alloys is presented in Table 5.

Corrosion Loss (mg/cm²)								
Alloy	300 h	500 h	1000 h	2000 h	3000 h	4000 h	5000 h	6000 h
2020	2	3	4	5				
2012	2	3	6	12				
Tribaloy 800	0	0	0.1	0.2	0.3	0.4		
ACD	0	0	0	0	0	0	0	0
4-2[a]	0	0	0-10					
W-12Cr-38Fe[b]	3	3	6					
W-12Cr-38Fe[c]	6	10						
WC-Co[d,e]	1							
WC-Tribaloy 800[d,f]	4							
Type 316 SS	45	60						

[a]Preoxidized (two different preoxidation conditions).
[b]Arc melted.
[c]Induction melted.
[d]Liquid phase sintered.
[e]Very low porosity.
[f]High porosity (needs sintering process improvement).

Table 5: Summary of the corrosion data on Series II materials

The following conclusions are possible from Table 5:

1. Tribaloy 800 is the best metallic material based on its corrosion loss.
2. ACD is the best ceramic material.
3. Alloy 2020 is the second best metallic material to Tribaloy 800.
4. ORNL alloy 4-2 is a very promising low-cost metallic material. However, it needs preoxidation for its performance.
5. W-Cr-Fe alloys prepared at ORNL to take benefit of good performance of tungsten were promising but had to be dropped because of their embrittlement.
6. WC-Co, liquid phase-bonded, showed good performance. These data validates the use of WC-Co as thermal spray coatings on type 316L.
7. Based on the excellent performance of Tribaloy 800, we attempted to use it as a binder to replace Co. We used liquid phase sintering to produce WC-Tribaloy 800; however, its performance was not as expected because of high porosity. Further optimization of processing parameters was needed to improve its performance.

Sub-Task 3.3 Series III Development

The focus for Series III materials development was to find practical low-cost methods for utilizing the best performing materials into practice. One of these materials was 2020, and we identified weld overlay as one of the low-cost methods for using it. In order to carry out the weld overlays of 2020, its wire was produced by Stoody Co. by the powder core approach. This is the first time such a filler wire was ever produced. Multiple pass welds were prepared using this wire on type 316L plate. Two weld samples were prepared, each using a metal inert gas (MIG) process. The detailed microstructural analysis of one of the multiple pass welds of 2020 on type 316L is shown in Figures 18 through 25.

Prior to making multiple pass welds, a single pass weld was also prepared. The microhardness data for the single and multiple pass welds are shown in Figures 26 and 27. The weld overlay is identified by four regions: weld top (2020), intermix region, interface, and substrate (type 316L). In the multiple pass welds, surface hardness was maximum and reached average values of ~ 575 Vicker's. In the single pass weld where the weld surface is diluted, its hardness was ~ 480 Vicker's.

The weld overlay procedure for aluminum weld overlay on carbon and stainless steels was developed. Results of this study have been published.[1]

The weld overlay study of 2020 over type 316L showed the following:

1. Weld wire of 2020 was successfully produced.
2. The powdered core wire was successfully used to do a multiple pass weld on stainless steel type 316.
3. Microstructural analysis showed no indication of interfacial or weld cracking.
4. Hardness profile indicates that the top 7-8 mm of the weld is of uniform hardness, which is close to that observed for the monolithic 2020.
5. From microstructure and hardness presented here, it looks very encouraging that 2020 may be useable as weld overlay for certain molten zinc hardware applications.

[1]Y. Bhambir, V. K. Sikka, L. R. Walker, M. L. Santella, G. Muralidharan, and J. W. Hales, "Al enrichment of carbon steels through weld overlay process for improved oxidation resistance," *Materials Science and Engineering A* 394 (2005) 249-255.

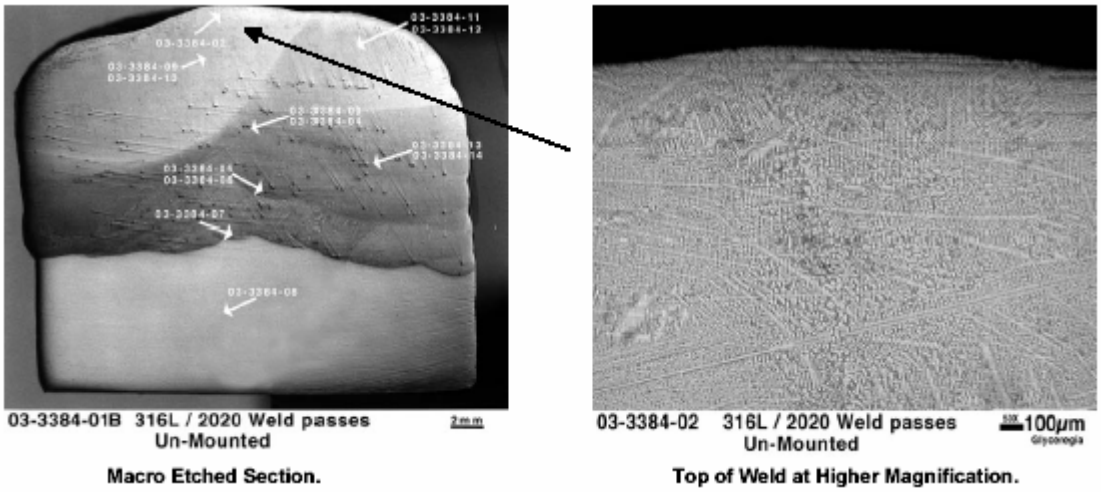

Figure 18: Top of weld overlay specimen.

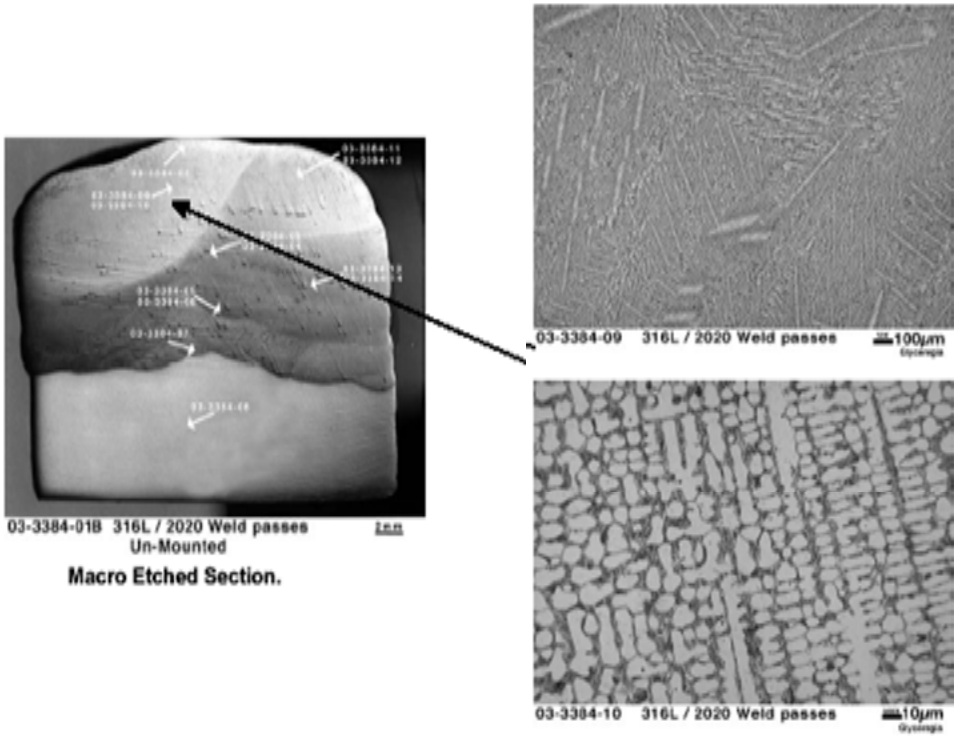

Figure 19: Low and high magnification microstructure of top left weld overlay pass.

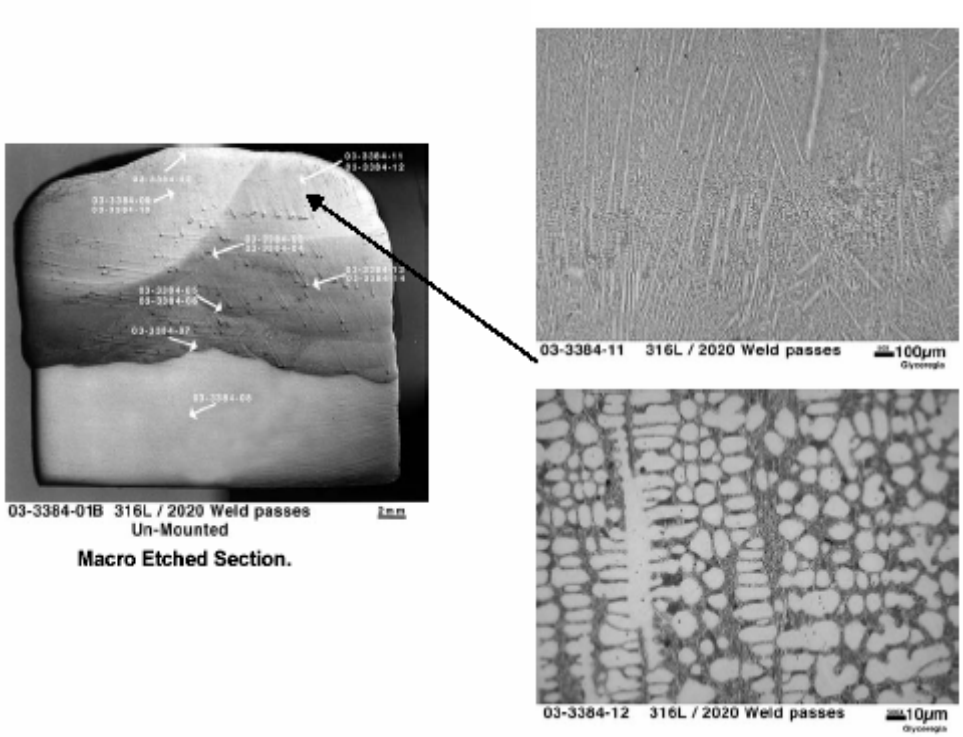

Figure 20: Low and high magnification microstructure of top right weld overlay pass.

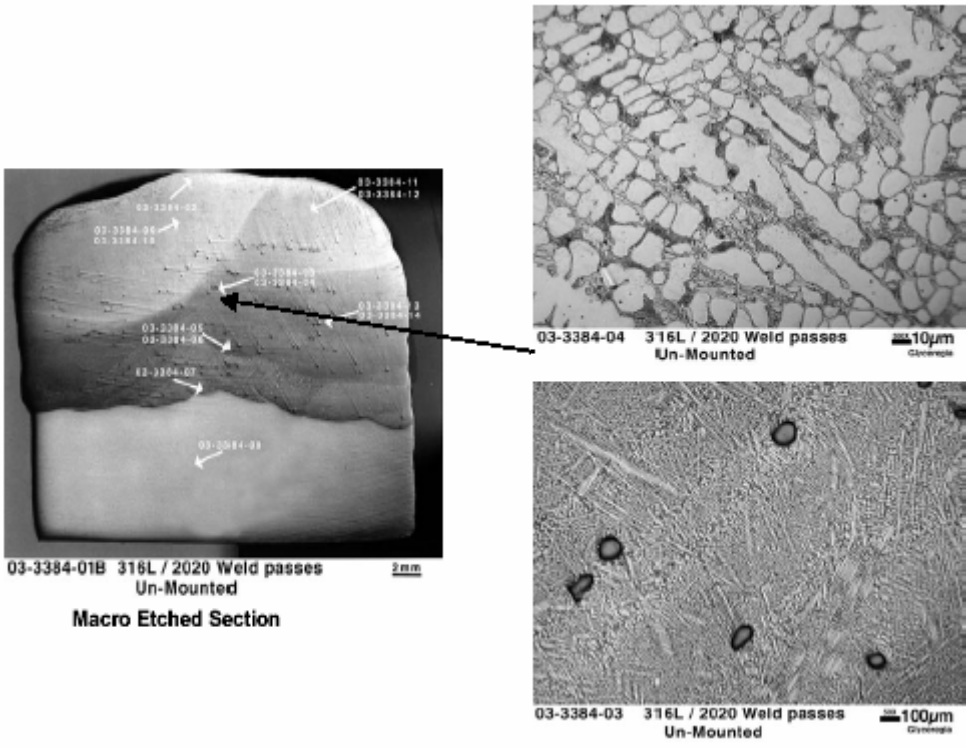

Figure 21: Low and high magnification microstructure of the pass below the top pass in the middle area.

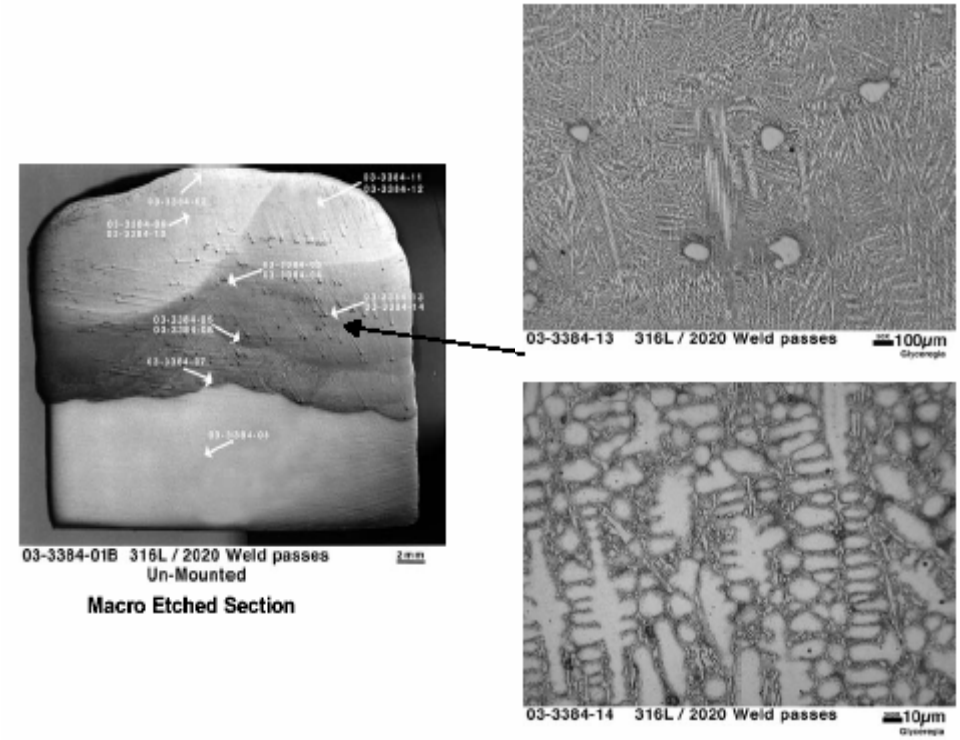

Figure 22: Low and high magnification microstructure of the second pass below the top pass on the right side.

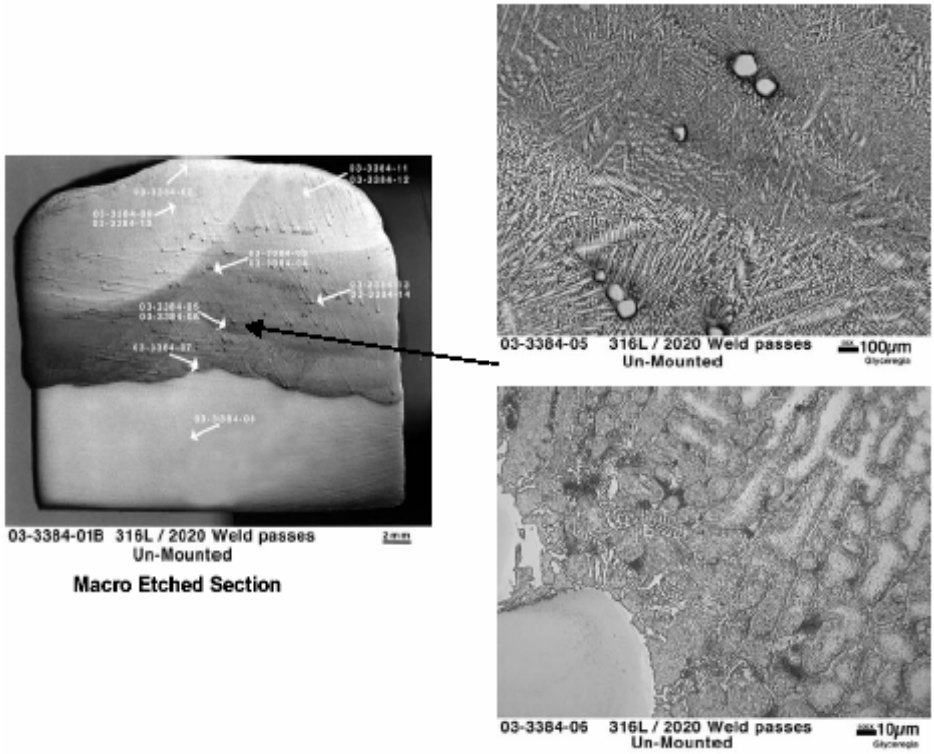

Figure 23: Low and high magnification microstructure of the third pass below the top pass in the middle of the weld.

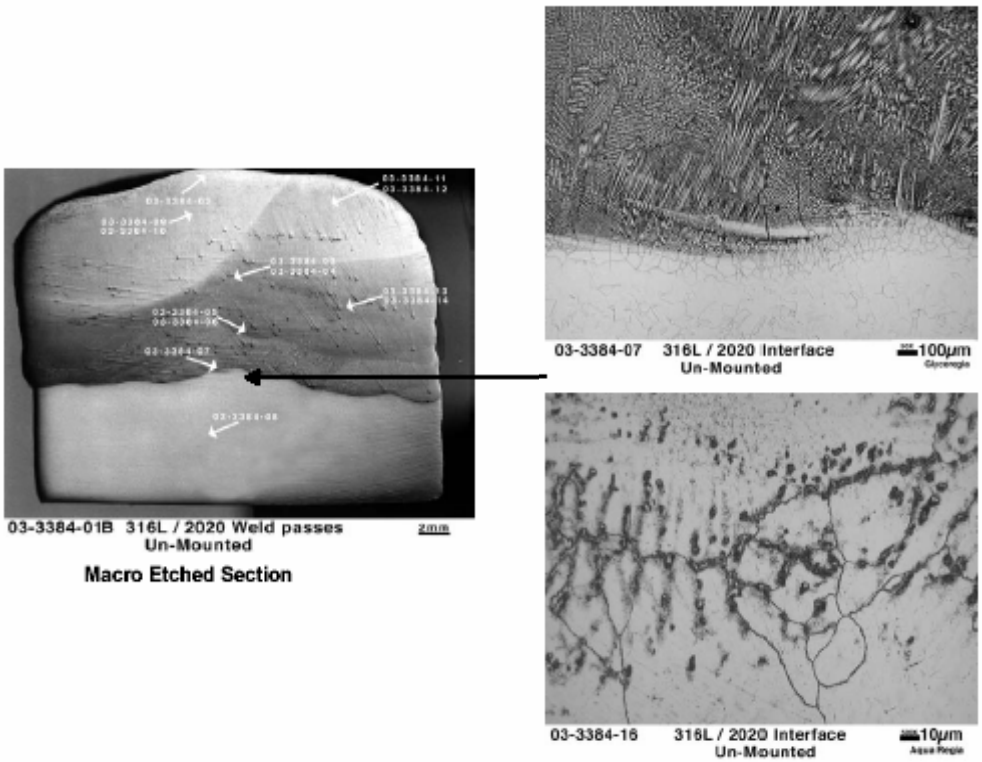

Figure 24: Low and high magnification microstructure of interface of 2020 on stainless steel type 316L.

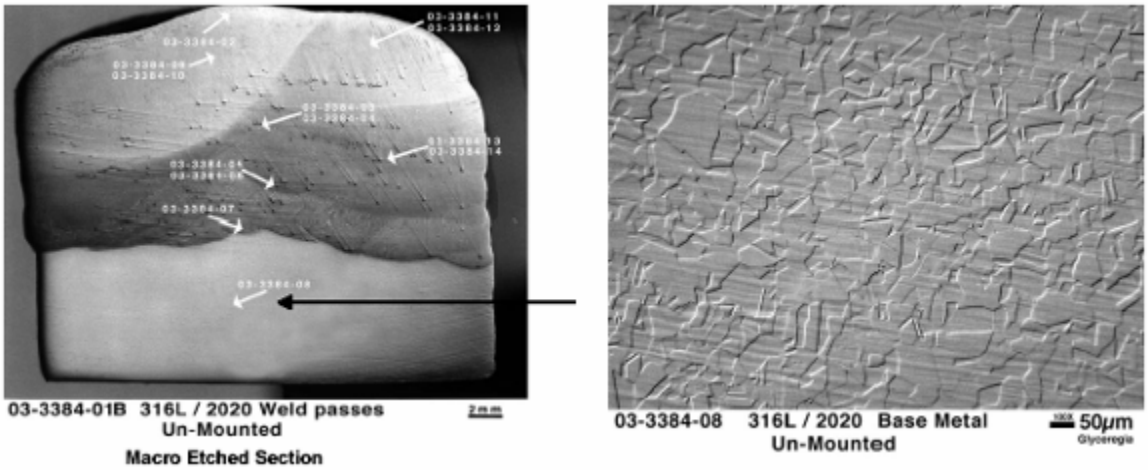

Figure 25: Base material – stainless steel type 316L.

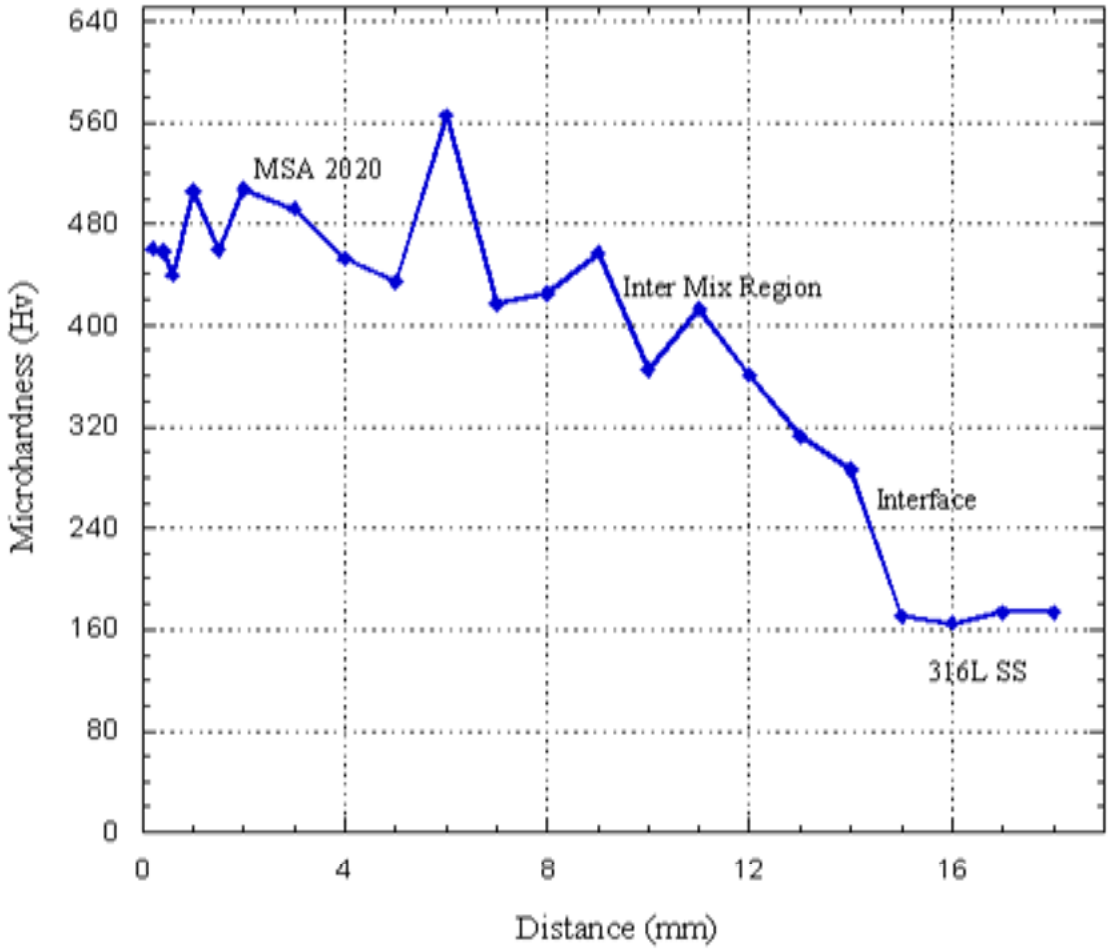

Figure 26: Hardness traverse from surface to core on weld overlay of a single pass weld of 2020 on stainless steel type 316L using MIG process.

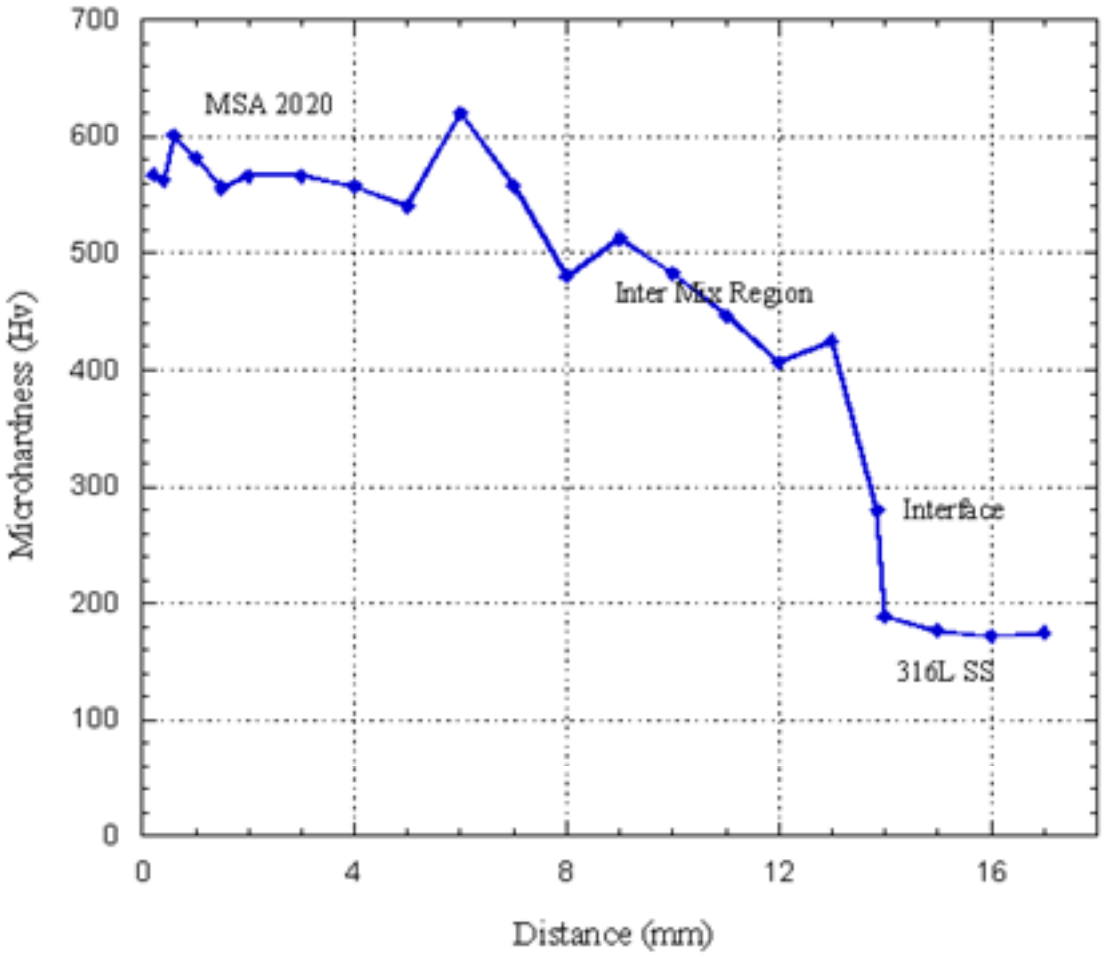

Figure 27: Hardness traverse from surface to core on multiple pass weld overlay of 2020 on stainless steel type 316L.

Task 4 Materials Testing

For this task, the materials developed in Task 3 through research and development at ORNL as well as submission from the material suppliers participating in the project were tested under corrosion, wear, and corrosion assisted wear conditions in order to accurately assess the overall performance of potential pot hardware materials for bearing and roll applications. From the outset of the project, it was determined that baseline information for standard commercially used material systems be tested in order to provide baseline information and verify the test results with other research efforts. All facets of Series I testing deal with baseline or currently used materials in the hot dip coating of rolled sheet steel. For Series II, the materials that were selected and tested were either newly developed materials from ORNL or new alloys, ceramics, and/or test material combinations that have not been previously tested. Series II was limited to new monolithic materials and/or combinations. For Series III, the knowledge gained from the results in Series I and II were used to select candidate materials that could be applied to baseline stainless steel substrates in the form of weld overlays or other coatings.

Sub-Task 4.1 Series I Testing

The following table details the materials selected for testing under Series I.

Series I Materials	Material Description	Use
CF-3M Stainless Steel	Stainless steel alloy used primarily for	Roll material
CF-3M SS with WC Spray coating	Tungsten carbide coating in CF3M substrate for improved corrosion resistance	Roll material
Stellite 6	Co-based superalloy used extensively for bearing applications.	Bushing/sleeve material
316L SS	Stainless steel alloy used for bearing applications as a monolith	Bushing/sleeve material
316L SS with Laser Clad WC coating	316L substrate for laser cladding, sprays, and weld overlays	Sleeve material
Wearguard Ceramic	Hard ceramic used in the form of a 3 bar shape along with the 316L-LCWC sleeve. Non wetting and good wear resistance.	Bushing material

Table 6: Series I material table

Sub-task 4.1.1 Series I Lab Scale Corrosion Testing

Four types of specimens were used during the lab-scale corrosion testing (see Figures 28 through 31). Tables 7 through 9 show the chemical analysis of various alloys used in the present investigation.

Figure 32 shows the baseline data on type 316 stainless steel. This graph also includes the data for wrought sheet and cast pipe in both unoxidized and preoxidized conditions. Figure 33 shows the data for A2 tool steel, which has performance very similar to that of type 316L. Data for D2 tool steel in the wrought and preoxidized conditions are shown in Figure 34. This graph shows that D2 had better performance than type 316L.

Data for ORNL alloy 4 are shown in Figure 35. This plot clearly shows that for ORNL alloy 4 to work, it needs preoxidation at 1100ºC. With such a treatment, corrosion loss was reduced to an insignificant amount.

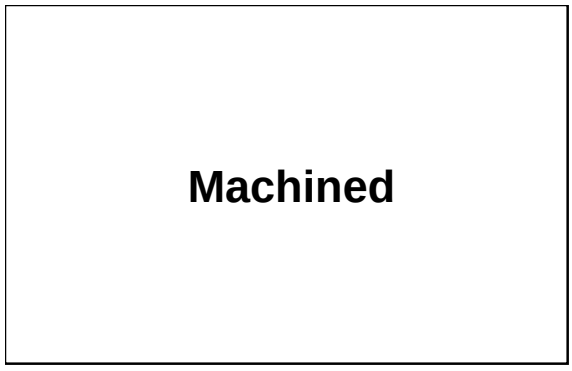

Figure 28: Monolithic (M) specimen. Examples of this specimen are type 316L and ACD ceramic.

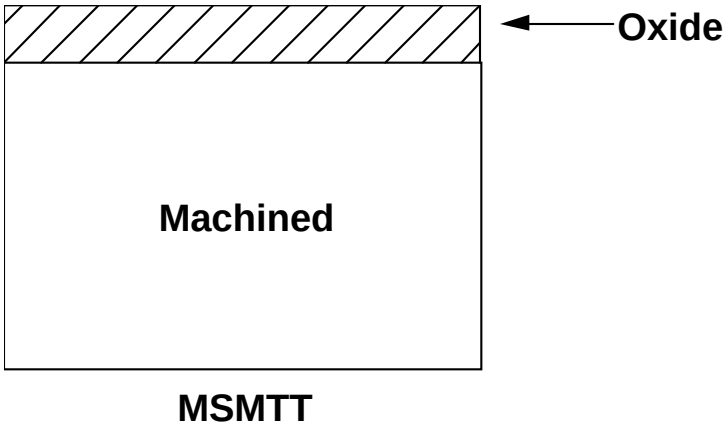

Figure 29: Monolithics with surface modified by thermal treatment (MSMTT). Examples of this specimen are Alloy 4-2 preoxidized to form Al2O3 on the surface.

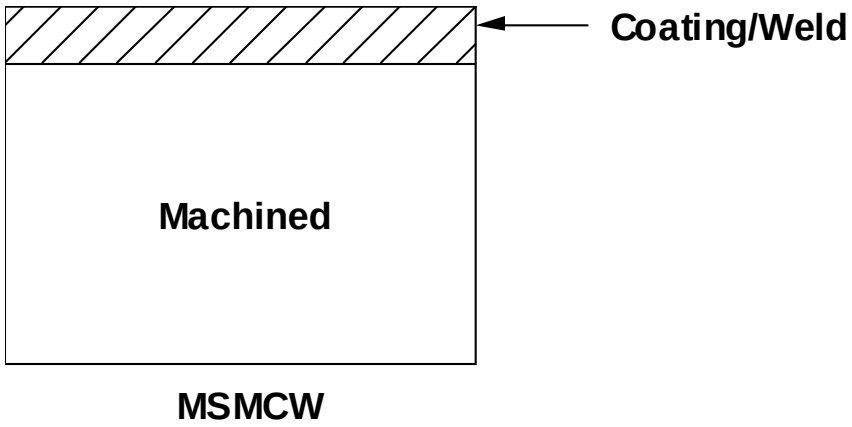

Figure 30: Monolithics with surface modified by coating/welding (MSMCW). Examples of this specimen are W – weld overlaid on substrate (steel or type 316L) and WC-Co coating on type 316L.

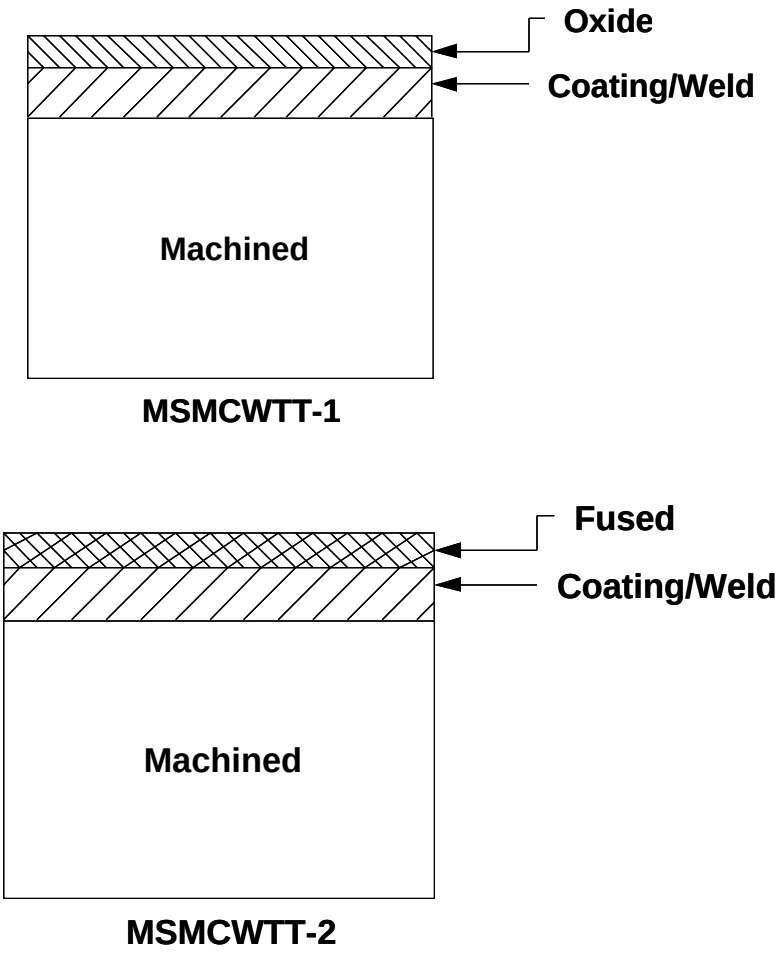

Figure 31: Monolithics with surface modified by coating/welding and by thermal treatment (MSMCWTT). Examples of this specimen are aluminum weld overlaid on alloy D2 and preoxidized WC coating on type 316L and laser-fused.

Element	Alloys (wt %)		
	A-2 Tool Steel	D-2 Tool Steel	Type 316L
C	0.95-1.05	1.40-1.60	0.03
Mn	0 75	1.00	1 50
P	0 03	0.03	0 04
S	0 03	0.03	0 04
Si	1 50	1.50	1 50
Cr	4 75-5 50	11.00-13.00	17 0-21.0
Mo	0 90-1.40	0.70-1.20	2-3 0
V	0.20-0.50[a]	0.40-1.00[a]	---
Co	---	0.70-1.00[a]	---
Ni	---	---	9.0-13.0

Table 7: Chemical compositions of alloys A-2, D-2, and type 316L

Element/ Hardness (R_C)	Alloy Designation (wt %)				
	No. 4 18117	No. 4-1 18118	No. 4-2 18119	No. 4-3 18120	No. 4-4 18121
Fe	74.78	74.58	72.58	70.68	62.68
Cr	20.00	20 00	20 00	20 00	30 00
Al	4.50	4.50	6.50	8.50	6.50
Ti	0.50	0.50	0.50	0.50	0.50
Si	0.10	0.10	0.10	0.10	0.10
Mn	0.10	0 10	0 10	0 10	0 10
C	0.02	0.02	0.02	0.02	0.02
Y	--	0.20	0.20	0.20	0.20
Cast hardness	10	12	17	20	16

Table 8: Chemical composition of Fe-Cr-Al alloys for wetting and corrosion testing in molten zinc

Element	Alloy (wt %)	
	Stellite 6	Tribaloy 800
C	1.2	0.08
Co	Balance	Balance
Cr	29.0	18.0
Fe	2.0	---
Mn	1.0	---
Mo	0.8	28
Ni	2.0	1
Si	1.4	3.4
W	4.5	---

Table 9: Alloy compositions of Stellite 6 and Tribaloy 800

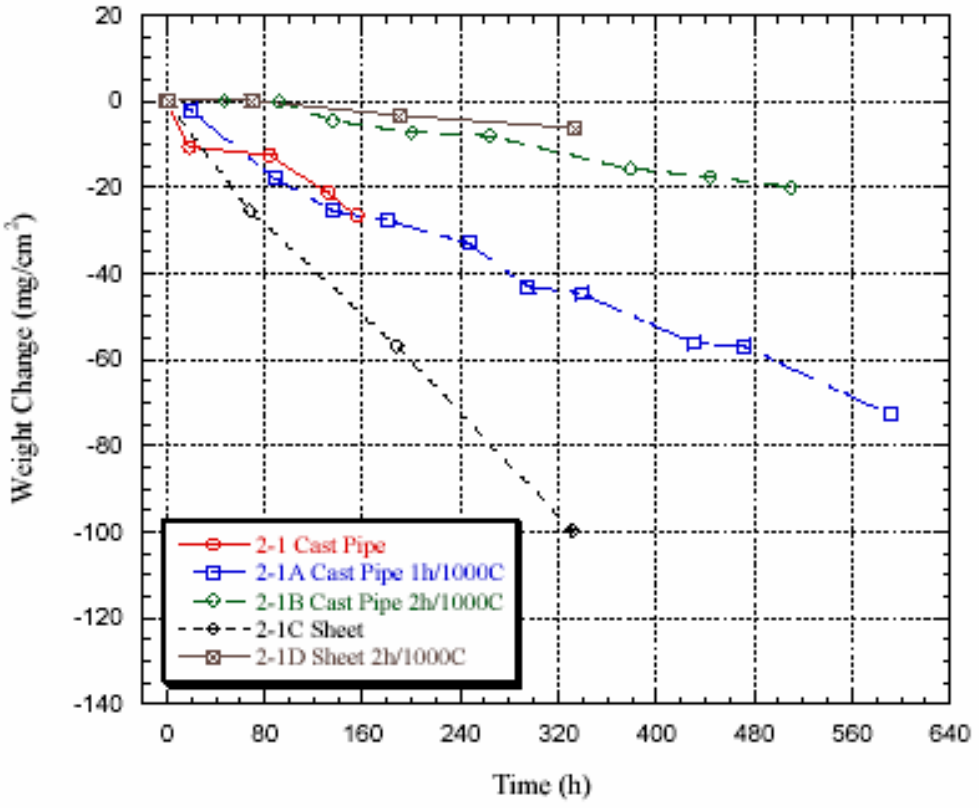

Figure 32: Preoxidation improves the performance of type 316L in molten zinc at 465°C. Wrought sheet is better than cast pipe.

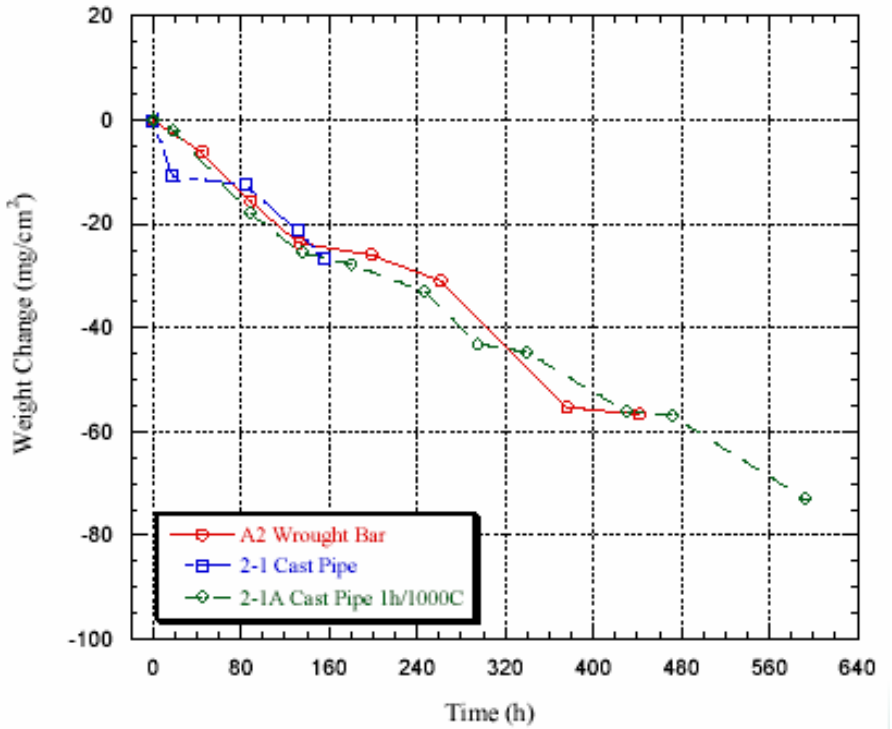

Figure 33: The A2 tool steel tested in molten zinc at 465°C has performance similar to type 316L.

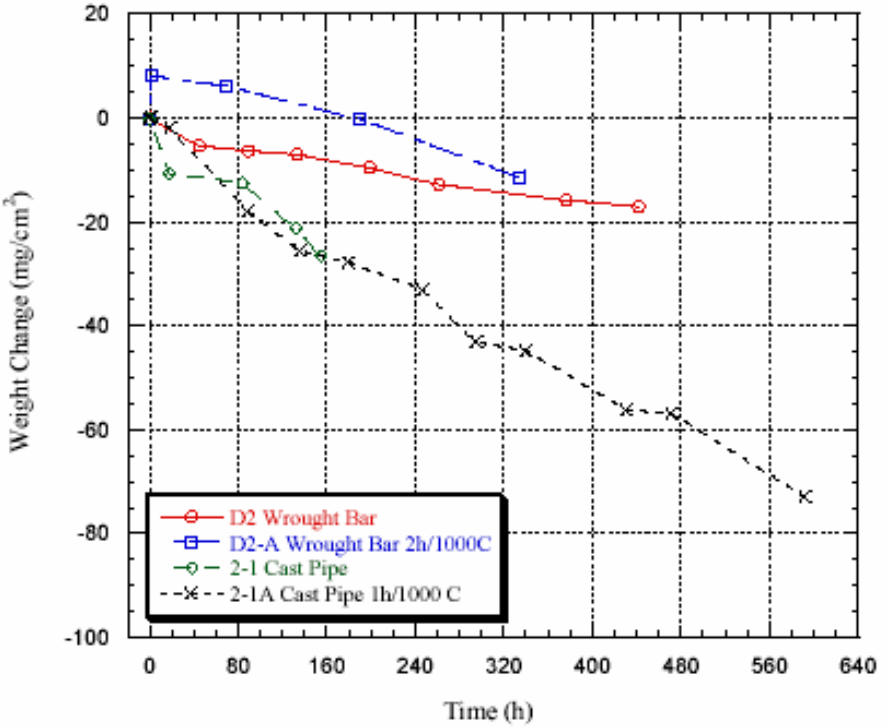

Figure 34: D2 tool steel in molten zinc at 465°C is better than type 316L. Preoxidation does not seem to be effective.

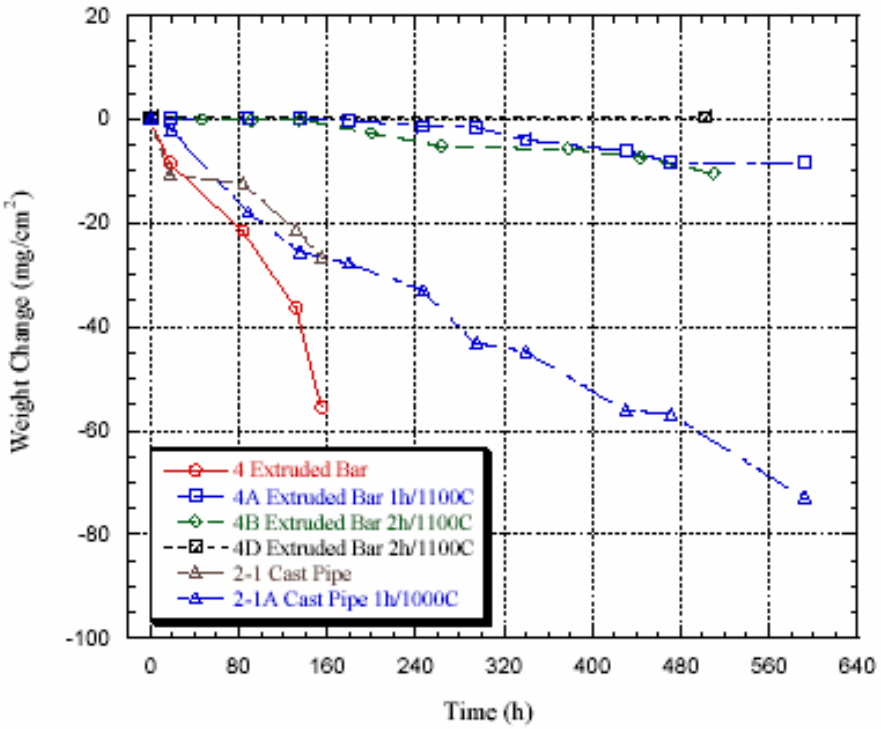

Figure 35: Alloy 4, in the preoxidized condition in molten zinc at 465ºC, is over an order of magnitude better than type 316L.

Figure 36 shows the corrosion data for ORNL alloy 4-1. Results for this alloy are similar to alloy 4 in Figure 35 above. Data in Figure 36 show that a preoxidation of 2 h at 1100ºC produces a more desirable protective oxide than a treatment of 1 h at 1100ºC. Data for ORNL alloy 4-2 (Figure 37) show it to have excellent performance after both 1- and 2-h preoxidation treatments at 1100ºC. This alloy showed better performance than alloy 4 and alloy 4-1. Data on ORNL alloys 4-3 and 4-4 are shown in Figures 32, 38, and 39. These figures show that alloy 4-4 has performance similar to alloy 4-2, which has lower alloy content.

Alloy 2012, supplied by Supplier A, showed excellent performance as opposed to type 316L (Figure 40) and did not require a preoxidation treatment. Alloy 2020, supplied by Supplier A, also showed performance (Figure 41) similar to 2012, without requiring the preoxidation treatment.

The W-20 Mo weld overlay or carbon steel also showed exceptional performance with requiring preoxidation treatment (Figure 42). The pure tungsten weld overlay on carbon steel (Figure 43) also showed good performance, but not as good as W-20 Mo weld overlay in Figure 42.

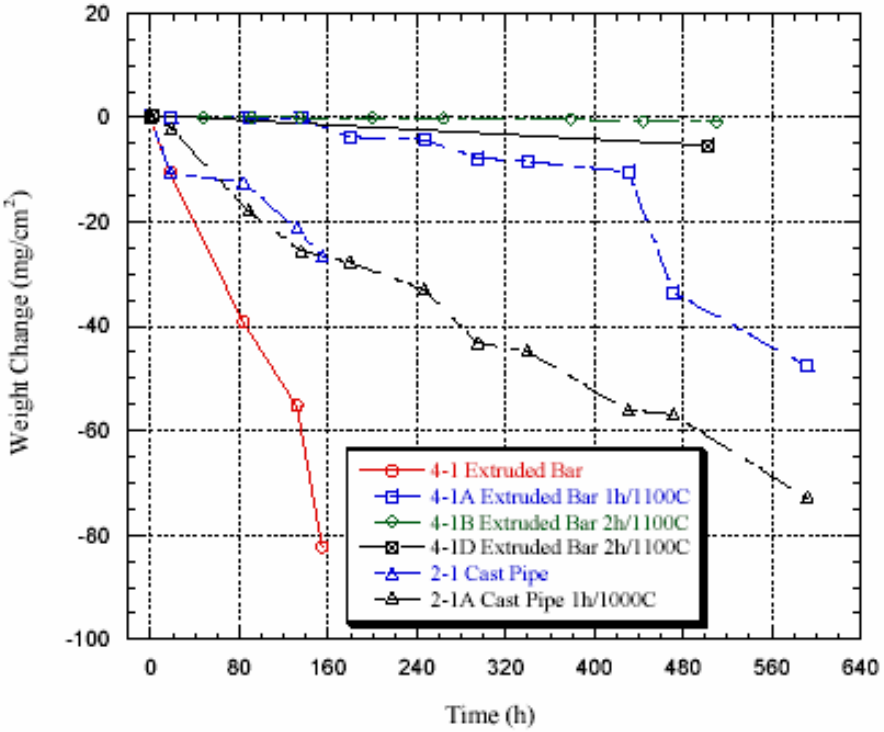

Figure 36: Alloy 4-1, in the preoxidized condition in molten zinc at 465°C, is similar to alloy 4 and over an order of magnitude better than type 316L.

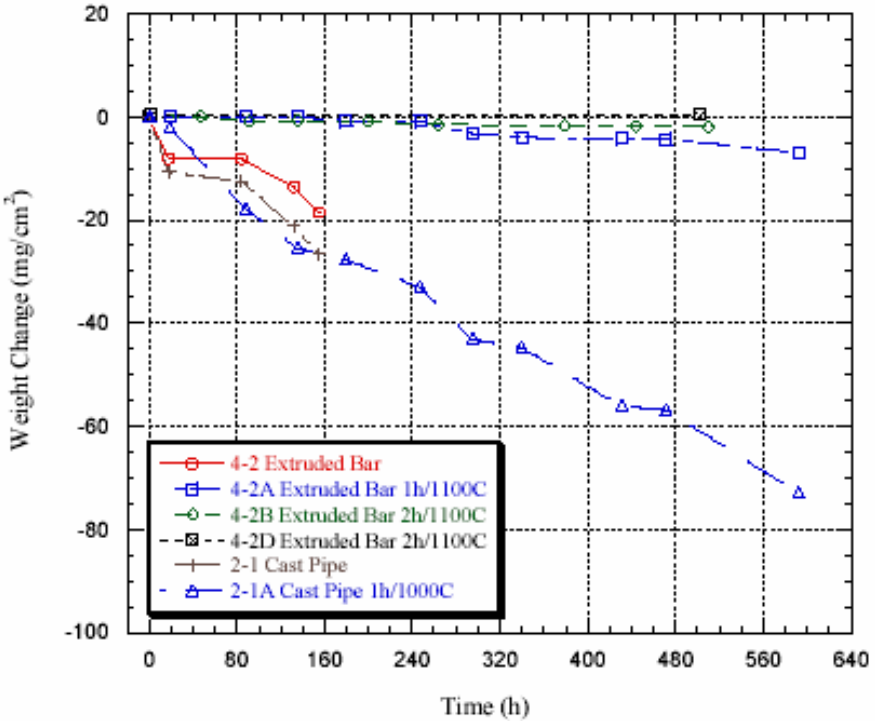

Figure 37: Alloy 4-2 in molten zinc at 465°C is better than alloys 4 and 4-1.

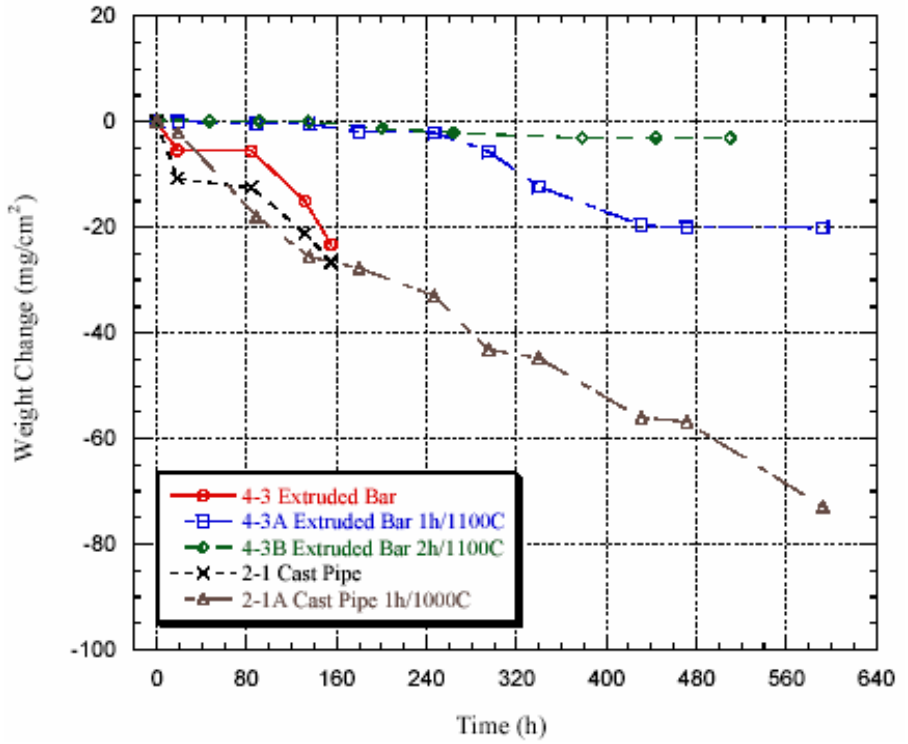

Figure 38: Alloy 4-3 in molten zinc at 465°C is not as good as alloys 4, 4-1, and 4-2.

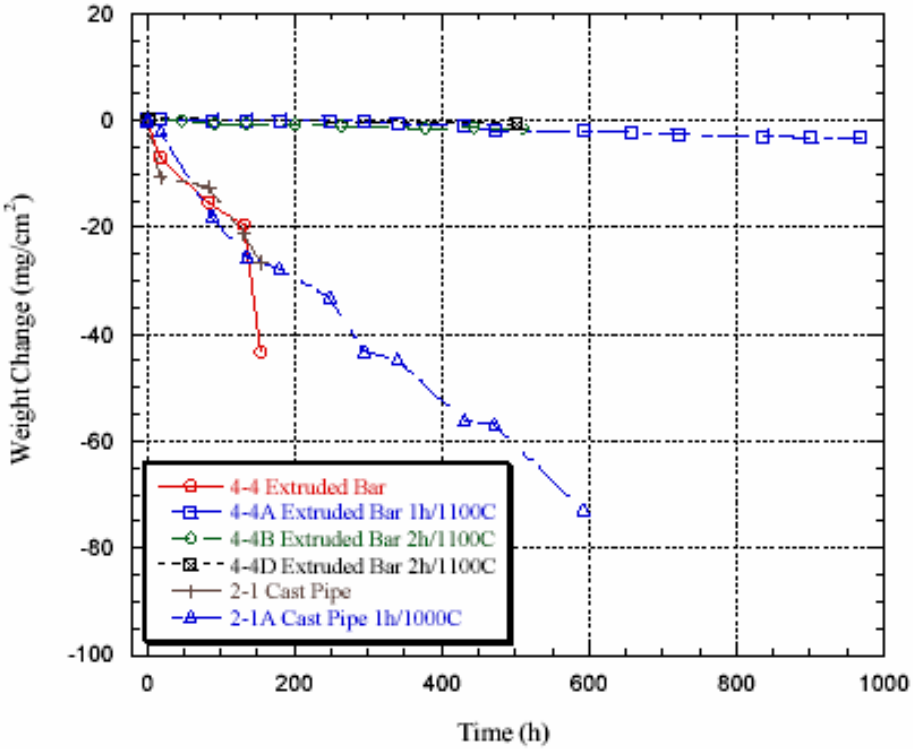

Figure 39: Alloy 4-4 in molten zinc at 465°c has performance similar to alloy 4-2, which has lower alloy content.

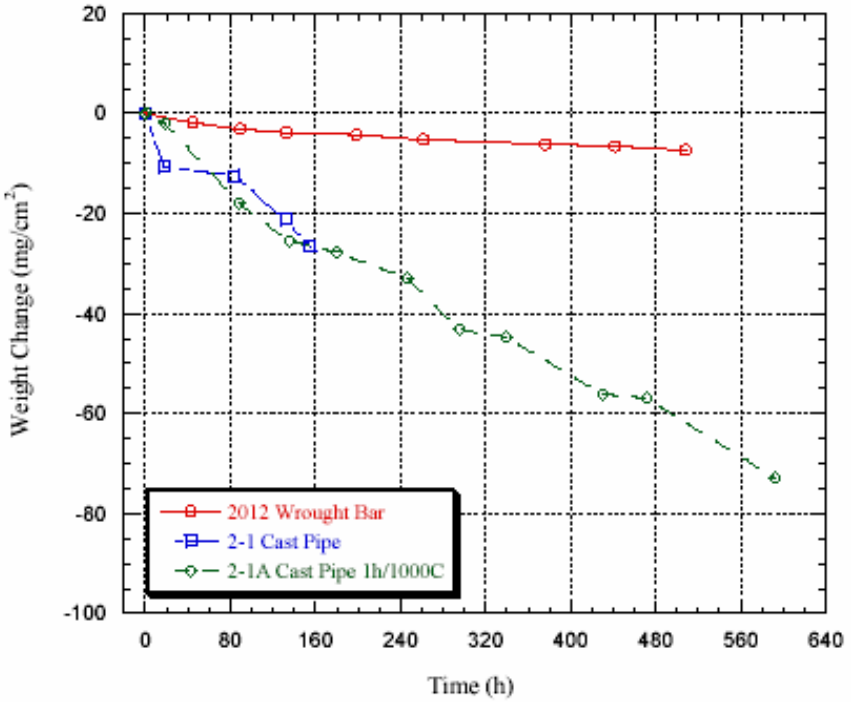

Figure 40: Alloy 2012, supplied by Supplier A, showed over a factor of 4 less weight change in molten zinc at 465°C as opposed to type 316L.

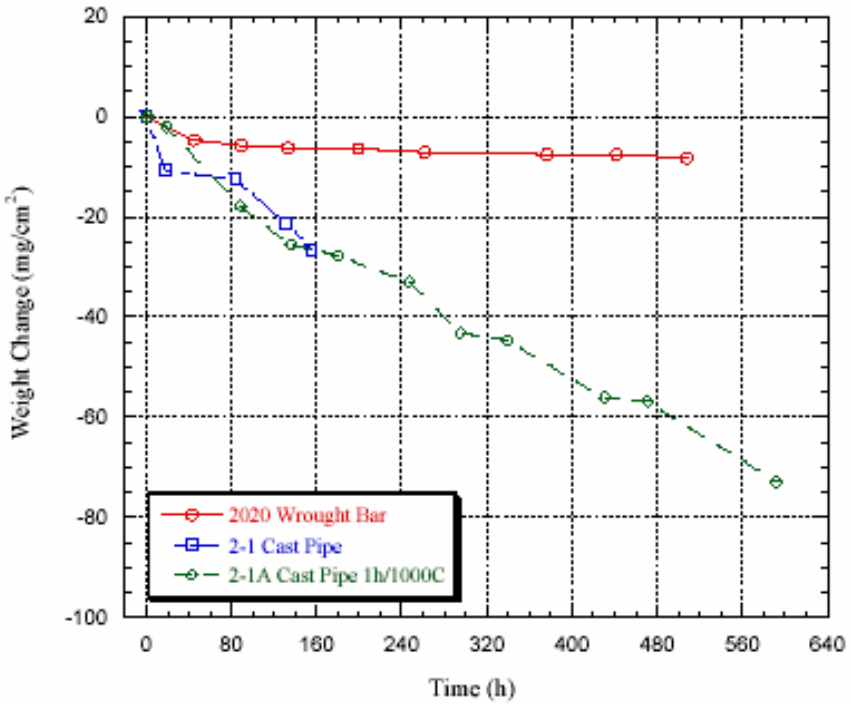

Figure 41: Alloy 2020, supplied by Supplier A, showed over a factor of 4 less weight change in molten zinc as opposed to type 316L. Performance of 2020 is very similar to that of alloy 2012.

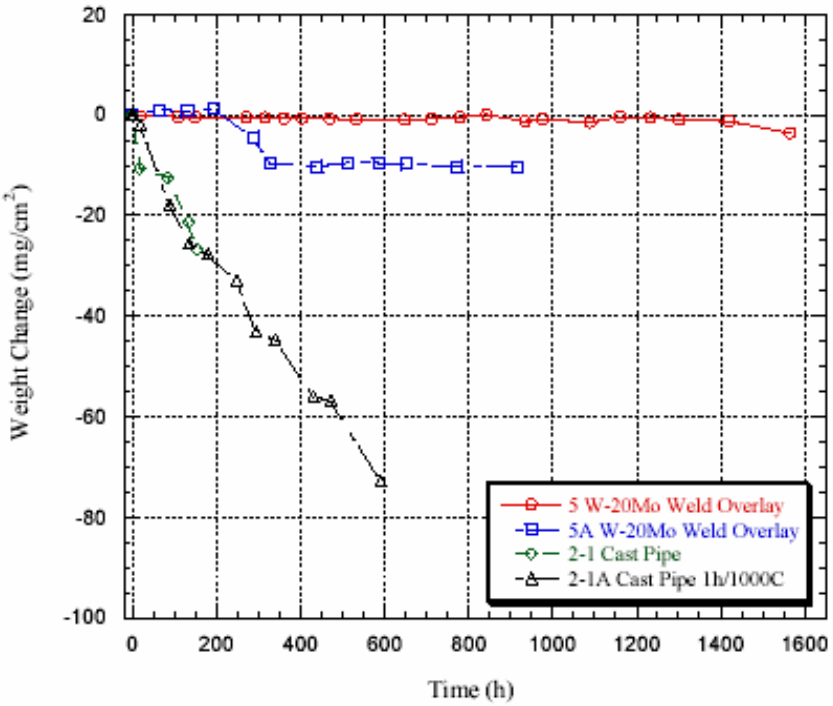

Figure 42: The weld overlay of W-20 Mo on carbon steel has shown exceptional performance in molten zinc at 465°C as opposed to type 316L.

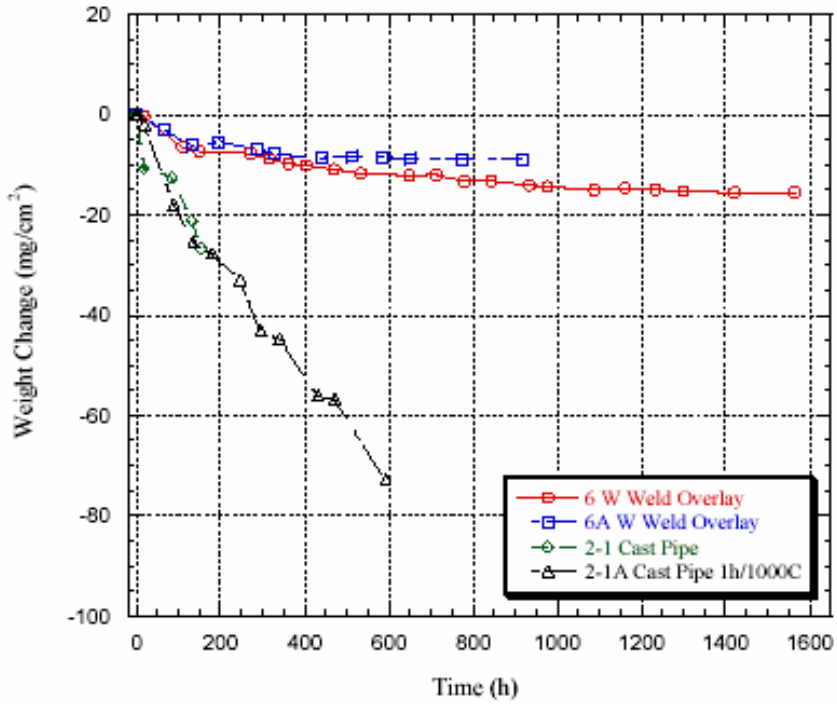

Figure 43: The weld overlay of tungsten on carbon steel has shown good

The ACD ceramic, supplied by Vesuvius, showed no corrosion attack in molten zinc at 465ºC (Figure 44). Based on data for ORNL alloy 4 series, aluminum weld overlay was tested in the preoxidized condition of D2 tool steel (Figure 45). Data up to

350 h showed that this approach may be worth pursuing further.

A sample of double carbide (DC) of WC/Co-Ni-Cr-Mo, when tested as monolithic material in molten zinc at 465ºC (Figure 46), did not perform well.

The following points can be summarized from the results presented in this section:

1. Large number of materials was tested for their molten zinc corrosion response under static conditions at 465ºC.
2. Materials tested were monolithic alloys, preoxidized alloys, weld overlays, and cermets.
3. Among the monolithic alloys, an Fe-20Cr-6.5% Al alloy (4-2) looks very promising in the preoxidized condition of 1100ºC for 2 h.
4. Among monolithics, both alloys 2012 and 2020 look promising.
5. Among weld overlays, W-20% Mo looks extremely good in the as-welded condition.
6. Aluminum weld overlaid on D2 alloy (Fe-12% Cr) after preoxidation at 1100ºC for 2 h looks promising.
7. Tests on DC tungsten carbide are not encouraging.
8. Stellite 6 was just gone in test and did not perform well for corrosion.

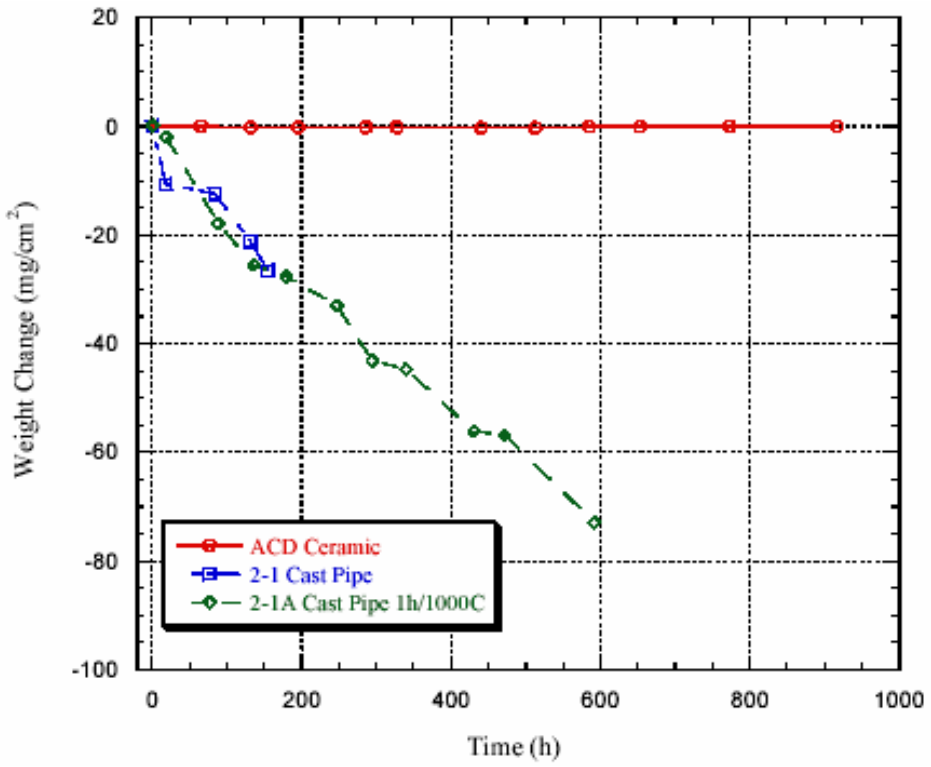

Figure 44: ACD ceramic from Vesuvius has shown no wetting when tested in molten zinc.

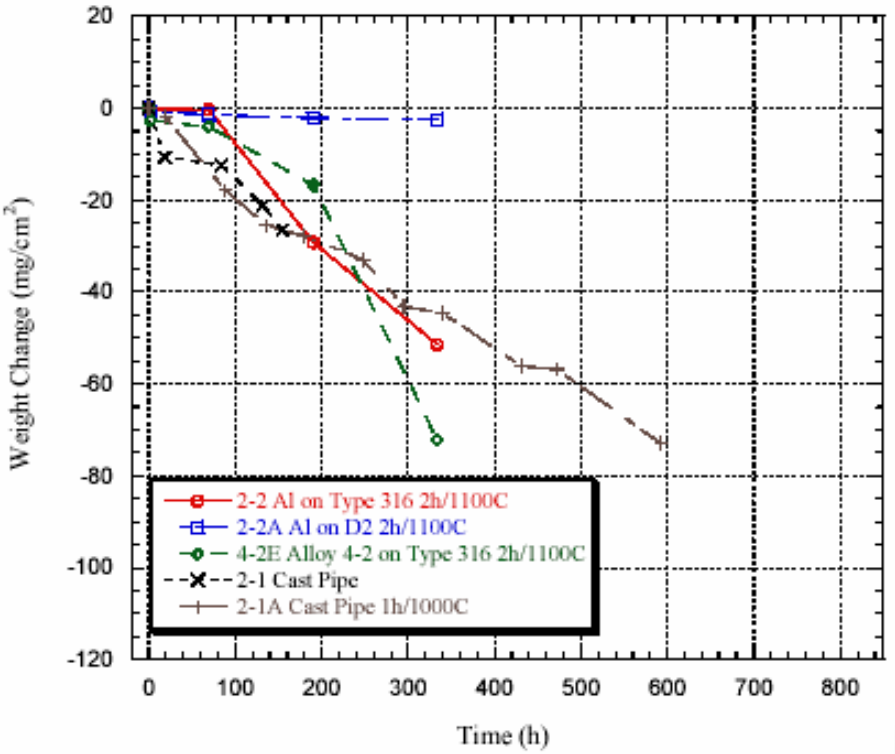

Figure 45: Weld overlay of aluminum on D2 steel, in the preoxidized condition in molten zinc at 465°C, is showing good promise as opposed to type 316L and D2.

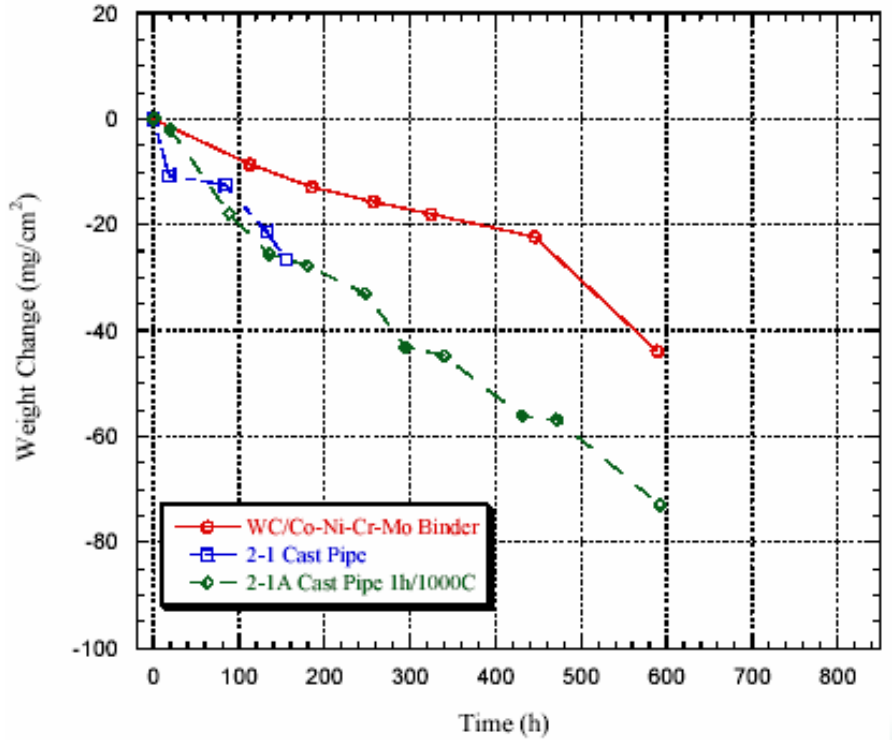

Figure 46: DC carbide in molten zinc at 465°C is showing poor performance.

Sub-task 4.1.2 Series I In-plant corrosion Testing

These materials were tested by static immersion in the currently operating galvanize or galvalume line of our project partners. Steel partner B and steel partner D are operating galvanizing lines, steel partner C is operating a galvannealing line and steel partner E and steel partner F are operating Galvalume lines. The samples are long thin strips and were affixed to a portion of the bath such that it did not interfere with the normal coating operations, as seen in
Figure 47.

Figure 47: Static corrosion specimens coming out of the industrial bath

The samples are long thin strips of either the substrate material, CF3M, or the substrate spray coated or laser coated with the tungsten carbide coating. Results from these tests are as follows:

Corrosion in GI/GA Bath The corrosion rates of the alloys were calculated based on the data at 1 inch from the bottom of the specimens. Figure 48 illustrates the corrosion rates of the base alloys and coating in GI/GA bath. There is no measurable thickness change for Stellite 6 specimens immersed up to 4 weeks in different baths. In the meantime, the corrosion rate of CF-3M alloys is around 3.5×10^{-3} in/week for all the four GI/GA bathes in this investigation. The corrosion rate of Spray-WC coating is around 1.9×10^{-4} in/week, which is about 1/18 of the corrosion rate of CF-3M.

Corrosion in GL Bath The corrosion rates of the alloys in Galvalume bath are shown in Figure 49. The corrosion rate of Stellite 6 is about 75% of CF3M.

Uniform Dissolution vs. Selective Corrosion In general, weight loss method is often used to evaluate the pot hardware materials' corrosion resistance since it is simple and easy to conduct. There is a hidden assumption of this method that the corrosion is a uniform dissolution process and that the lesser the material is lost, the better corrosion resistance it offers. However, the results from this investigation show that there are two kinds of corrosion. The SEM/BSI picture of Stellite 6 after immerging in GL bath for 4 weeks is shown in Figure 51. The right corner is Stellite 6 alloy and the freezing bath is on the left hand. There is only one intermetallic layer between the bath and the alloy, which indicates that the corrosion of Stellite 6 in GL bath is a uniform dissolution

process. However, in contrary to the alloy in GL bath, the corrosion of Stellite 6 in GI/GA bath is a selective-corrosion reaction. As shown in Figure 50, Fe and Al in the bath will segregate toward the alloy and react with the matrix to form an intermetallic compound. Cr and Co in the alloy will diffuse out of the alloy and react with the molten metal. Therefore, weight loss method is not a valid corrosion measurement method under this condition, because the procedure is not a uniform dissolution process.

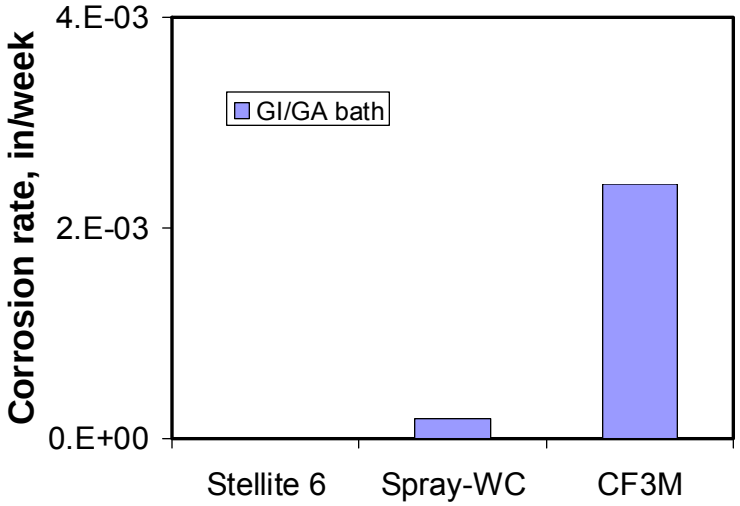

Figure 48: Corrosion rates of the alloys in GI/GA bath

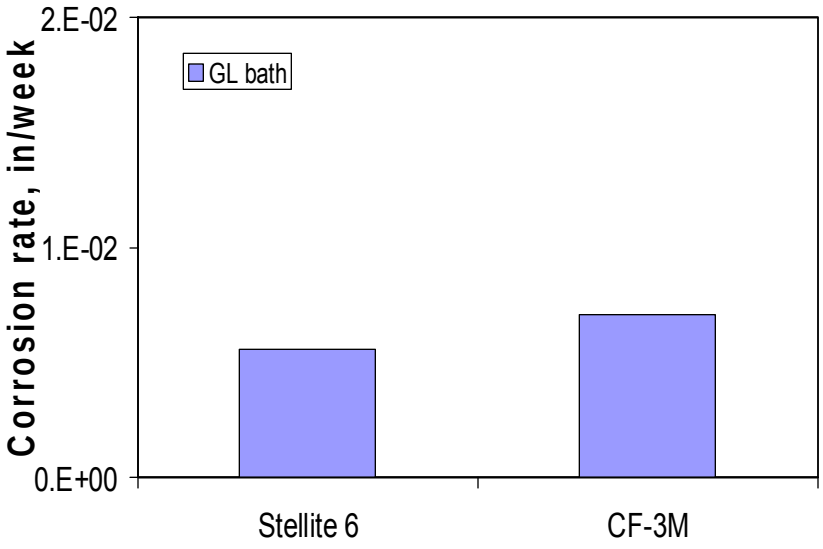

Figure 49: Corrosion rates of the alloys in GL bath

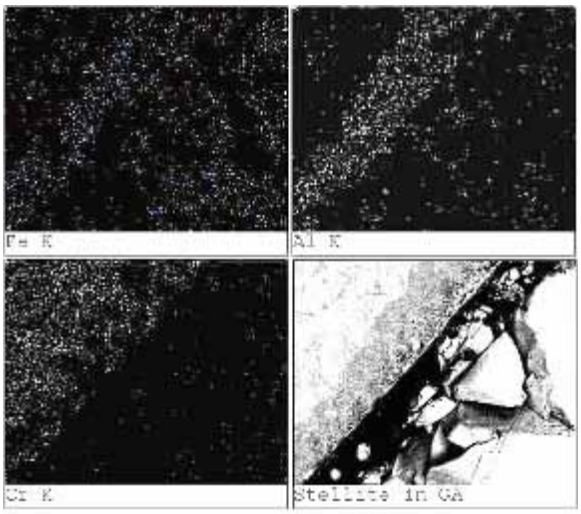

Figure 50: Elemental map of Stellite 6 in GA bath

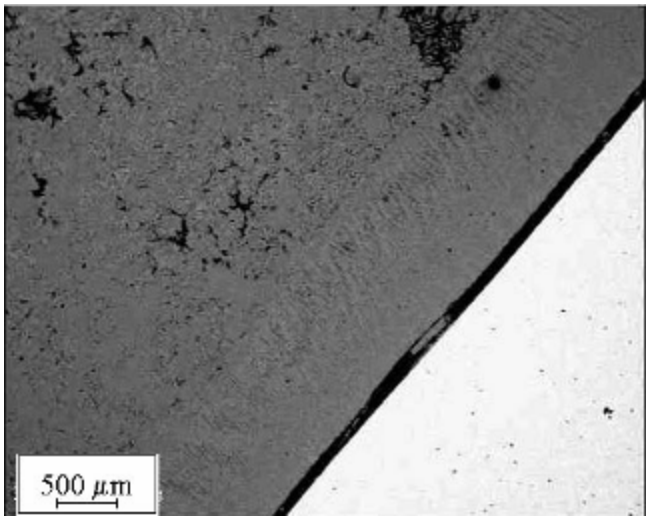

Figure 51: Stellite 6 in GL bath for 4 weeks (SEM/BSI)

Sub-task 4.1.3 Series I Lab-scale wear testing (small scale)

A small laboratory scale zinc-pot bearing materials tester was designed and constructed at West Virginia University with the purpose of providing reliable friction coefficient and wear rate data. The design objectives were:

a) Provide repeatable friction coefficient and material wear rate data for a variety of zinc pot bearing materials.

b) Minimize cost to prepare, install and analyze test samples.

c) Test sample geometry selected was a 25.4-mm (1-inch) ball mounted in a spindle that rotates on a stationary sample with a narrow seat machined into it

at a 45-degree contact angle.

d) Automate data acquisition by using high sample rate.

e) Provide pneumatic cushioning of stationary sample so as to eliminate vibration and load changes and simplify load adjustment.

f) Use small stainless steel test cups to mount the stationary sample, which is then filled with zinc taken from an actual galvanizing bath.

g) A vertical mill with a water-cooled spindle, was used to rotate a 25.4-mm ball sample on a 45º sloped seat at controllable load and RPM.

WVU's small-scale bearing materials tester was designed to simulate actual steel mill galvanizing line machine bearing operating conditions, as shown in Figure 52. Operational conditions for galvanizing lines 3, 4 and 5 as provided by steel partner D are provided in Table 10.

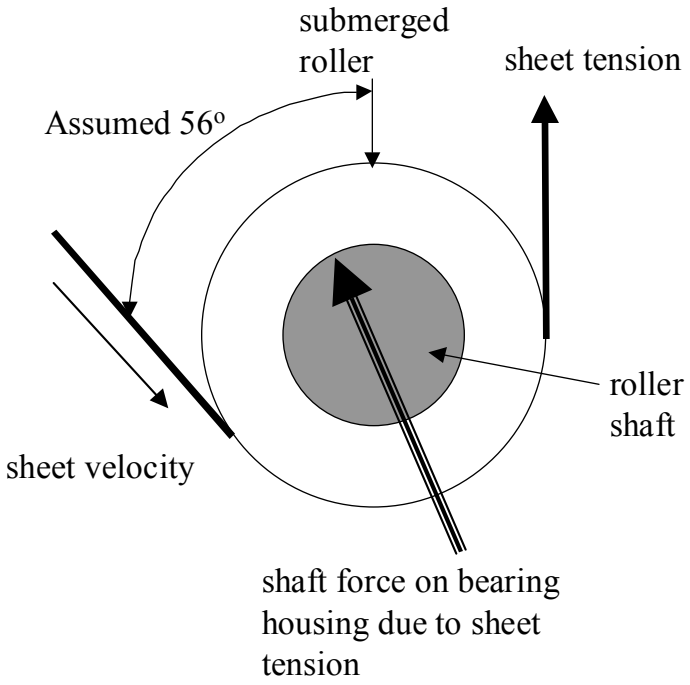

Figure 52: Schematic of Galvanizing Line Roller and Bearing

	Line #3	Line #4	Line #5
Pot liner	Ceramic Brick	Ceramic Brick	Ceramic Brick
Zinc pot chemistry	0.08-0.22% Al	0.15-0.22% Al	0.08-0.22% Al
Temperature	471 – 593°C	482 – 504°C	471 – 482°C
Sheet width	0.610 – 1.24 m	0.610 – 1.07 m	0.610 – 1.24 m
Sheet thickness	0.711 – 4.19 mm	0.239 – 0.711 mm	0.305 – 1.14 mm
Sheet tension (T_s)	14,234 – 22,241 N	4,448 – 8,896 N	14,234 – 21,351 N
Sheet velocity	0.254 – 1.52 m/sec	0.508 – 2.08 m/sec	0.559 – 2.79 m/sec
Bottom Roller Characteristics			
Bearing life	7 - 14 days	7 - 14 days	7 - 30 days
Bearing materials	316L S.S.	316L S.S.	316L S.S
Outside diameter (D_R)	0.610 m	0.508 m	0.508 m
Shaft diameter (D_B)	0.133 m	0.0984 m	0.0984 m
Bearing length	0.102 m	0.102 m	three 0.102 m long, 0.0254 m wide inserts
Each bearing has projected area (A_B)	0.0135 m^2	0.0100 m^2	0.00622 m^2

Table 10: Steel partner D operating parameters for Lines 3, 4, and 5.

To correlate steel partner D operational data to the WVU small-scale zinc-pot bearing materials tester, an average sheet entry angle of 56-degrees from vertical was assumed. Based on the roller and bearing configuration shown in Figure 52, each of the two bearings at either end of the roll carries a load F_B related to the sheet tension, T_S, by:

$$F_B = T_S * [\cos(0.5 * 56°)] = 0.88 * T_S \quad (1)$$

Bearing contact pressure was determined by a ratio of bearing force, F_B, to the contact area of one of the two bearings.

$$P_B = \frac{F_B}{A_B} = 0.88 * \left(\frac{T_S}{A_B} \right) \quad (2)$$

The bearing contact velocity is lower than the sheet velocity, which equals the roller surface velocity. Contact velocity is found by a ratio of the bearing shaft diameter to the roller diameter as follows:

$$V_B = V_{Sheet} * \left(\frac{D_B}{D_R} \right) \quad (3)$$

With the use of equations (1) through (3), galvanizing line bearing pressures and velocities were determined, as shown in Table 11.

	Line #3	**Line #4**	**Line #5**
Projected contact area of each bearing, A_B (m^2)	0.0135	0.0100	0.00622
Line speed (m/sec)	0.254 – 1.524	0.508 – 2.08	0.559 – 2.79
Line tension, T_S (N)	14,234 – 22,241	4,448 – 8,896	14,234 – 21,351
Bearing contact velocity, V_B (m/sec)	0.0556 – 0.333	0.0986 – 0.404	0.108 – 0.541
Bearing contact pressure, P_B (kPa)	924 – 1,448	393 – 786	2,020 – 3,034

Table 11: Steel Partner D Converted Galvanizing Line Operational Conditions

WVU's small-scale zinc-pot bearing materials tester rotates a 25.4-mm diameter ball against a matching stationary seat, machined as shown in Figure 53. This design is based on a 45-degree contact angle or a mean contact diameter of 17.96-mm. A 15.88-mm hole is machined in the center of the seat and the resulting outer diameter of the contact area is 19.81-mm. The resulting horizontal projected area A_{hor} = 110.3 mm.

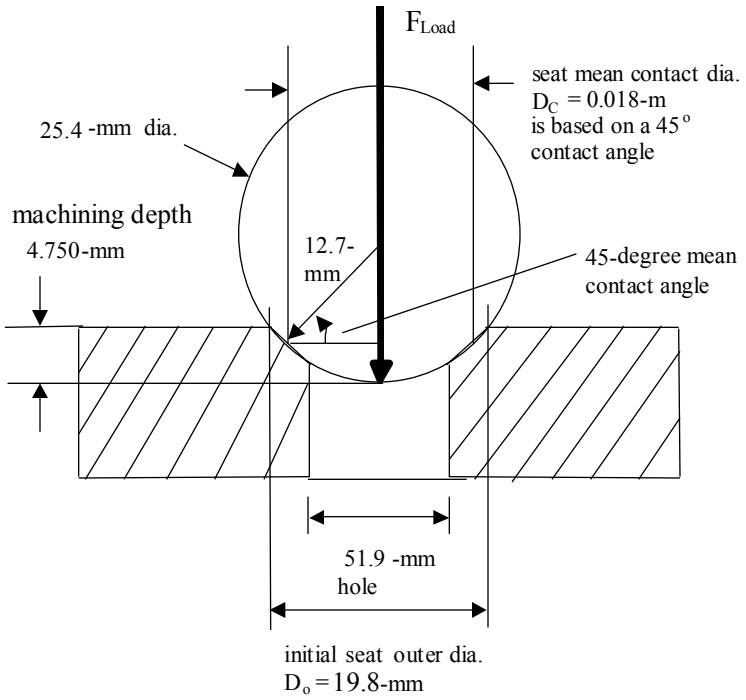

Figure 53: Ball and Seat Specimen Diagram

To duplicate steel mill bearing operating pressures, P_B, in the WVU small-scale zinc-pot bearing materials tester the ball specimen containing spindle was loaded to $F_{spindle}$ to produce the desired bearing contact pressure, P_C, based on the initial ball on seat contact area, $A_{average}$.

$$F_{spindle} = P_C * A_{average} \quad (4)$$

Based on the 0.018-m seat mean contact diameter, the contact velocity, V_C, for the sample specimens was determined.

$$Spindle\,RPM = 60*\left[V_C(m/s)/(\pi*0.018m)\right] = V_C(m/s)*1061 = V_c(inch/\sec)*27 \quad (5)$$

With the use of the above equations, the operational data ranges provided by steel partner D were converted to equivalent operational data ranges for WVU's small-scale zinc-pot bearing materials tester. The data ranges are shown in
Table 12.

	Line #3	Line #4	Line #5
Line Speed (m/sec)	0.254 – 1.524	0.508 – 2.08	0.559 – 2.79
Line Tension (N)	14,234 – 22,241	4,448 – 8,896	14,234 –21,351
***Bearing Contact V_C (m/sec)**	**0.0556 – 0.333**	**0.0986 – 0.404**	**0.108 – 0.541**
***Bearing Contact P_C (kPa)**	**924 – 1,448**	**393 – 786**	**2,020 – 3,034**
Tester Spindle RPM	59.1 – 354	105 – 429	114 – 575
Tester Ball Load (N)	102 – 160	43.2 – 86.3	222 – 333

Table 12: Steel Partner D Operational Ranges Converted to WVU's Zinc Pot Bearing Materials Tester (* operating conditions are common to both)

A vertical mill/drilling machine used to drive WVU's small-scale zinc-pot bearing materials tester provided the constant RPM and load needed. A 2500-Watt melting pot was used to maintain tin at controllable temperature. An aluminum disc covering the melting pot is suspended on a ball bearing track. The disc suspends the cup holder within the molten tin. The friction torque is transmitted from the seat sample to the test cup and from there to the ball bearing supported aluminum disc. A bracket attached to this disc transfers the friction torque to a strain gage beam, connected to a data logging program. The water-cooled aluminum ring with the ball bearing track is supported by three linear bearings which allow it to move up and down friction free while floating on a pneumatic cushion, which helps to maintain constant load and dampen vibrations. The pneumatic cushion is supported by three load measuring strain gage balances.

This spindle containing the ball sample is mounted into a R-8 mill cullet and is partly made of thin walled stainless steel to minimize heat loss from the sample cup and to hold the test specimen in place. A rivet is used to key the ball sample to the thin walled tube. To protect the bearings in the vertical mill, the upper end of the spindle was water cooled. This was accomplished by spring loading a stationary water cooled disc to ride against a similar aluminum disc pressed on the rotating spindle. The hollow spindle also allows using a steel rod to push the ball sample out of the spindle after testing. A variable speed motor allows adjustment of the spindle rotation rate to the nearest 1 RPM.

The seat specimen was secured in the stainless steel cup by the use of a stainless steel strut channel machined to clamp the sample in place. This channel was secured with a bolt to the specimen test cup, see Figures 54 and 55, respectively. Both the test cup and strut channel were coated with Boron Nitride to prevent corrosion during testing.

Figure 54: Stainless Steel Strut Channel and Seat

Figure 55: Stainless Steel Strut Channel and Seat Bolted into Specimen Cup

Four channels of data were recorded during bearing material tester operation. These include: load, friction torque, spindle RPM and test cup temperature. The output of these four data channels was saved by use of a QBasic™ program that writes all collected data to a floppy disk. Figure 56 shows the WVU small-scale zinc-pot bearing materials tester in operation.

Figure 56: WVU's Small-Scale Zinc-Pot Bearing Materials Tester

With the collected data for torque and load it was possible to calculate the sliding friction coefficient. The first step in this computation was to remove the gains from the voltage signals by dividing the signal by its respective gain. Next, the voltage signal is transformed to the proper units using the calibration constants for the load and torque. These constants were determined by calibration of the various strain gages, load cells, RPM meter and thermometer on the WVU small-scale zinc-pot bearing materials tester. To allow removing any erroneous data points from the recorded signal, an over-lap save method was employed.

The ball sample rotates on a stationary seat at a 45-degree contact angle for self centering. This 45-degree seat angle increases both contact area and spindle normal force component by a factor of √2, thus does not effect contact velocity. The calibrated strain gage beam has a moment arm $\ell_{\text{gage}} = 0.171$-m. The sample seat friction torque produces a force on the strain gage beam $F_{\text{beam with gage}}$. With the data converted and averaged, the friction coefficient, μ_F, can be calculated from:

$$\mu_F = \frac{Torque\, Q = r_{beam} * F_{beam\ with\ gage}}{F_{spindle} * \sqrt{2} * (r_{mean} = 0.018/2)} = \left(\frac{F_{beam\ with\ gage}}{F_{spindle}} \right) * \left(\frac{2 * 0.171}{0.018 * \sqrt{2}} = 13.5 \right) \quad (6)$$

The friction power dissipation rate for the ball/seat system is the product of the ball/seat load, contact velocity and friction coefficient. The friction power dissipation rate can be determined for each test as follows:

$$Friction\ Power = V_c * F_{spindle} * \sqrt{2} * \mu_F \quad (7)$$

Wear of the various test materials was determined by measuring the loss of seat material as a function of time at a prescribed set of test conditions. To determine the loss of material, the average initial horizontal seat width, W_i, was measured before the start of the test. The measurement was done with an 20X measuring microscope capable of measuring to the nearest 0.025-mm. The seat measurements were taken in four locations, North, South, East and West, as seen in Figure 57. These four measurements were then averaged to arrive at an average seat width, W_i.

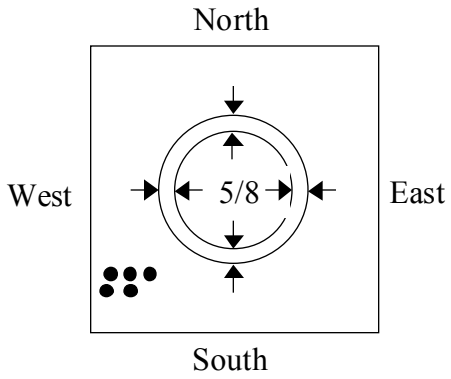

Figure 57: Measurement Locations on Seat Specimen

The amount of material lost from the sloped seat is a function of the wear depth. Wear depth is calculated by the average gain in seat width, $(D_f - D_i)/2 = \Delta W$, by the square root of 2 as follows:

$$Wear\ Depth = \frac{\Delta W}{\sqrt{2}} \quad (8)$$

This depth accounts for the amount of material loss on the sloped seat. A diagram of this is shown in Figure 58. The horizontal projected seat area, A_{hor}, before and after the test can be derived from the initial and final seat radii, r_i and r_f, respectively.

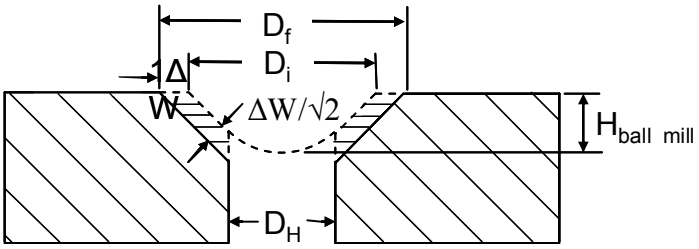

Figure 58: Wear location of seat specimen

$$A_{hor} = \pi\left[(r)^2 - \left(D_H/2\ mm\right)^2\right] \tag{9}$$

(3.9)

The actual area of the sloped seat, $A_{average}$, was determined using the initial seat width.

$$A_{average} = \frac{\pi}{4}\left[\left(D_i + 2*\Delta W\right)^2 - \left(D_i\right)^2\right]*\sqrt{2} \tag{10}$$

The mass wear rate on the sloped surface of the stationary seat specimen can be calculated from the increase in seat width, ΔW. First, the volume removed on the stationary seat due to the rotating ball end volume, V_S, can be found as a spherical segment. The volume removed in the stationary seat by the rotating ball end volume of radius R_{ball} is a function of the depth of travel $H_{ball\ mill}$ used to machine the test sample seat.

$$V_s = \pi\left(H_{ball\,mill}^2 * R_{ball} - \frac{H_{ball\,mill}^3}{3}\right) \tag{11}$$

The volume removed due to machining of the ball/seat is different than that of a spherical segment since a hole of diameter D_H is present in the center of the seat. This reduces the volume of the spherical segment by another height segment of H_o. The height of this segment can be calculated as:

$$H_o = R_{ball} * \left(1 - \cos\left(\sin^{-1}\left(\frac{D_H/2}{R_{ball}}\right)\right)\right) \tag{12}$$

The volume removed due to the cylindrical center hole, V_H, of diameter D_H and a height of $H_{ball} - H_o$ would be:

$$V_H = \frac{\pi * D_H^2}{4} * \left(H_{ball\,mill} - H_o\right) \tag{13}$$

Based on the stationary seat geometry with a 45-degree contact angle, the height of the cylindrical projection into the ball/set, $H_{ball\ mill}$-H_o, is equal to the initial seat width, W_i. The volume of material removed due to machining, $V_{machining}$, of the stationary seat specimen to its final dimensions of would be found as:

$$V_{machining} = V_S - \pi * \left(H_o^2 * R_{ball} - \frac{H_o^3}{3} \right) - \frac{\pi * D_H^2}{4} * W_i \tag{14}$$

The final volume of the seat region, V_f, would was found using the final seat width, W_f, resulting in the following:

$$V_f = V_S - \pi * \left(H_o^2 * R_{ball} - \frac{H_o^3}{3} \right) - \frac{\pi * D_H^2}{4} * W_f \tag{15}$$

Wear volume, V_{wear}, is the difference between the final volume and the volume removed due to machining as:

$$V_{wear} = V_f - V_{machining} \tag{16}$$

Multiplied by material density provides a mass loss. By dividing by test duration, t, gives stationary seat wear rate, WR_S.

$$Wear\ Rate\ (seat) = WR_S = \left(\frac{\Delta W}{\sqrt{2}} \right) / t \tag{17}$$

The mass wear rate of the stationary seat sample, WR_{SM}, may be determined using the volume removed due to wear, V_{wear}, the material density and the test duration.

$$WR_{SM} = \left(\frac{V_{wear}}{t} \right) * \rho_{material} \tag{18}$$

The rotating ball sample was weighed before and after the test to determine the mass loss due to wear. Using the initial and final mass, m_i and m_f, respectively, and the test time, the wear rate of the ball sample was determined.

$$Wear\ Rate\ (ball) = WR_B = \left(m_f - m_i \right) / t = \Delta m / t \tag{19}$$

With the use of material density, the above mass wear rate can be converted to a volume loss wear rate for the rotating ball sample.

Rotating Ball Specimen Material	Stationary Seat Specimen Material	Wear Rate of Stationary Seat (mm/day)	Sliding Friction Coefficient of Material Pair
316L stainless steel	316L stainless steel	3.07	0.20
Stellite 6	Stellite 6	1.80	0.16
Laser-Clad Tungsten-Carbide Overlay	ACD Wearguard Ceramic	0.0561	0.30

Table 13: Series I wear rate and sliding friction coefficient tested at a contact pressure of 1379 kPa (psi) and contact velocity of 0.226 m/sec (RPM) in a 460 C molten zinc bath.

For Series I testing, the wear rate for materials used in existing commercial lines was determined for baseline performance data. During this process, a significant property was discovered from the numerous trial runs performed on various material combinations. It was determined that the wear rate are strong functions of the contact pressure and velocity, but NOT correlated with the sliding coefficient of friction. Comparison of all the data from each series will be shown in Series II and III testing results.

Pressure and velocity wear correlation of Cobalt 6

Cobalt 6 is a cobalt-based superalloy currently used for galvanizing line submerged hardware. Table 14 shows the composition of the Cobalt 6 superalloy. Cobalt 6 is very similar in composition to Stellite 6, a Task 4.1 Material Tests: Series I alloy, and was selected to use as a base-line material to which other promising materials could be compared.

Alloying Element	Co	Si	Fe	Ni	Cr	W	C	Mn	Mo
Mass Percent in Alloy	58	0.7	3.0*	2.5	30	4.0	1	1.4	1.5*
* maximum mass percent in alloy									

Table 14: Composition of Cobalt 6

Wear tests were performed on Cobalt 6 to determine the effects of contact pressure and contact velocity on wear rate while submerged in a molten zinc bath of typical galvanizing composition at 460°C. Prior to testing, all provided samples were pre-polished and prepared for testing. The tests sample seat widths were measured before and after testing using an optical microscope to the nearest 0.025-mm and the ball samples were weighed to the nearest 0.001-g using a digital balance. The contact pressures, contact velocities and wear rate data obtained from these tests are shown in Table 15.

Test Number	Contact Pressure, P_C (kPa)	Contact Velocity, V_C (m/sec)	Test Duration (hours)	Seat Wear Rate, WR_S (mm/day)	Ball Mass wear rate, WR_B (g/day)	Seat Mass wear rate, WR_{SM} (g/day)
C1	517	0.0705	20	0.055	-0.077	-0.70
C2	1034	0.0705	20	0.177	-0.248	-0.331
C3	1551	0.0705	20	0.321	-0.479	-0.446
C4	517	0.141	20	0.204	-0.287	-0.326
C5	1034	0.141	20	0.491	-0.771	-0.926
C6	1551	0.141	20	0.938	-1.668	-1.502
C7	517	0.212	20	0.309	-0.453	-0.407
C8	1034	0.212	20	0.782	-1.351	-1.284
C9	1551	0.212	20	1.395	-2.824	-3.240
C10	689	0.0705	6.6	0.115	-0.152	-0.148
C11	689	0.0705	13.3	0.109	-0.149	-0.165
C12	689	0.0705	20	0.118	-0.165	-0.151
C13	689	0.141	6.6	0.314	-0.436	-0.374
C14	689	0.141	13.3	0.333	-0.484	-0.444
C15	689	0.141	20	0.313	-0.462	-0.419
C16	689	0.212	6.6	0.393	-0.541	-0.611
C17	689	0.212	13.3	0.419	-0.615	-0.568
C18	689	0.212	20	0.384	-0.596	-0.505

Table 15: Collected Data from Cobalt 6 Wear Rate Correlation Tests

The effect of contact pressure on the stationary seat wear rate of Cobalt 6 is shown in Figure 59. These tests were performed with contact pressures ranging from 517 to 1551 kPa and contact velocities ranging from 0.0705 to 0.212 m/sec, all for a 20 hour test period and are labeled as tests C1 through C9, C12, C15 and C18 in Table 15. As seen in Figure 59, the seat wear rate appears to be non-linear with the contact pressure. When a linear fit was applied to the data, it was determined that seat wear rate, WR_S, is proportional to $P_C^{1.39}$. This curve fitted linear relation is shown in Figure 60.

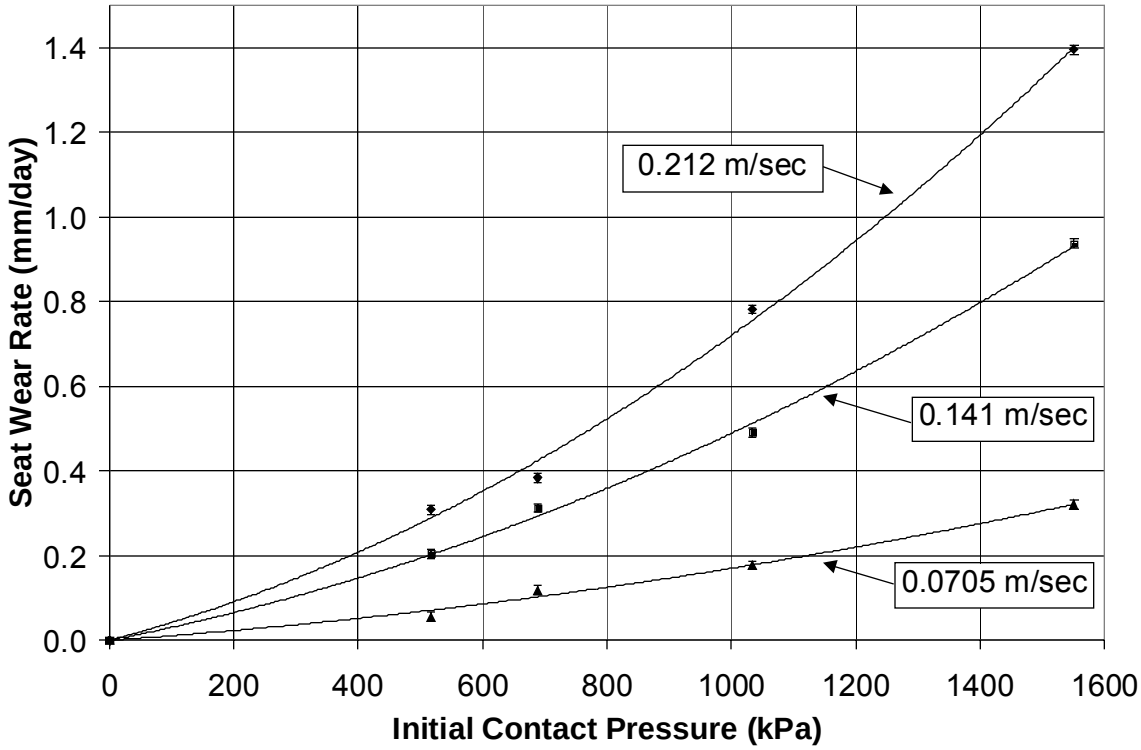

Figure 59: Contact Pressure Effects on Seat Wear Rate of Cobalt 6

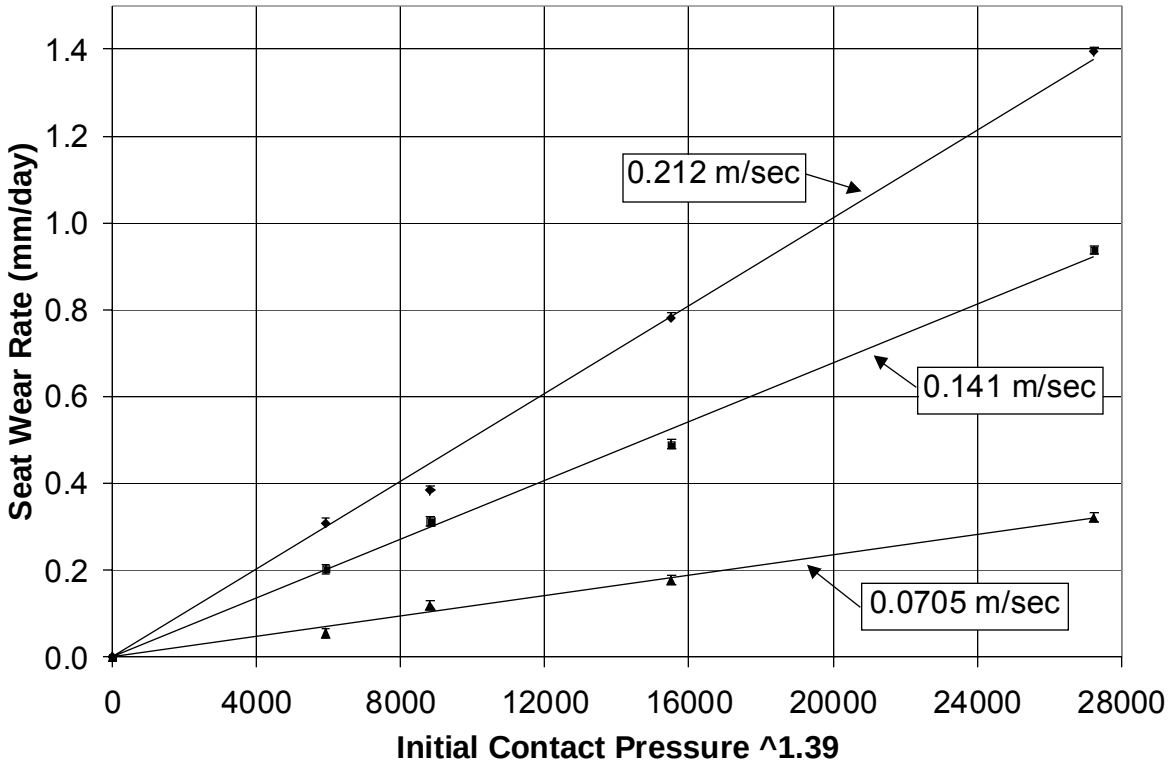

Figure 60: Seat Wear Rate of Cobalt 6 as a Function of Contact Pressure Raised to the Power of 1.39

The effects of contact velocity on seat wear depth were studied for Cobalt 6. Tests were performed over three even time intervals up to 20 hours at three contact velocities of 0.0705, 0.141 and 0.212 m/sec with a constant contact pressure of 689-kPa and are labeled as tests C10 through C18 in Table 15. Figure 61 shows the effect of contact velocity on seat wear depth over time. As this Figure shows, the seat wear depth is linear with time at a constant contact velocity, but non-linear over a range of contact velocities.

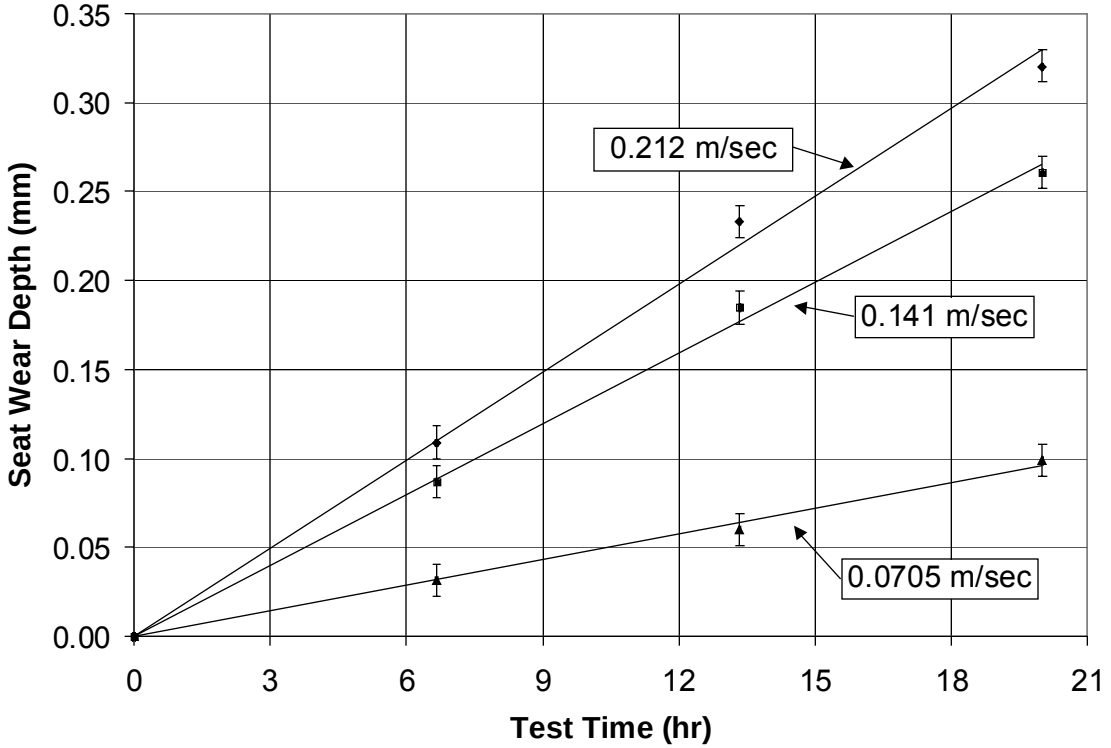

Figure 61: Effects of contact velocity over time on seat wear depth of Cobalt 6

A correlation between the contact pressure, contact velocity and seat wear rate was constructed. The construction of this curve fitted correlation was in the form:

$$WR_S = C_S * P_C^{\alpha} * V_C^{\beta} \tag{20}$$

The values determined for the three parameters, based on experimental data, were: α = 1.39, β = 1.45 and $C_S = 5.3*10^{-4}$. This resulted in a final correlation for the Cobalt 6 seat wear rate of:

$$WR_S\left[\frac{mm}{day}\right] = 5.3*10^{-4} * \left[P_C\left[kPa\right]\right]^{1.39} * \left[V_C\left[\frac{m}{\sec}\right]\right]^{1.45} \tag{21}$$

This correlation is shown graphically in Figure 62.

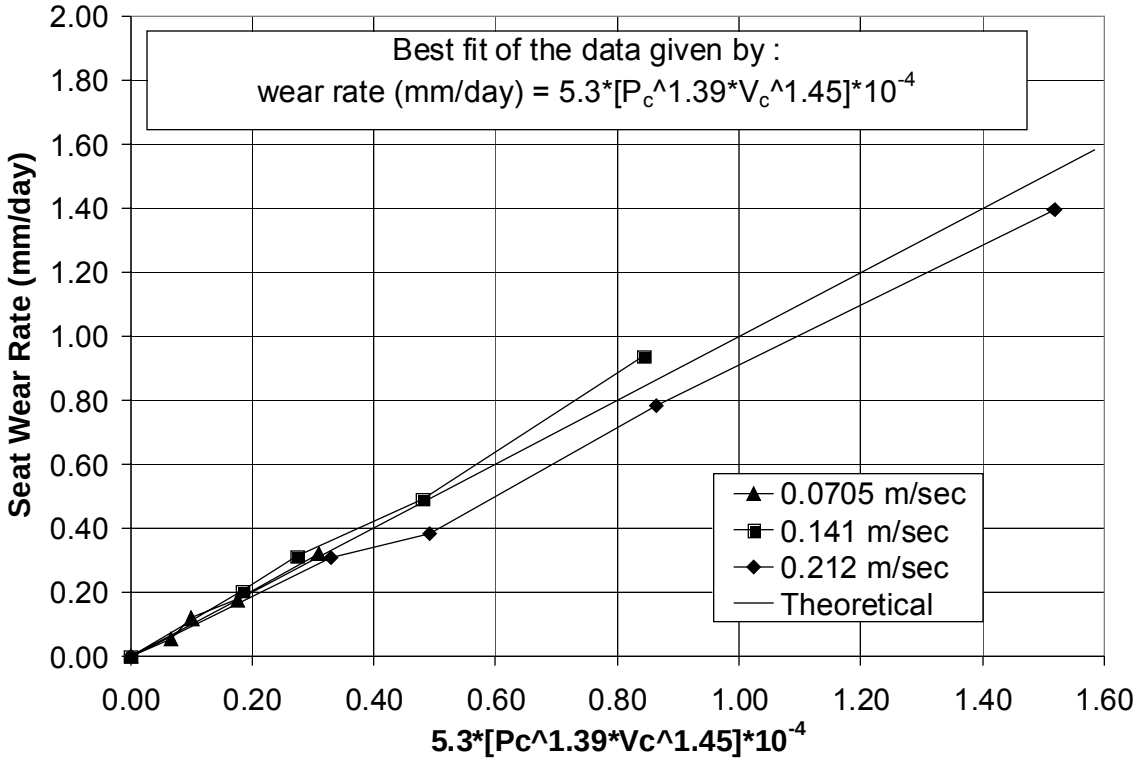

Figure 62: Cobalt 6 Seat Wear Rate as a Function of Contact Pressure and Contact Velocity

Next, a correlation was determined for the seat mass wear rate as a function of contact pressure and contact velocity. Using the density of Cobalt 6, as provided by the manufacturer of 0.00838-g/mm^3, the mass wear rate of the stationary seat was determined for each test. The calculated mass wear rates of the stationary seat specimen are shown in Table 15.

The effect of contact pressure on the mass wear rate, WR_{SM}, of the Cobalt 6 stationary seat is shown in Figure 63. These tests were performed with contact pressures ranging from 517 to 1551 kPa and contact velocities ranging from 0.0705 to 0.212 m/sec, all for a 20 hour test period and are labeled as tests C1 through C9, C12, C15 and C18 in Table 15. From this Figure, it appears that the mass wear rate of the seat is a non-linear function of the contact pressure. When a linear fit was applied to the data, it was determined that mass loss seat wear rate, WR_{SM}, is proportional to $P_C^{1.66}$. This curve fitted linear relation is shown in Figure 64.

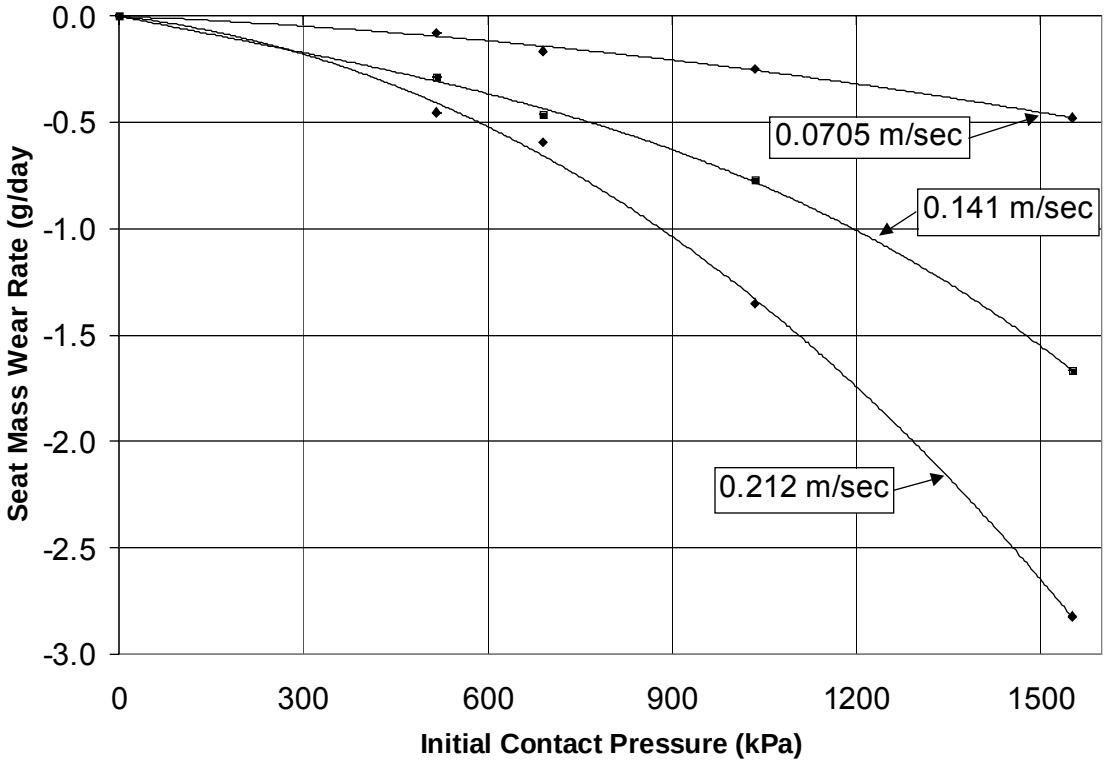

Figure 63: Mass Wear Rate of the Cobalt 6 Seat Sample as a Function of Contact Pressure

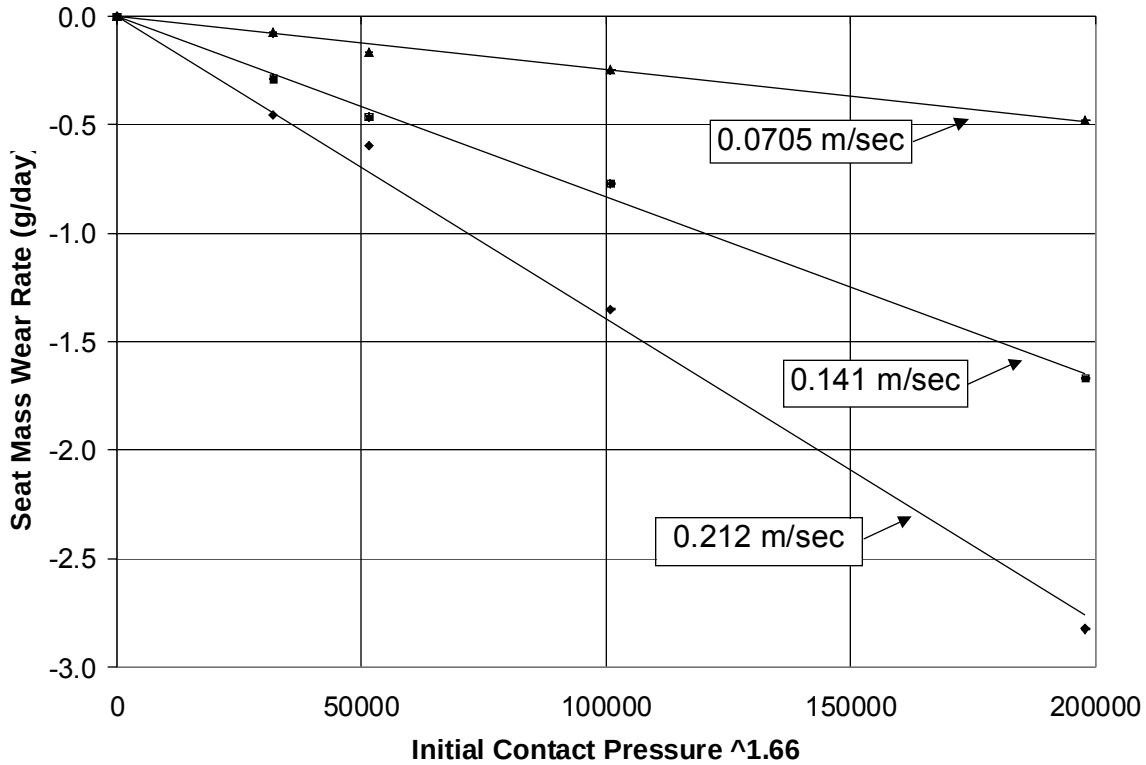

Figure 64: Mass Wear Rate of the Cobalt 6 Seat Sample as a Function of Contact Pressure Raised to

the Power of 1.66

The effect of contact velocity on the mass loss of the Cobalt 6 seat sample over time is shown in Figure 65. These tests correspond to tests number C10 through C18 in Table 15. As seen in Figure 65, the mass lost on the stationary seat specimen is linear with time at a constant contact velocity, but non-linear over a range of contact velocities.

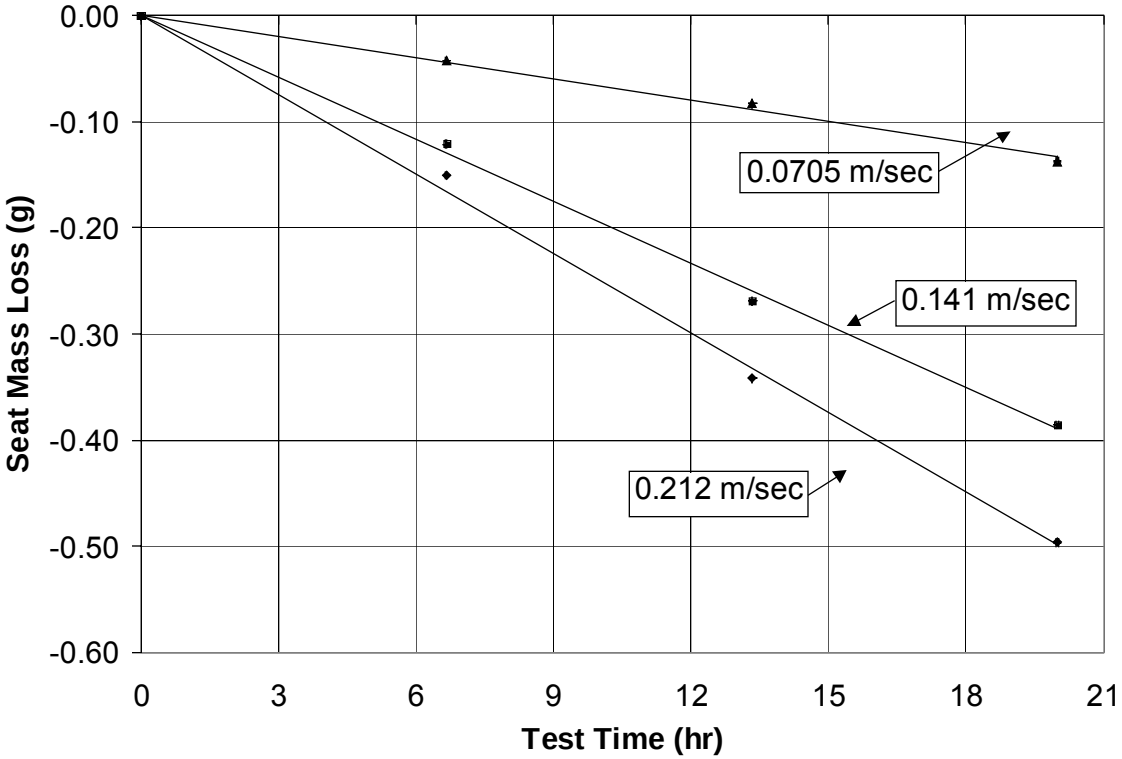

Figure 65: Effect of Contact Velocity Over Time on Mass Loss Rate of the Cobalt 6 Stationary Seat Sample

An overall correlation relating the effects of contact pressure and contact velocity to the seat specimen mass wear rate was constructed. This relation was of the form:

$$WR_{SM} = C_{SM} * P_C^{\alpha} * V_C^{\beta} \tag{22}$$

The values determined for these constants were $\alpha = 1.66$, $\beta = 1.58$ and $C_{SM} = -1.6*10^{-4}$. This relation is shown graphically in Figure 66. The final correlation for the stationary seat sample mass wear rate as a function of contact pressure and contact velocity was:

$$WR_{SM}\left[{}^{g}\!/_{day}\right] = -1.6*10^{-4} * \left[P_C\left[kPa\right]\right]^{1.66} * \left[V_C\left[{}^{m}\!/_{\sec}\right]\right]^{1.58} \tag{23}$$

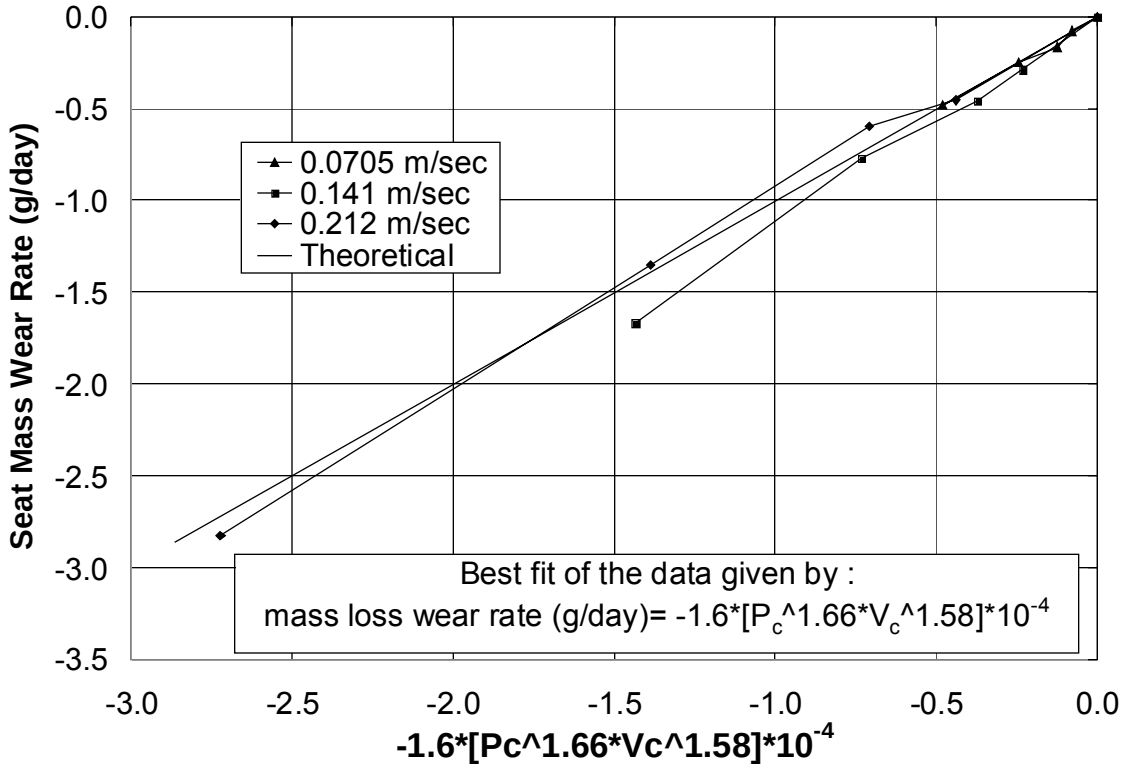

Figure 66: Cobalt 6 Seat Mass Wear Rate as a Function of Contact Pressure and Contact Velocity

With a correlation determined for the stationary seat specimen mass wear rate, the same type of correlation was applied to the Cobalt 6 rotating ball specimens used in the tests in Table 15. Figure 67 shows the effect of contact pressure on the mass wear rate of the rotating ball sample, which appears to be a non-linear function of contact pressure. This relation was fitted to a linear relation between contact pressure and mass wear rate of the ball sample as WR_B is proportional $P_C^{1.52}$. This relation is shown in Figure 68.

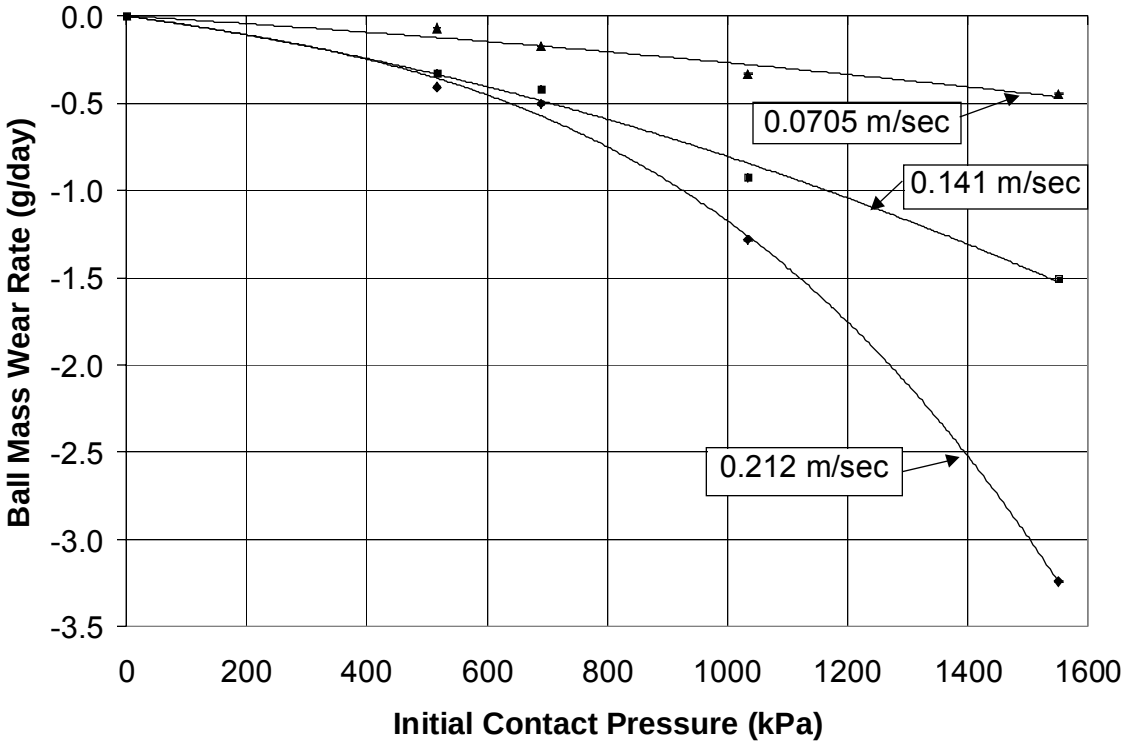

Figure 67: Effects of Contact Pressure on the Cobalt 6 Ball Sample Mass Wear Rate

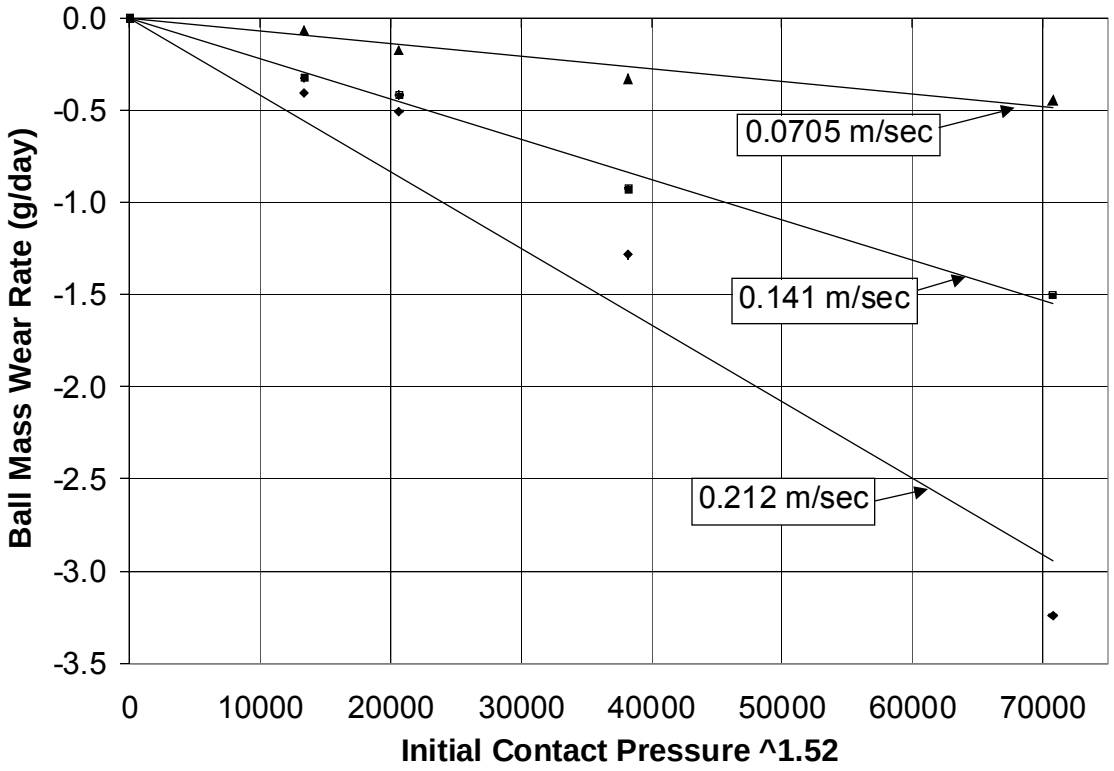

Figure 68: Mass Wear Rate of the Cobalt 6 Ball Sample as a Function of Contact Pressure Raised to the Power of 1.52

The effect of contact velocity on the mass loss rate of the Cobalt 6 rotating ball sample are shown in Figure 69. Tests were performed over constant time intervals at three different contact velocities at a constant contact pressure of 689-kPa and are test numbers C10 through C18 in Table 15. From this Figure, the mass loss rate of the rotating ball sample is linear with time at a constant contact velocity, but non-linear over a range of contact velocities.

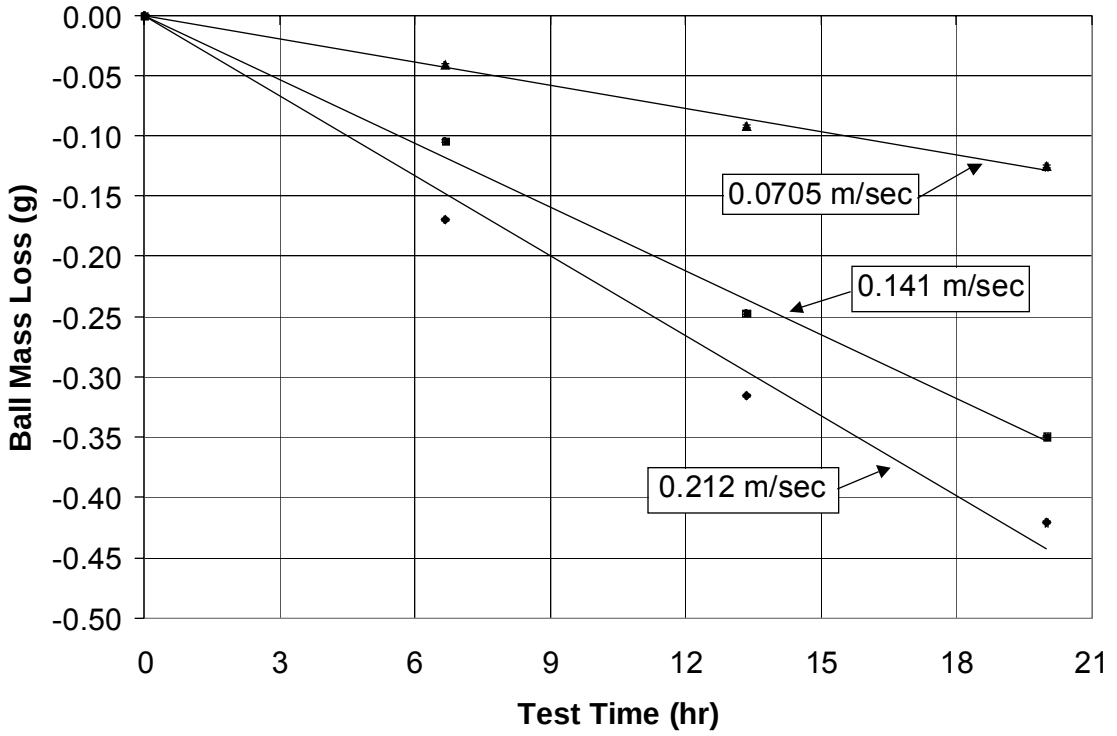

Figure 69: Effect of Contact Velocity Over Time on Mass Loss Rate of the Cobalt 6 Rotating Ball Sample

For the mass wear rate of the Cobalt 6 ball sample, an overall correlation was derived between contact pressure and contact velocity as a function of mass wear rate. A correlation was applied to a curve fitted data and was in the form:

$$WR_B = C_B * P_C^{\alpha} * V_C^{\beta} \tag{24}$$

The values determined for these constants were $\alpha = 1.52$, $\beta = 1.42$ and $C_B = -3.2*10^{-4}$. The final correlation for the rotating ball sample mass wear rate as a function of contact pressure and contact velocity was:

$$WR_B\left[g/day\right] = -3.2*10^{-4} * \left[P_C\left[kPa\right]\right]^{1.52} * \left[V_C\left[m/\sec\right]\right]^{1.42} \tag{25}$$

This relation is shown graphically in Figure 70.

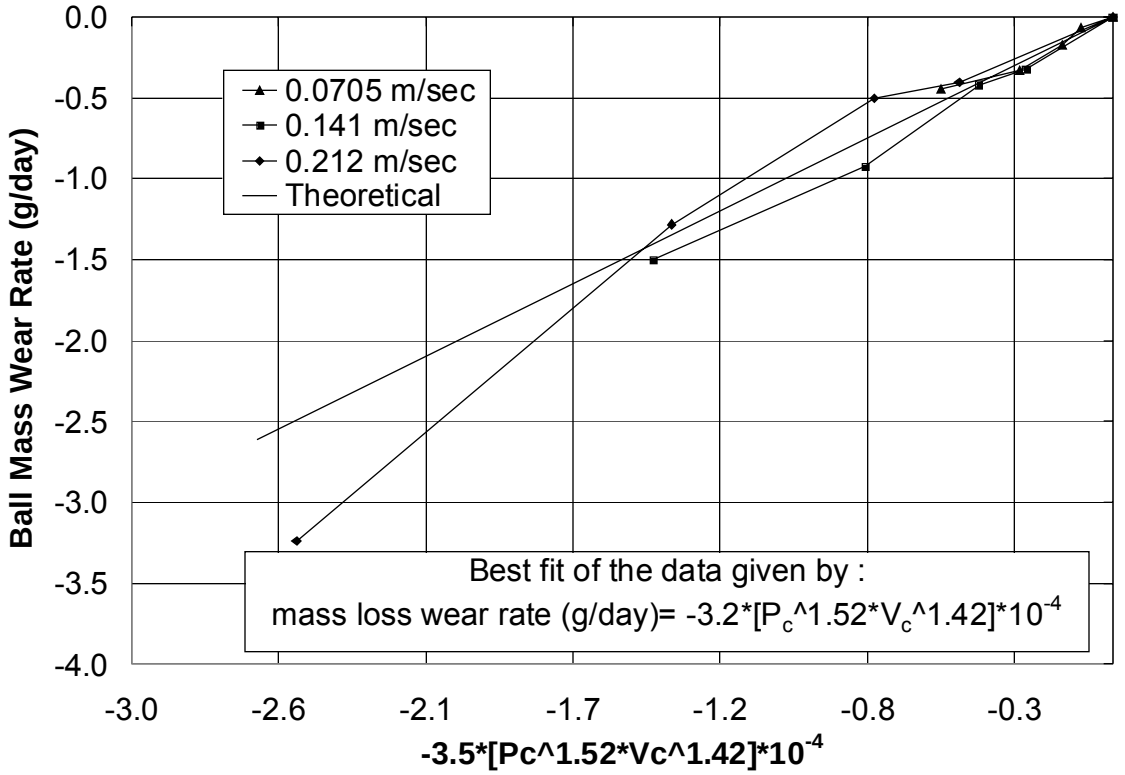

Figure 70: Cobalt 6 Ball Mass Wear Rate as a Function of Contact Pressure and Contact Velocity

An overall correlation for the wear pair was constructed using the mass wear rate of both the seat and ball samples. Both the stationary seat mass wear rate and rotating ball sample mass wear rate, found in Table 15, were added together to determine a mass wear rate for the material pair, WR_{MP}. Figure 71 shows the mass wear rate of the wear pair as a function of contact pressure. The mass wear rate of the material pair is a non-linear function of the contact pressure. A linear fit was applied to determine that mass wear rate of the material pair varies with $P_C^{1.58}$. The curve fitted linear relation between contact pressure and the mass wear rate of the material pair is shown in Figure 72.

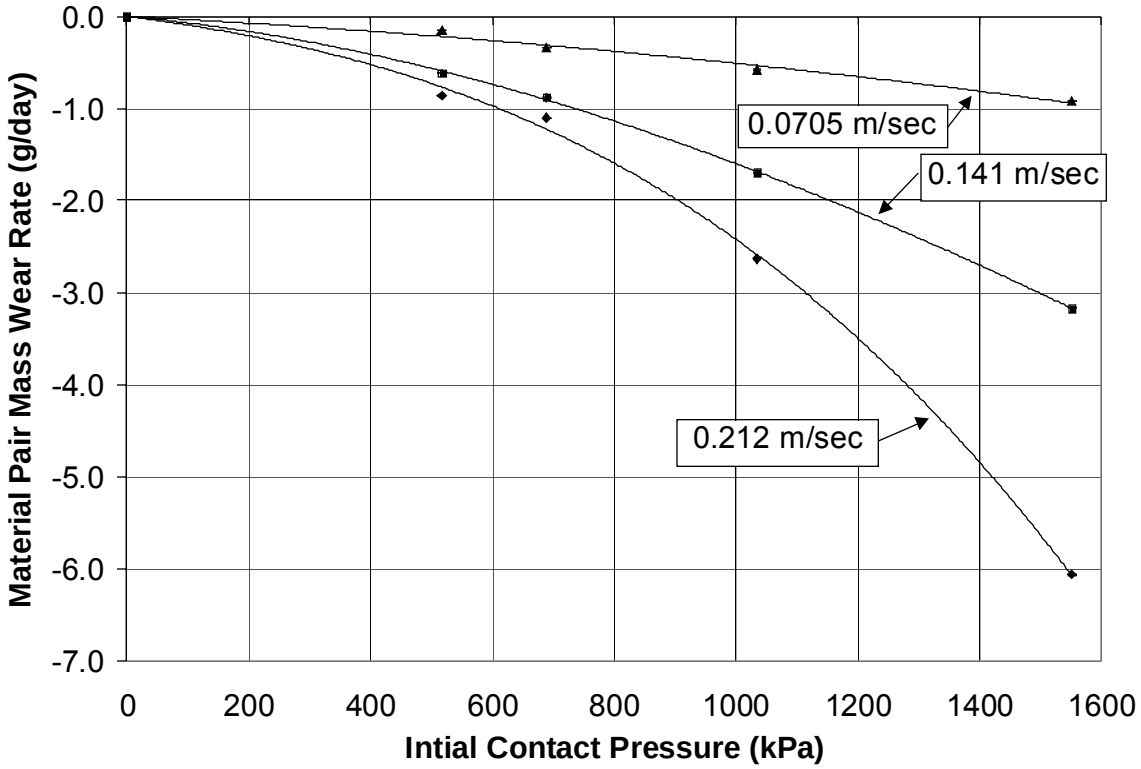

Figure 71: Effects of Contact Pressure on the Mass Wear Rate of the Cobalt 6 Material Pair

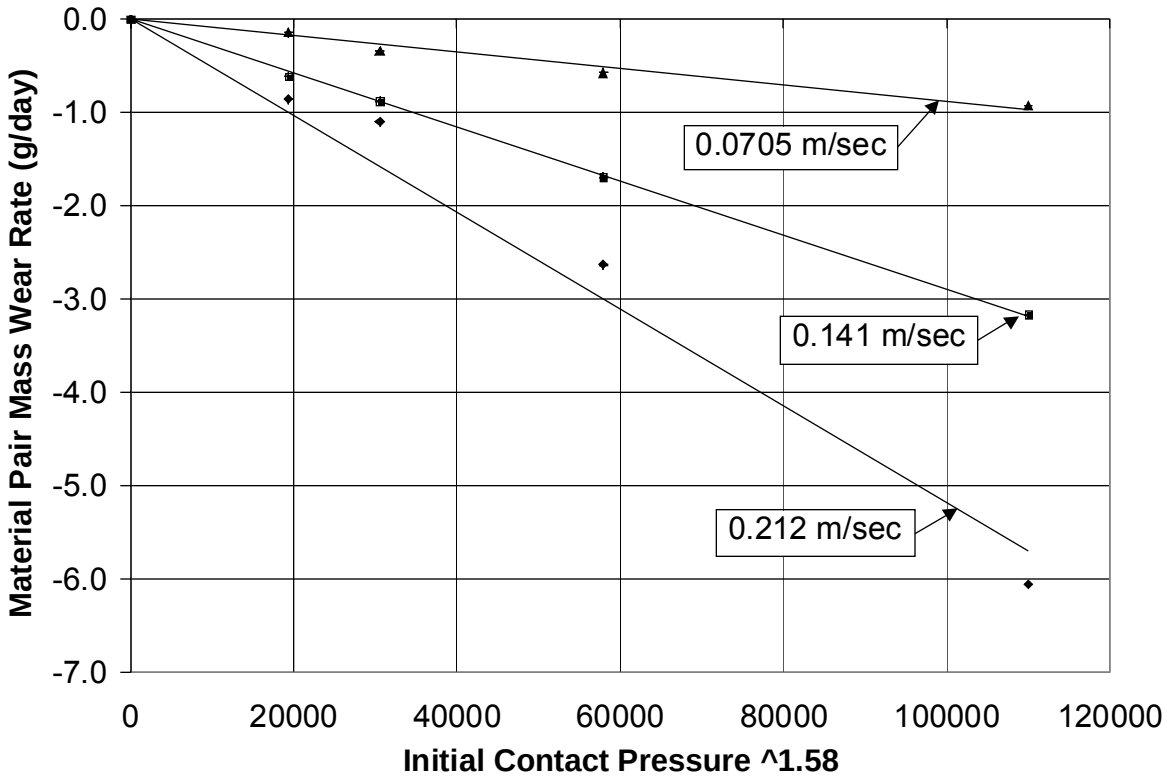

Figure 72: Mass Wear Rate of the Cobalt 6 Material Pair as a Function of Contact Pressure Raised to the Power of 1.58

The effects of contact velocity on the mass loss of the Cobalt 6 material pair over time is shown in Figure 73. These tests were performed at a constant contact pressure of 689 kPa and various contact velocities ranging from 0.0705 to 0.212-m/sec over three even time intervals. The mass loss of the material pair is linear over time with constant contact velocity, but non-linear over a range of contact velocities.

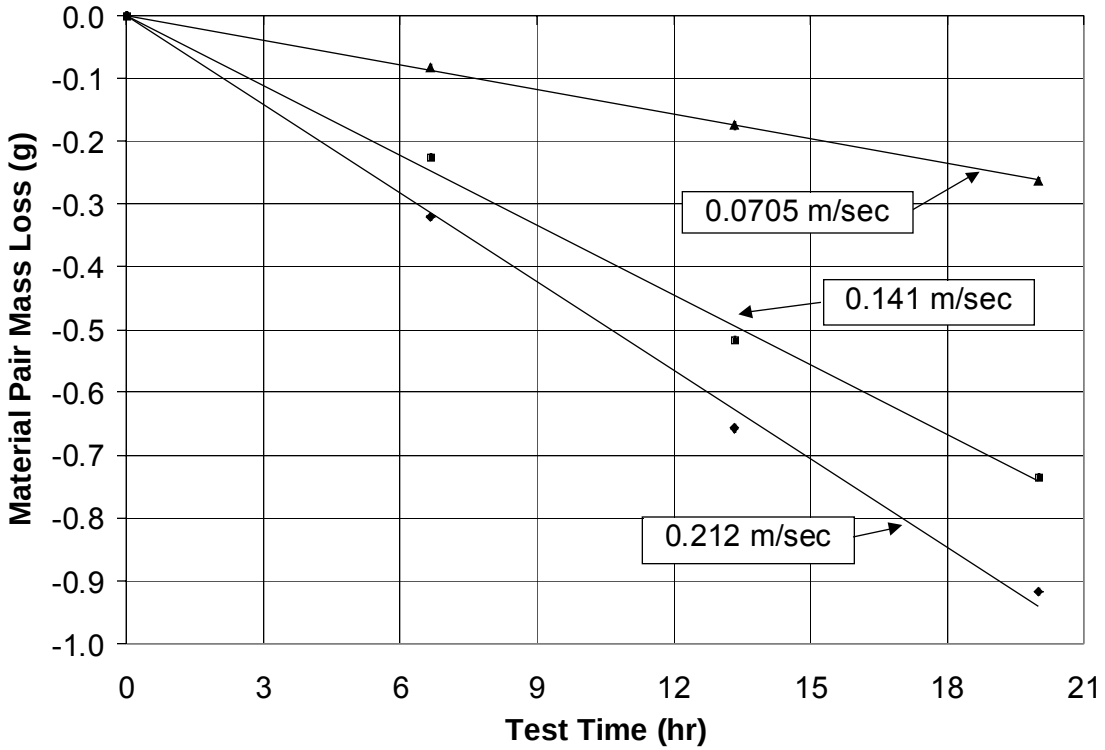

Figure 73: Effect of Contact Velocity Over Time on Mass Loss Rate of the Cobalt 6 Material Pair

With the collected data for the mass wear rate of the Cobalt 6 material pair, an overall correlation for the mass wear rate as a function of contact pressure and contact velocity was determined. The mass wear rate data was correlated to the form:

$$WR_{MP} = C_{MP} * P_C^{\alpha} * V_C^{\beta} \tag{26}$$

The values determined for these constants were $\alpha = 1.58$, $\beta = 1.51$ and $C_{MP} = -5.4*10^{-4}$. This relation is shown graphically in Figure 74. The final correlated equation for the mass wear rate of the material pair as a function of contact pressure and contact velocity was:

$$WR_{MP}\left[\frac{g}{day}\right] = -5.4*10^{-4} * \left[P_C\left[kPa\right]\right]^{1.58} * \left[V_C\left[\frac{m}{\sec}\right]\right]^{1.51} \tag{27}$$

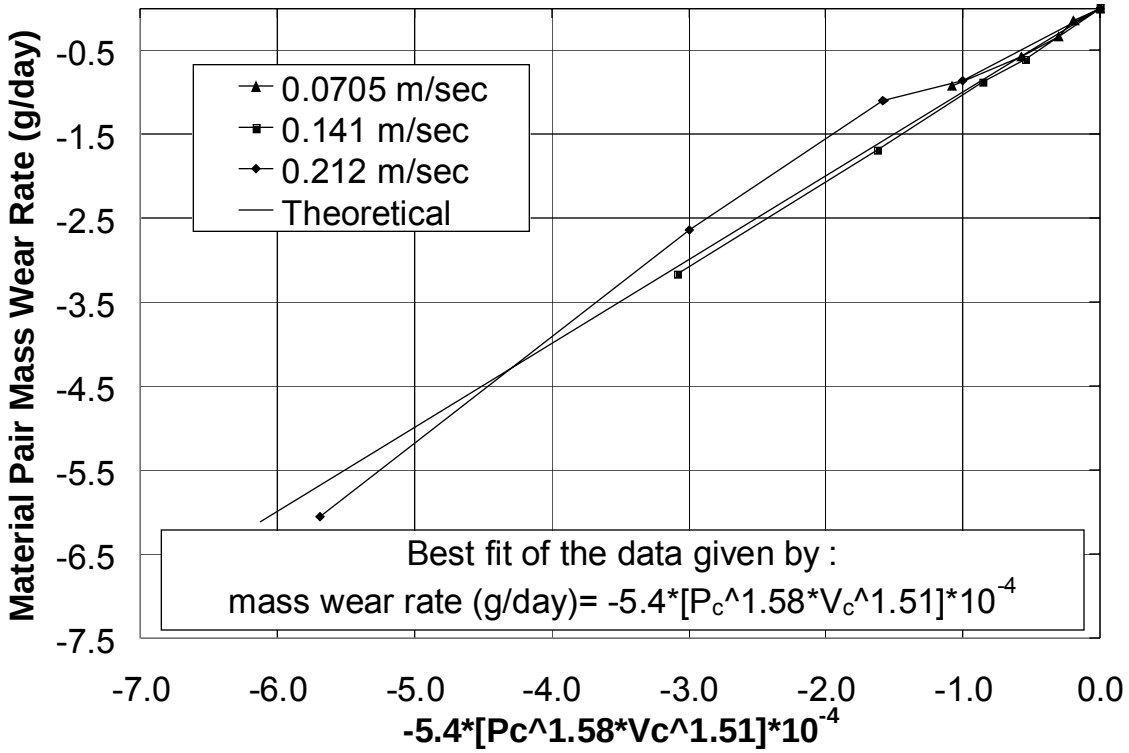

Figure 74: Cobalt 6 Material Pair Mass Wear Rate as a Function of Contact Pressure and Contact Velocity

For each test shown in Table 15, a sliding friction coefficient was calculated from the collected test data. The friction coefficients derived as a function of contact pressure at various velocities are shown in Figure 75 as test numbers C1 through C9, C12, C15 and C18. As may be seen in this Figure, the sliding friction coefficients followed no trend as a function of contact pressure. Figure 76 shows the collected sliding friction coefficients for tests C10 through C18 as a function of time over various contact velocities. The average friction coefficient for test number C1 through C18 was 0.324. Once again, there appears to be no trend in the friction coefficient as a function of time at various contact velocities. It appears that sliding friction coefficient follows no trend with contact pressure or contact velocity for Cobalt 6.

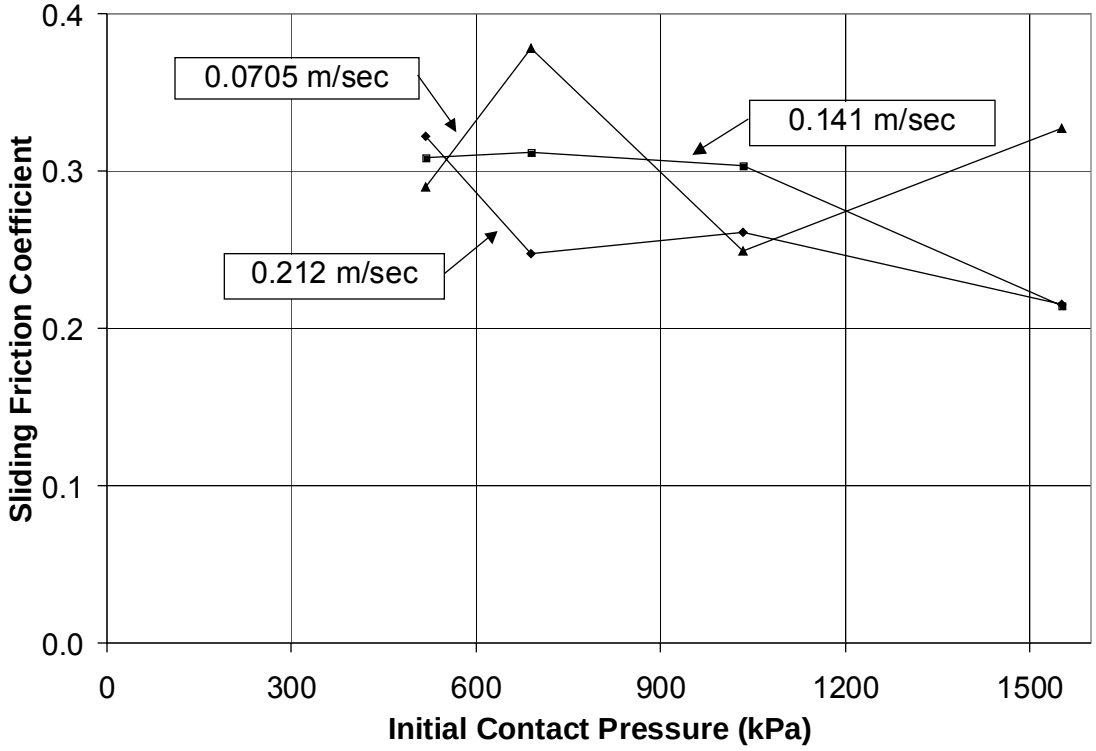

Figure 75: Sliding Friction Coefficient as a Function of Contact Pressure for Cobalt 6

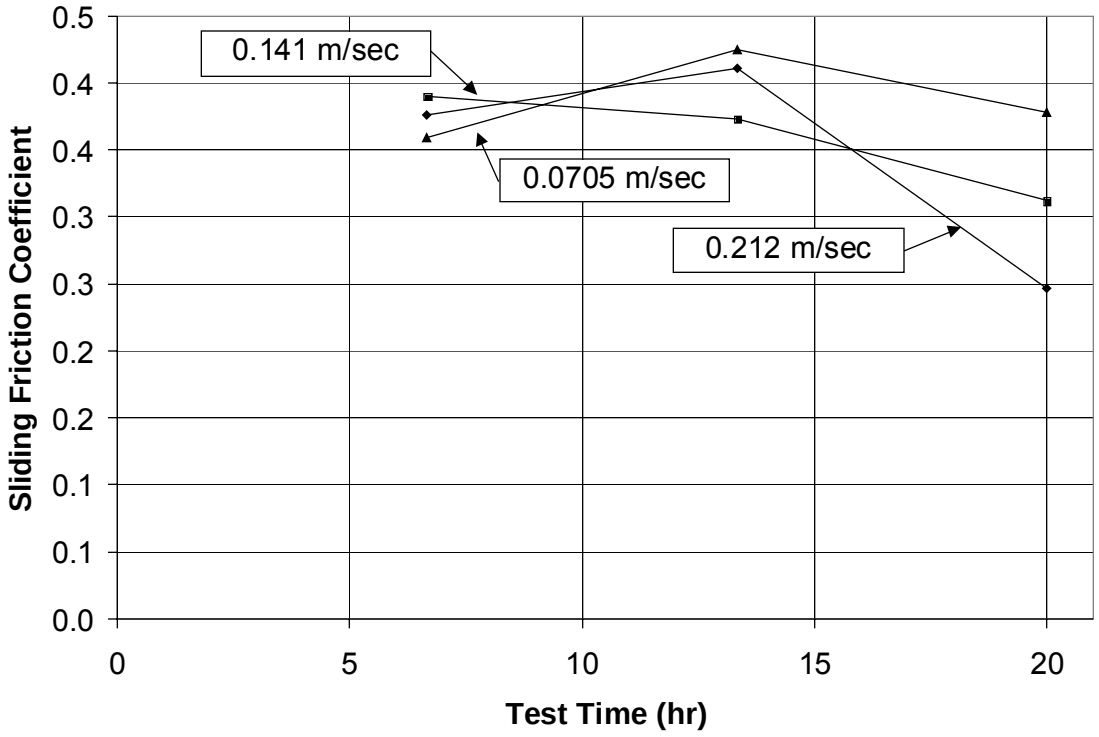

Figure 76: Sliding Friction Coefficient Over Time at Various Contact Velocities for Cobalt 6

Sub-task 4.1.4 Series I Prototype-scale wear testing

For this task, roll-dross build-up test and bearing wearing test are conducted on selected test alloys. Periodic measurement of the time-dependent development of the degraded layer of the pot hardware surface is also taken. Preliminary wearing test was conducted on CF3M tungsten carbide laser cladding against ACD Wearguard ceramic at 31 % production line tension and Stellite 6 against Tribaloy T-400 at 35 % production line tension. Wearguard™ bearing system was used for the wearing test. Modification have been made in the Wearguard™ system so as to fit into the Duraloy test bath. Wearing rate of the bearing sleeve was measured at the cleaned surface of the sleeve using a high precision diametric unit. The sleeve materials after the wear tests were examend by SEM, and Figure 77 shows the cross section view of the Stellite 6 alloy. The result can lead to the life estimate of the roll and bearing material in continuous hot dip galvanizing line. The surface hardness value was measured and correlated to the surface microstructure of the sleeve taken at the end of each cycle. The hardness value of the roll and bearing material for each testing condition were compared, as shown in Figure 78. Table 16 and Figure 79 show the measured wear rates, where the loads are scaled up to 50% of production line load for a uniform comparison.

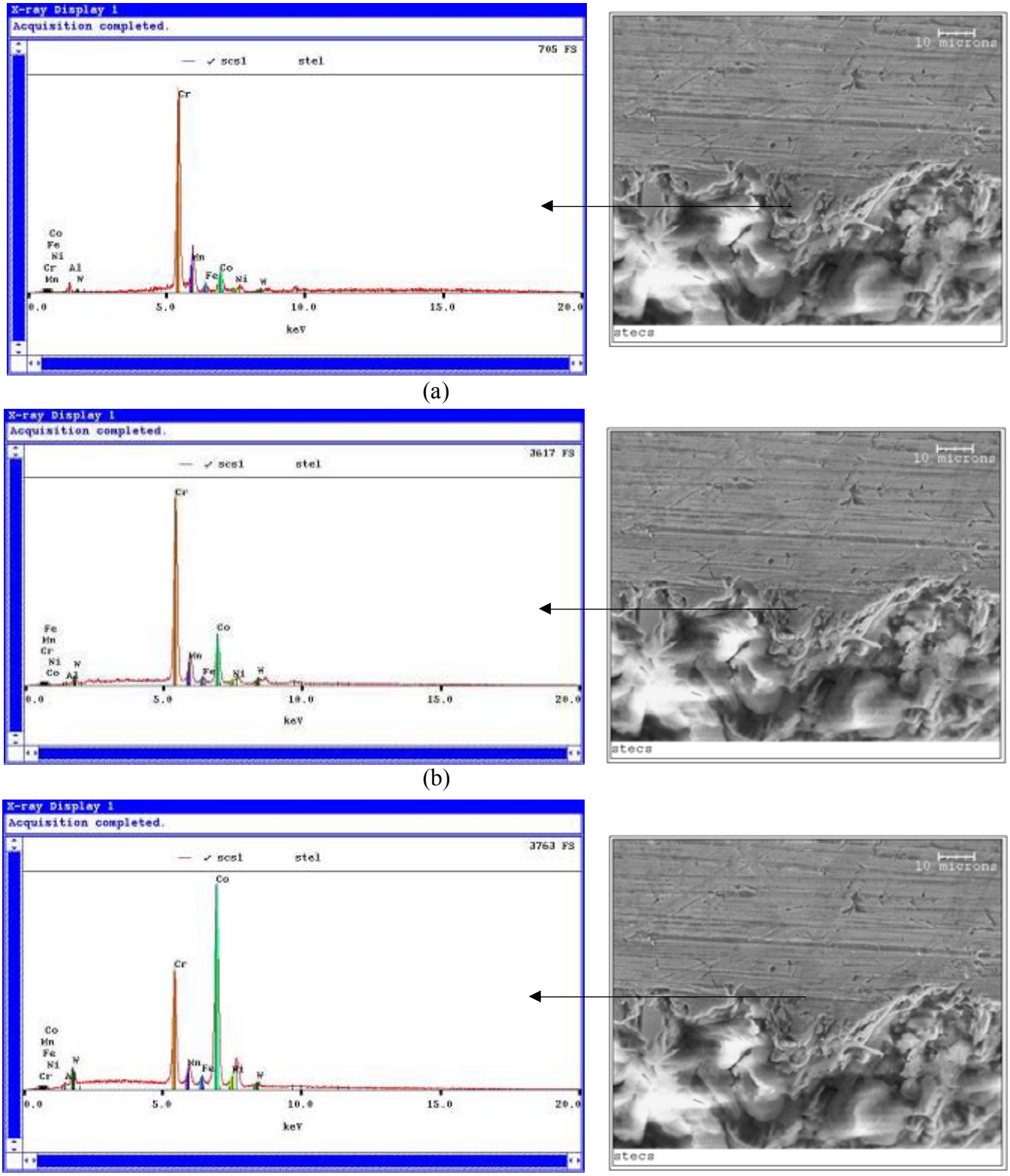

Figure 77: Cross sectional view showing diffusion of Co from matrix (diffusion layer) at (a) Near the diffusion layer to (c) far from the diffusion layer

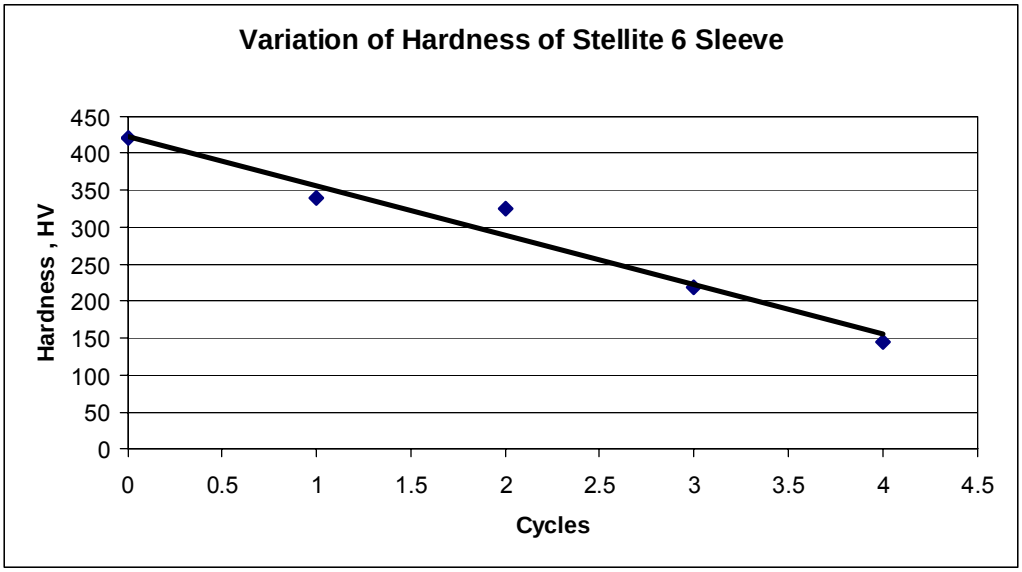

Figure 78: Variation of hardness values of stellite 6 sleeve

Test	Material Tested	% Of Production Line Load	Line Speed (ft/min)	Wearing Rate (mm/day)
WC Laser Clad /ACD Wearguard	WC Laser Clad	50 %	110 (21rpm)	0.03
Stellite 6 / T-400	Stellite 6	50 %	110 (21rpm)	0.05
Stellite 6 / Stellite 6	Stellite 6	50 %	110 (21rpm)	0.53

Table 16: Series I material wear rates

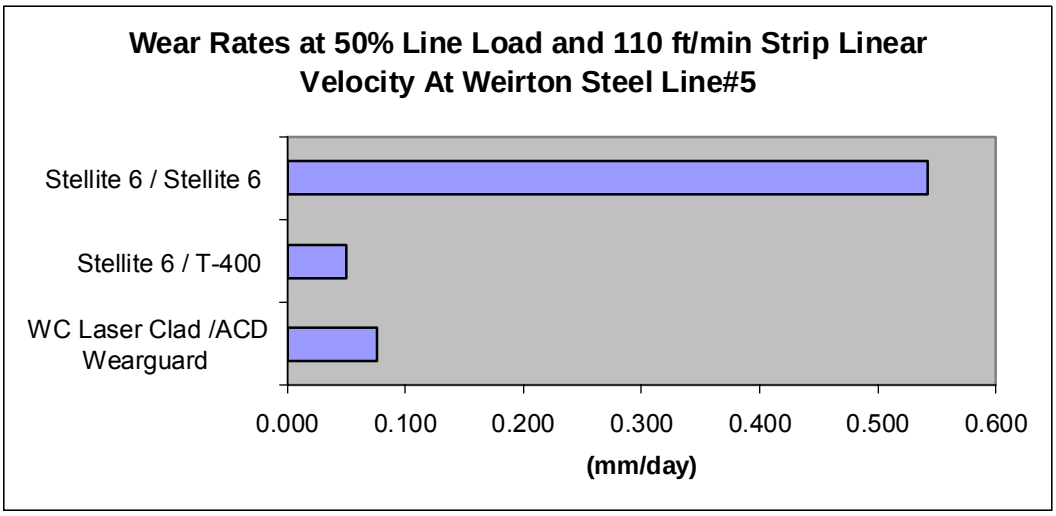

Figure 79: Wear Rates comparison of Series I materials.

Sub-Task 4.2 Series II Testing

The following table details the materials selected for testing under Series II.

Series II Materials	Use
ORNL Alloy 4	Roll material
ORNL Alloy 4-2	Roll material
ORNL Alloy 4-3	Roll material
ORNL Alloy 4-4	Roll material
CF-3M SS with WC Co (IR)	Roll material
2012	Bushing/sleeve material
2020	Bushing/sleeve material
2012xt	Bushing/sleeve material
Tribaloy T800	Bushing/sleeve material
AGC ceramic	Bushing material
Fontaine ceramic	Bushing material

Table 17: Series II material table

Sub-task 4.2.1 Series II Lab scale corrosion testing

Lab-scale corrosion testing continued on all of the Series II alloys (see Figure 80). The longest-term test reached 8000 h. Data from this figure is compared for Series II alloys after 500, 1000, 2000, 3000, 4000, and 6000 h (see Figures 81 through 86). These figures clearly show that the best metallic materials that can be used without pretreatment are 2012, 2020, and Tribaloy T-800.

Data for ORNL alloy 4-2Y (Y is yittrium) in Figure 87 shows that it performs well with 2-h pretreatment at 1100ºC. However, if surface repair is needed, a 2-h

treatment at 1200ºC is quite useful.

Figure 88 shows the static corrosion data for Tribaloy 400 and 800. Although Tribaloy 800 was tested for nearly 7000 h, Tribaloy 400 after 1500 h also showed exceptional performance. Based on ductility improvements of Tribaloy 400 over 800 (private discussion with James Wu, Deloro Stellite Group, Ltd.), Tribaloy 400 could be chosen over Tribaloy 800.

Figure 89 shows the long-term data on ACD ceramic. It is clear that it was not affected by molten zinc for up to 8000 h.

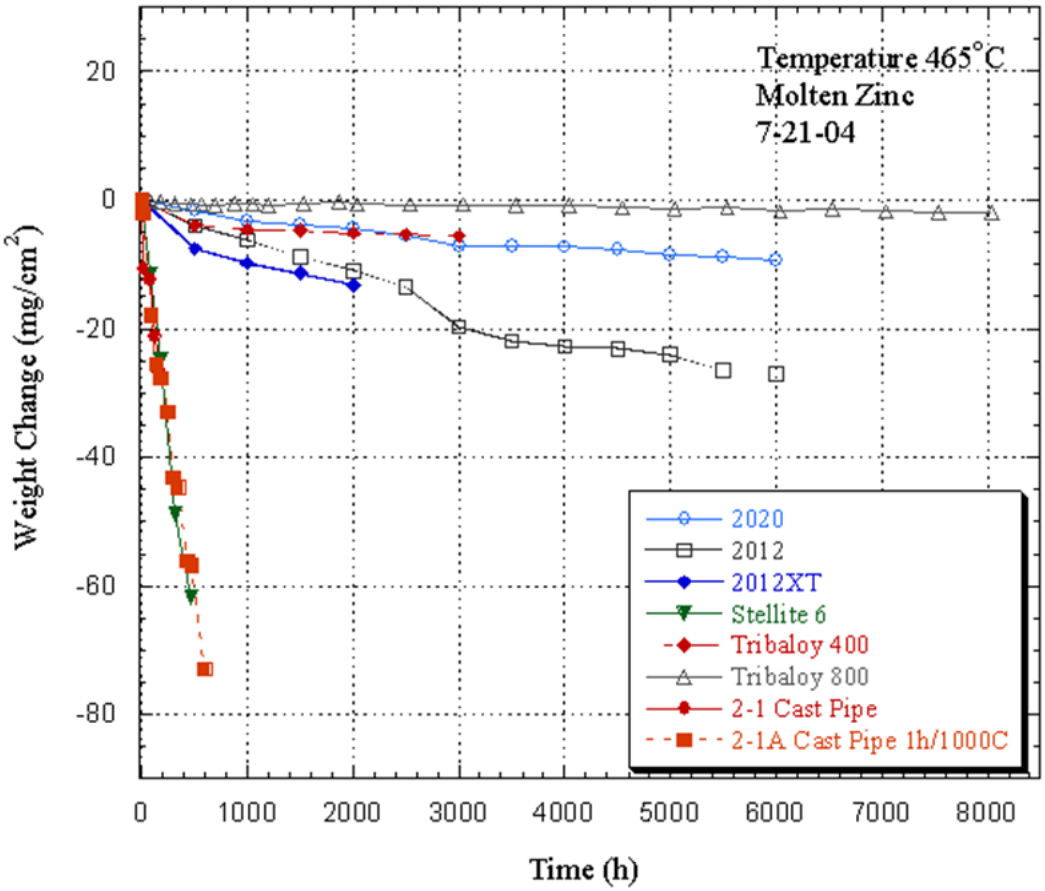

Figure 80: Static corrosion kinetics for Series II alloys.

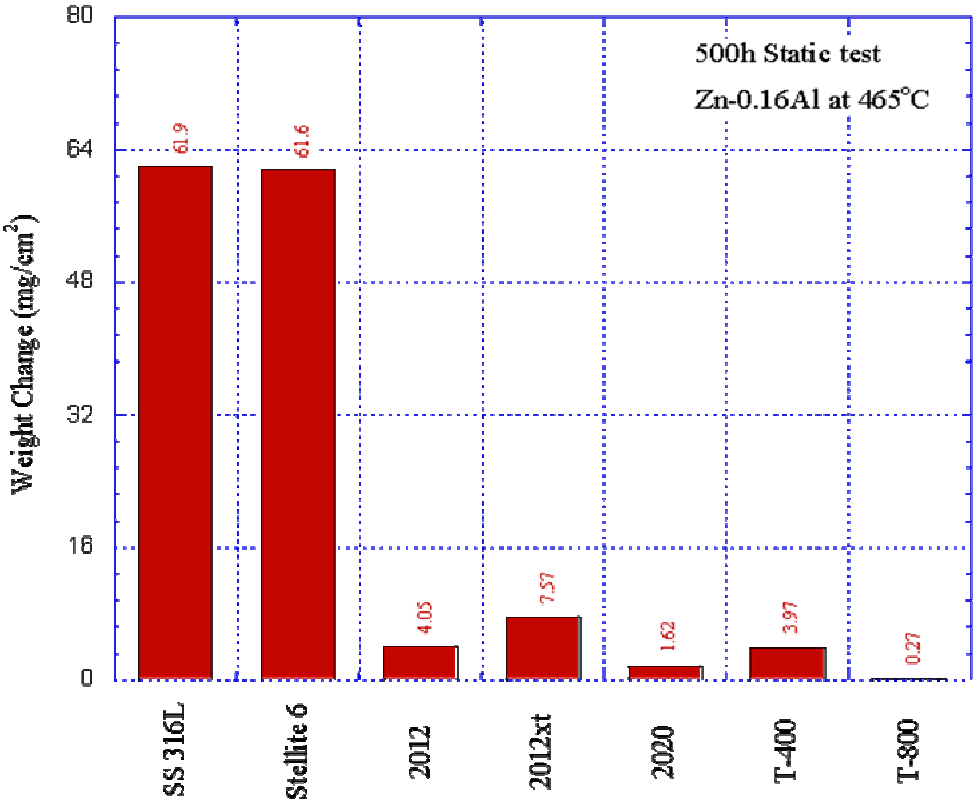

Figure 81: Static corrosion of Series II candidate alloys at 500 h.

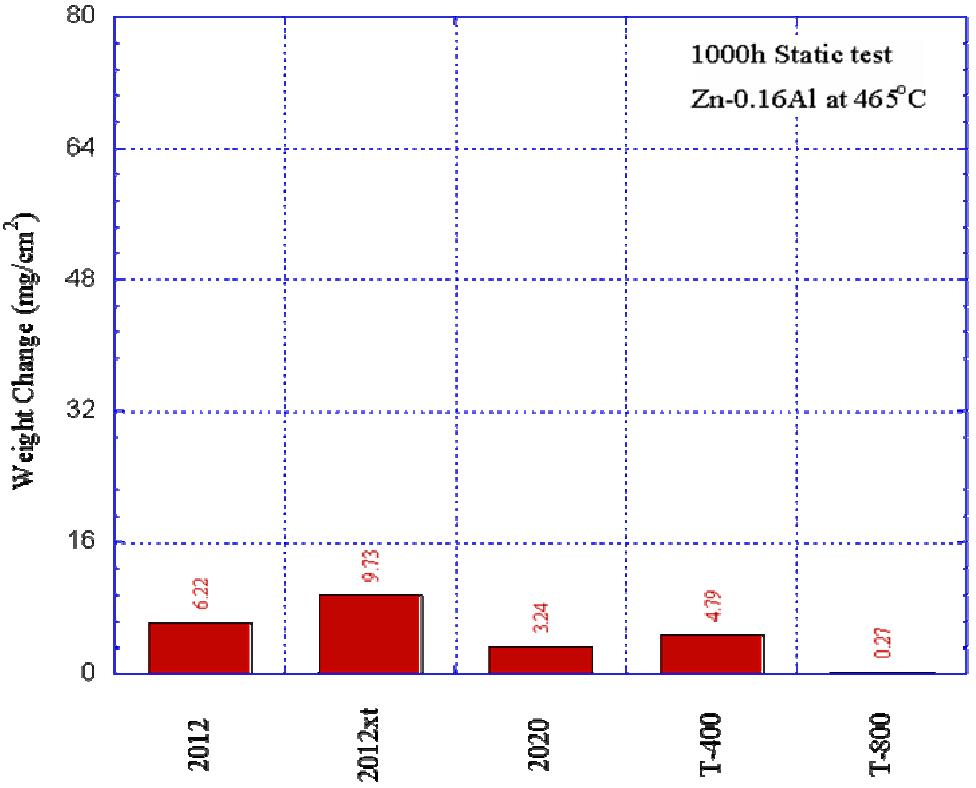

Figure 82: Static corrosion of Series II candidate alloys at 1000 h.

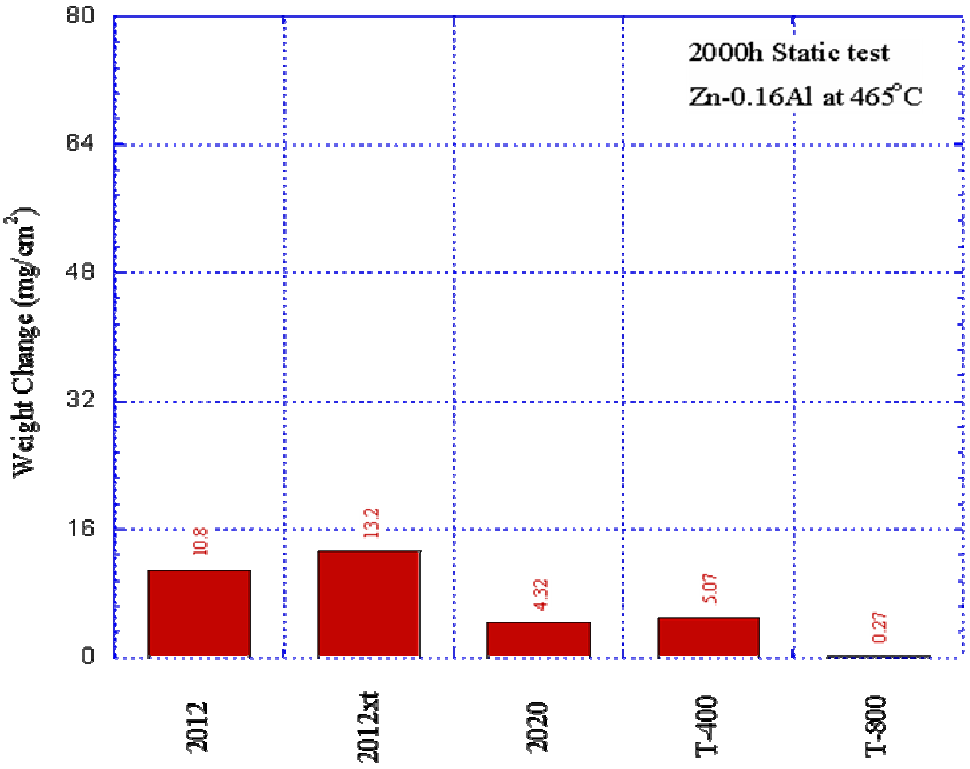

Figure 83: Static corrosion of Series II candidate alloys at 2000 h.

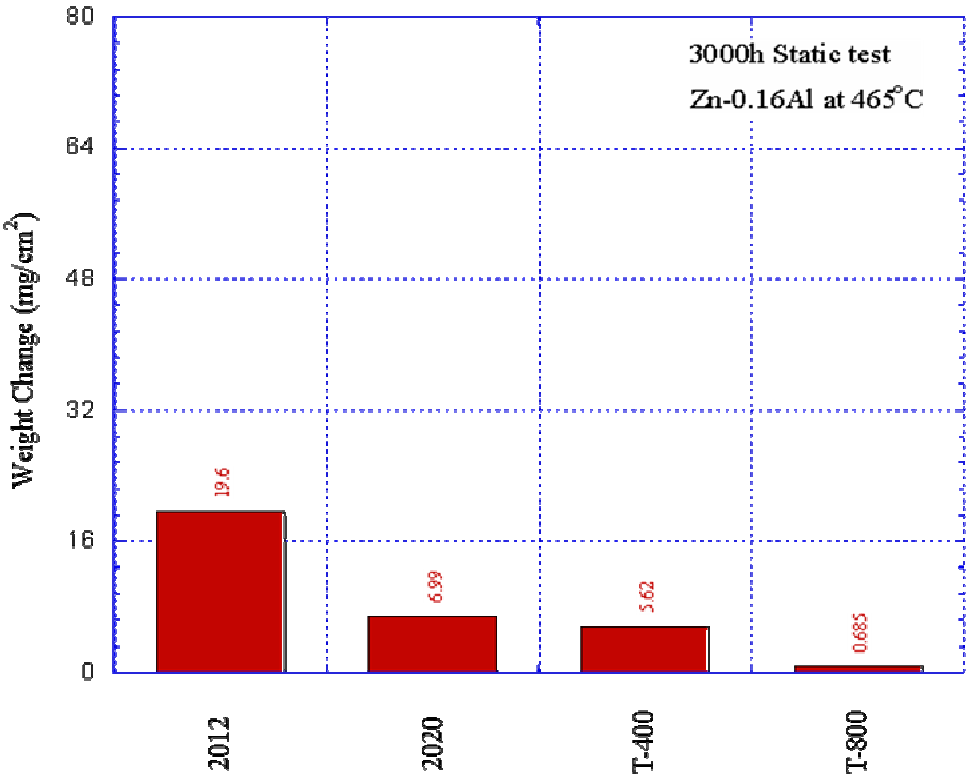

Figure 84: Static corrosion of Series II candidate alloys at 3000 h.

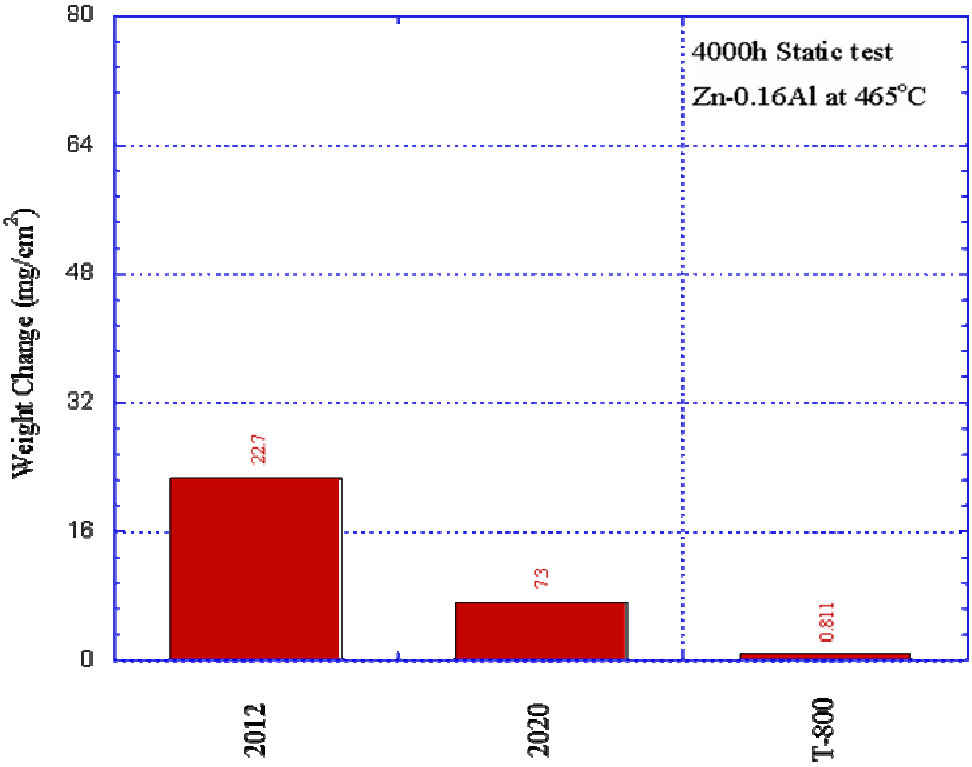

Figure 85: Static corrosion of Series II candidate alloys at 4000 h.

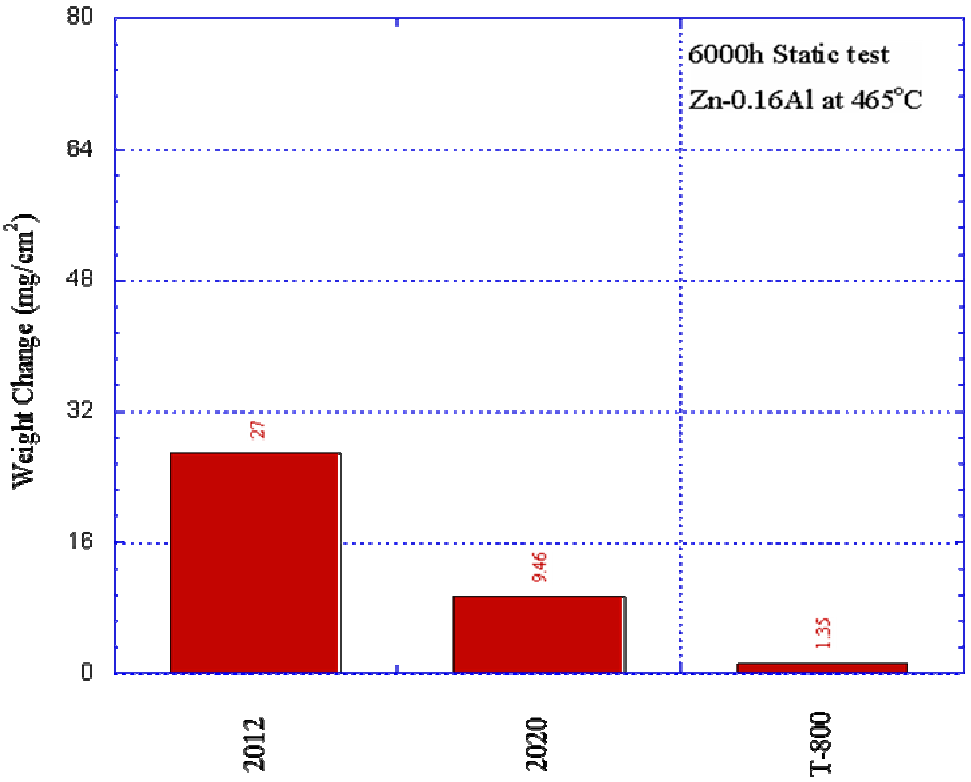

Figure 86: Static Corrosion of Series II candidate alloys at 6000 h.

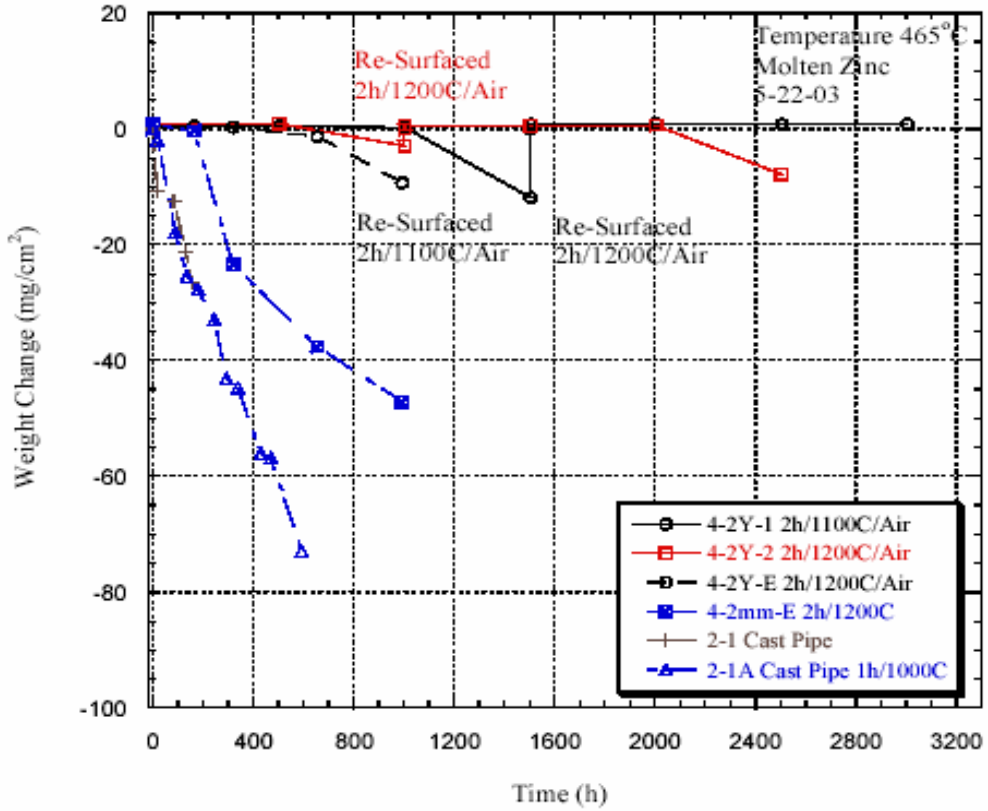

Figure 87: 4-2Y-1 and 4-2Y-2 weight change vs. time plot.

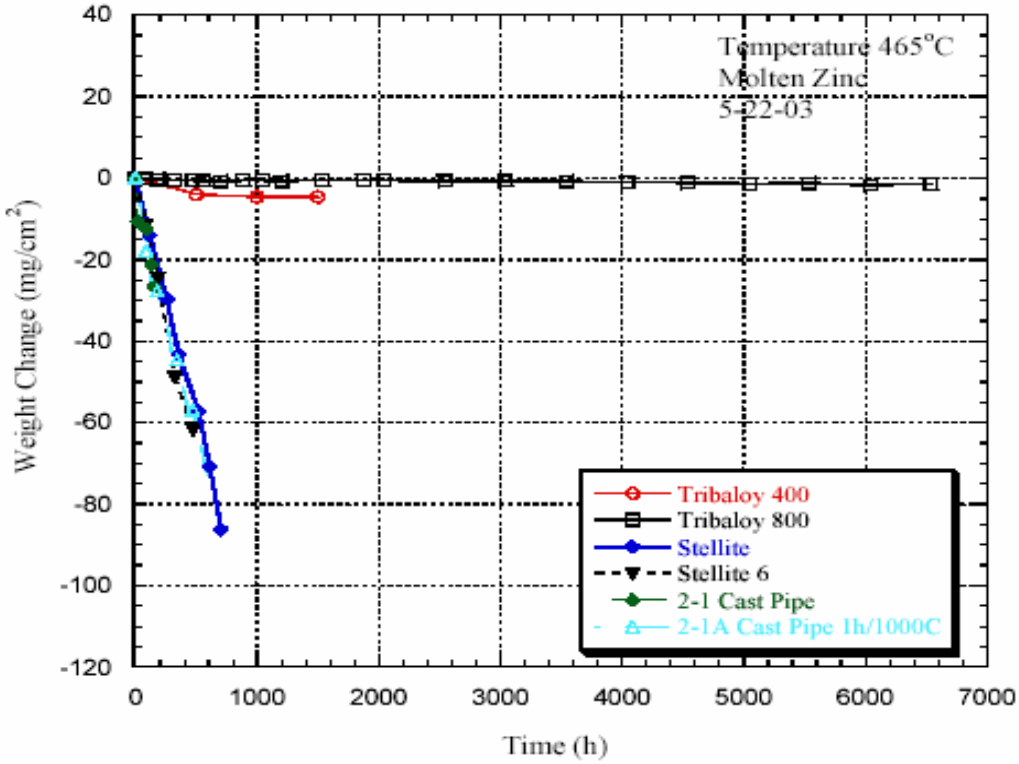

Figure 88: Tribaloy 400 and 800 and Stellite weight change vs. time plot.

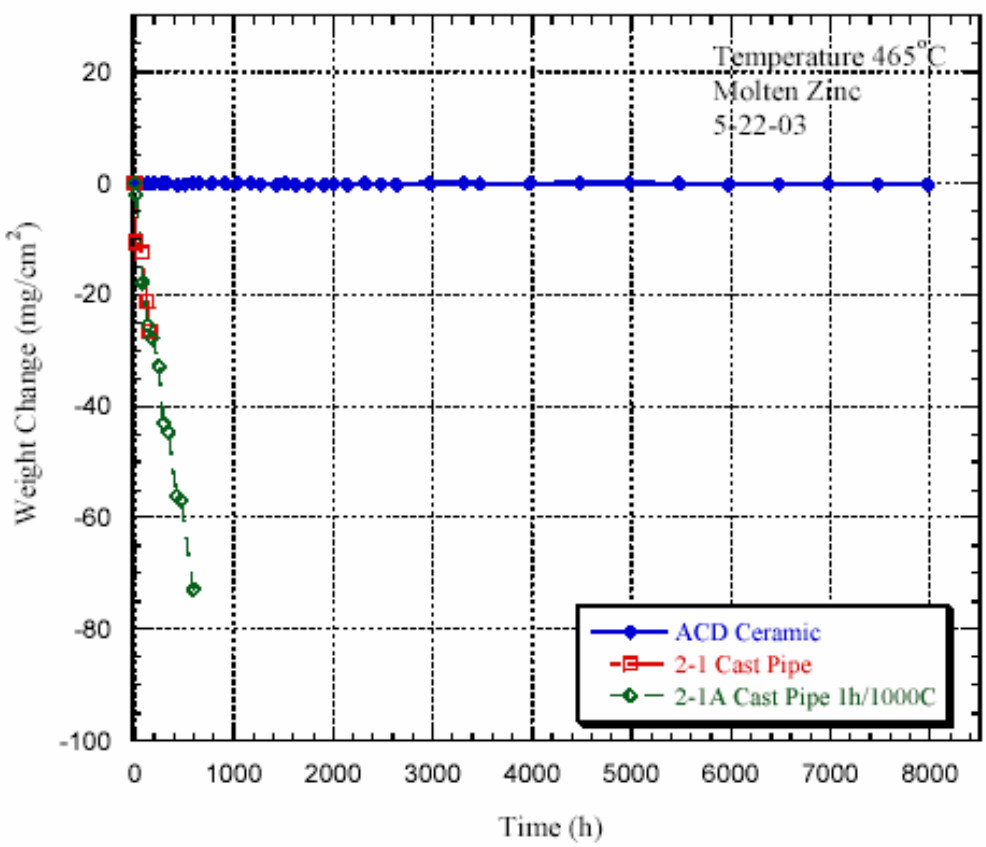

Figure 89: ACD Series weight change vs. time plot.

Sub-task 4.2.2 Series II In-plant corrosion testing

These materials were tested by static immersion at the above mentioned hot-dipping lines. The samples are long thin strips of either the substrate material, Oak Ridge Alloy 4, or a spray coated with the tungsten carbide coating. Results from these tests are as follows:

Corrosion in GI/GA Bath The corrosion rates of the alloys were calculated based on the data at 1 inch from the bottom of the specimens. Figure 90 illustrates the corrosion rates of the base alloys and coating in GI/GA bath, as compared with two baseline materials: CF3M and Stellite 6. There is no measurable thickness change for 2012 specimens immersed up to 4 weeks in different baths.

Corrosion in GL Bath The corrosion rates of the alloys in Galvalume bath are shown in Figure 91. Although 2012 behave very well in GI/GA bath, the corrosion rates of 2012 is the fastest among the four alloys listed in the figure, which is around 1.5×10^{-2} in/week. After 12 weeks immersion in GL bath, the lower 3 inches of 2012 has disappeared. The corrosion rate of ORNL 4 is about 1.4 times of CF-3M.

Microstructural Analysis: Analysis of the tested samples were carried out by SEM/EDAX. Figure 92 shows that there is a continuous dross buildup layer attached to the ORNL 4 alloy, after the alloy was dipped in steel partner B's GI bath for two weeks. It is still not clear that If this layer is the corrosion product of the alloy, or it is the result of the dross particles sticking onto the sample surface. Figure 93 shows the SEM/EDAX

micrograph of the same alloy after dipping in GL bath for two weeks. It is apparent that there are two intermetallic layers in between the frozen bath and the alloy substrate, although both layers have similar chemical compositions. There are some cracks close to the interface between the two layers, which were believed to form during the cooling. The cracks confirm that there is mismatch of thermal expansion between the two layers.

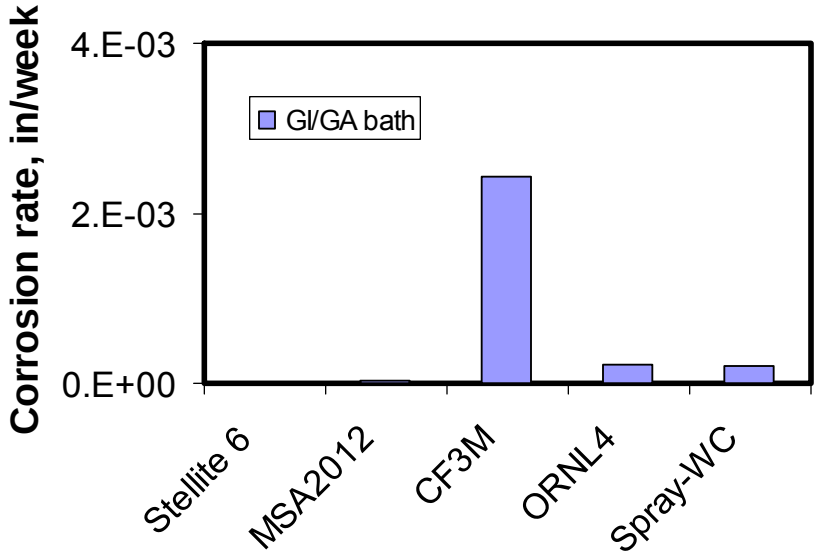

Figure 90: Corrosion rates of the alloys in GI/GA baths

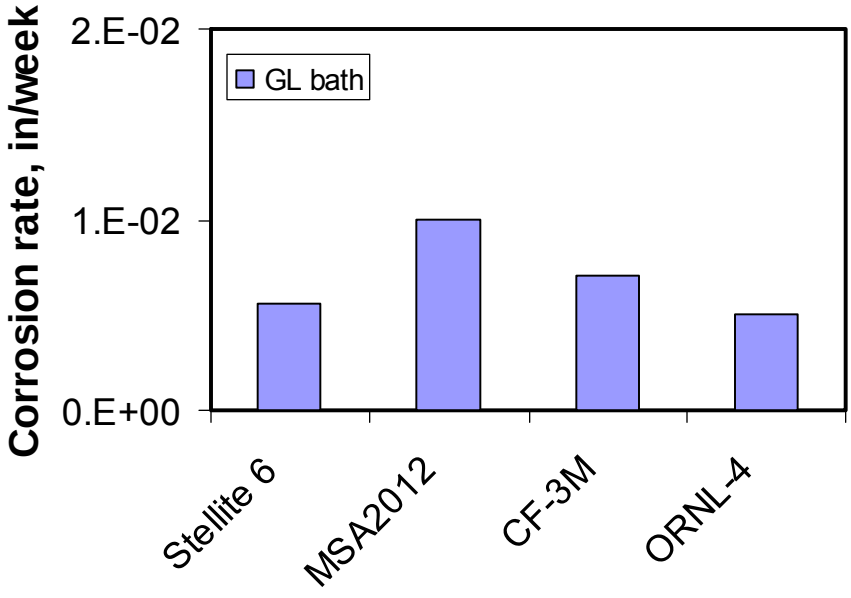

Figure 91: Corrosion rates of the alloys in GL baths

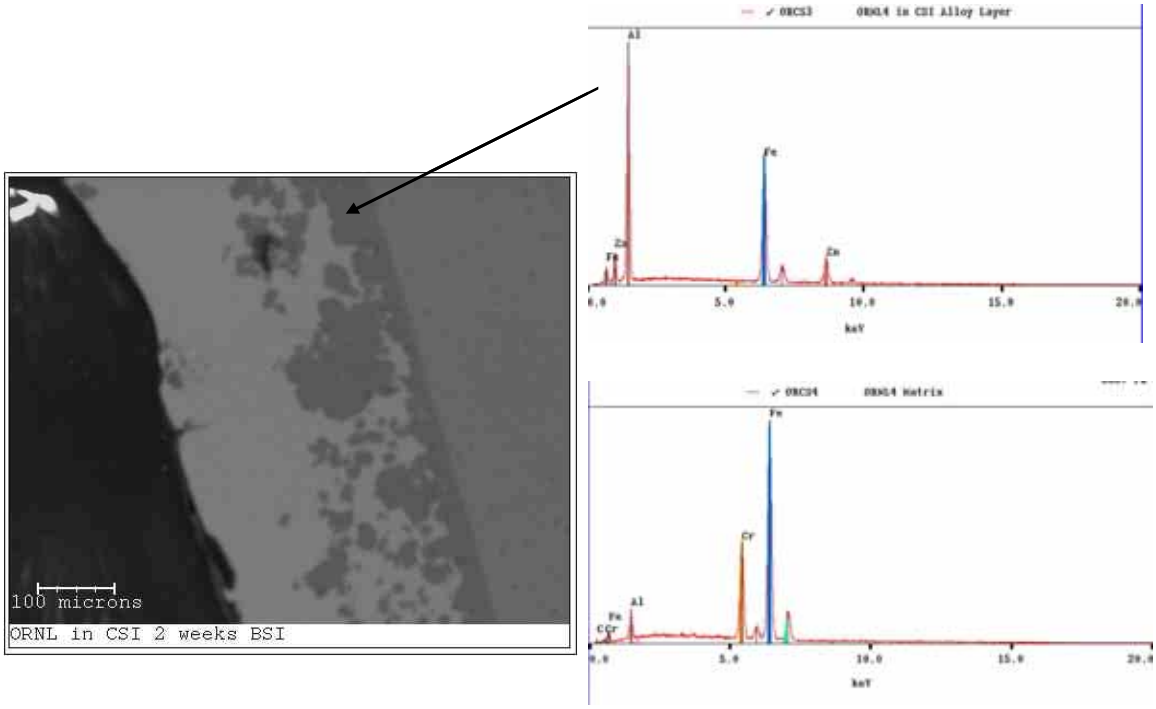

Figure 92: SEM/EDAX micrographs of ORNL-4 alloy after dipped in GI bath for 2 weeks.

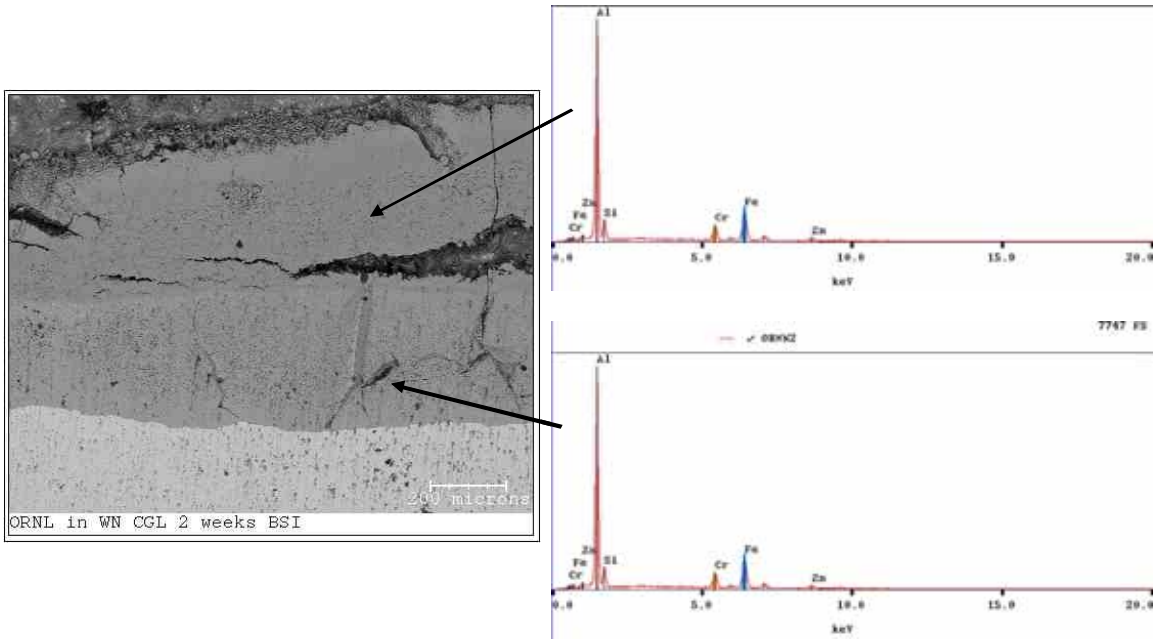

Figure 93: SEM/EDAX micrographs of ORNL-4 alloy after dipped in GL bath for 2 weeks.

Sub-task 4.2.3 Series II Lab-scale wear testing

Following the testing procedures of Sub-task 4.1.3, a series of tests were conducted on various new material combinations that were provided by both ORNL and

industrial partners.

Rotating Ball Specimen Material	Stationary Seat Specimen Material	Wear Rate of Stationary Seat (mm/day)	Sliding Friction Coefficient of Material Pair
2020	2020	0.616	0.31
2020	AGC Ceramic	0.0890	0.40
AGC Ceramic	2020	0.939	0.55
2012	2012	0.823	0.38
2012 XT	2012 XT	0.660	0.51
Tribaloy 800	Fontaine Ceramic	0.0939	0.43
Tribaloy 800	Tribaloy 800	0.236	0.47

Table 18: Series II bushing and sleeve materials for wear testing

Pressure and Velocity correlation studies with 2012 XT

Supplier A Molten Metal Systems of Ohio produces a proprietary iron-based superalloy labeled as 2012 XT. Table 19 shows the composition of the 2012 XT alloy, which must remain confidential due to the proprietary nature of this alloy. This material performed well in preliminary screening wear tests and was selected for further study based on its good performance.

Alloying Element	Mo	W	Cr	Co	V	Nb	C	Mn	Si	Fe
Mass Percent in Alloy	Iron-based superalloy containing primary additives of Mo, W and Cr									

Table 19: Composition of 2012 XT

Tests were performed to determine the effects of contact pressure and contact velocity on the wear rate of 2012 XT running against itself, while submerged in a molten zinc bath of typical galvanizing composition at 460°C. The galvanizing zinc used in the study contained approximately 0.17wt% aluminum. Prior to testing, all 2012 XT samples provided by Supplier A were pre-polished and prepared for testing. The tests sample seat widths were measured before and after testing using an optical microscope to the nearest 0.025-mm and the ball samples were weighed to the nearest 0.001-g using a digital balance. The contact pressures, contact velocities and wear rate data obtained from these tests are shown in Table 20.

Test Number	Contact Pressure, P_C (kPa)	Contact Velocity, V_C (m/sec)	Test Duration (hours)	Seat Wear Rate, WR_S (mm/day)	Ball Mass wear rate, WR_B (g/day)	Seat Mass wear rate, WR_{SM} (g/day)
M1	517	0.0705	20	0.059	-0.086	-0.079
M2	1034	0.0705	20	0.180	-0.110	-0.115
M3	1551	0.0705	20	0.318	-0.491	-0.461
M4	517	0.141	20	0.145	-0.184	-0.196
M5	1034	0.141	20	0.414	-0.614	-0.597
M6	1551	0.141	20	0.619	-1.026	-0.983
M7	517	0.212	20	0.289	-0.428	-0.398
M8	1034	0.212	20	0.463	-0.687	-0.700
M9	1551	0.212	20	0.989	-1.810	-1.868
M10	689	0.0705	6.6	0.101	-0.133	-0.128
M11	689	0.0705	13.3	0.073	-0.090	-0.096
M12	689	0.0705	20	0.083	-0.097	-0.108
M13	689	0.141	6.6	0.270	-0.414	-0.365
M14	689	0.141	13.3	0.303	-0.452	-0.417
M15	689	0.141	20	0.262	-0.406	-0.379
M16	689	0.212	6.6	0.372	-0.497	-0.505
M17	689	0.212	13.3	0.354	-0.554	-0.502
M18	689	0.212	20	0.377	-0.504	-0.562

Table 20: Collected Data from 2012 XT Wear Rate Correlation Tests

The effect of contact pressure, P_C, on the stationary seat wear rate, WR_S, of 2012 XT is shown in Figure 94. These tests were performed with contact pressures ranging from 517 to 1551 kPa and contact velocities ranging from 0.0705 to 0.212 m/sec. These 20 hour tests shown are labeled as tests M1 through M9, M12, M15 and M18 in Table 20. As shown in Figure 94, the seat wear rate is non-linear with contact pressure. These test data fall on a straight line when the wear rate, WR_S, is plotted as a function of $P_C^{1.31}$. This linearized relationship is shown in Figure 95.

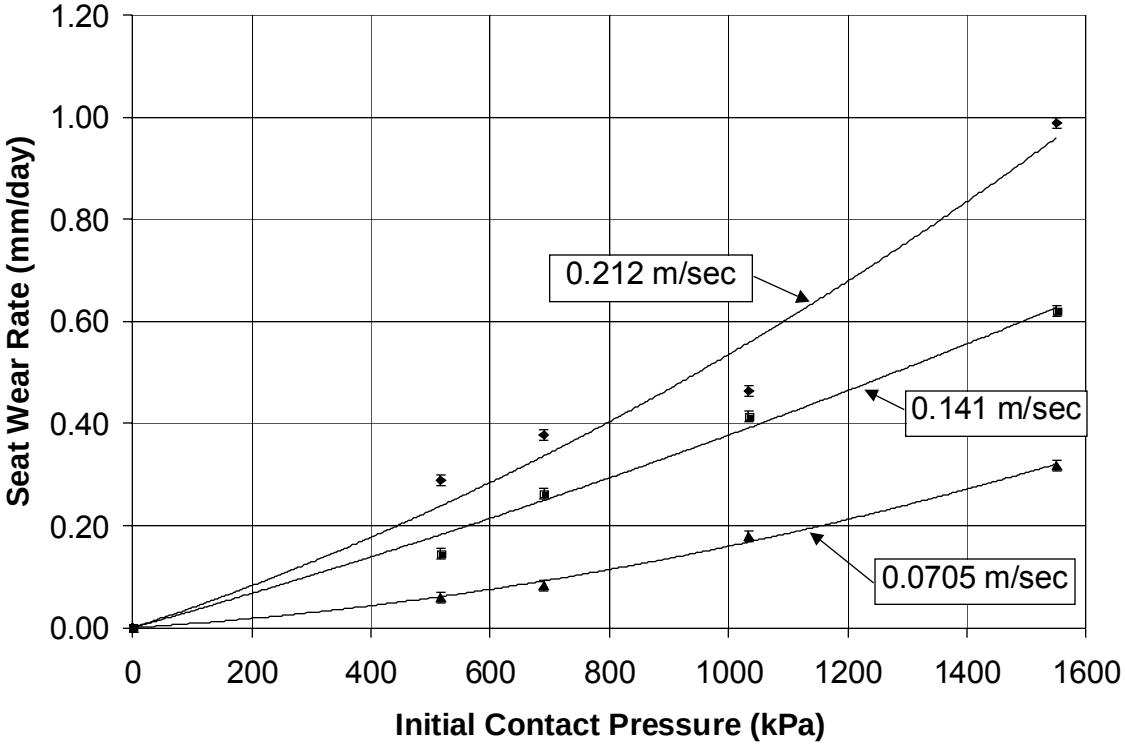

Figure 94: Contact Pressure Effects on Seat Wear Rate of 2012 XT

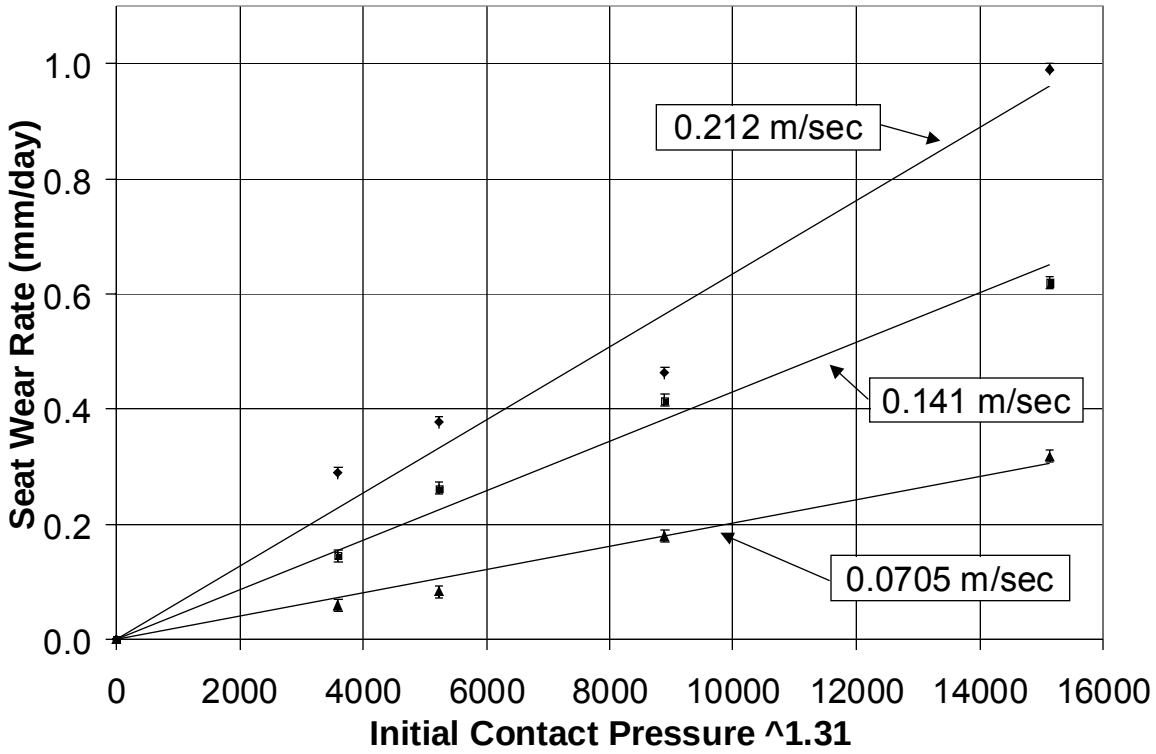

Figure 95: Seat Wear Rate of 2012 XT as a Function of Contact Pressure Raised to the Power of 1.31

The effect of contact velocity, V_C, on seat wear depth, was studied using 2012 XT. Tests were performed in three equal time intervals adding up to 20 hours of testing at a constant contact velocity. The tests were repeated three times at velocities of 0.0705, 0.141 and 0.212-m/sec corresponding to 75, 150 and 225 spindle RPM. The constant contact pressure was held constant at 689-kPa. The test results are labeled as tests M10 through M18 in Table 20. Figure 96 shows the effect of contact velocity on seat wear depth over time. As seen in this Figure, the seat wear depth is linear with time at a constant contact velocity, but non-linear with time over a range of contact velocities. For this test the wear rate as a function of velocity showed to be $V_C^{1.16}$. If wear rate were proportional to $V_C^{1.0}$ then one could conclude that wear is simply proportional to the distance traveled instead of being a complex function of velocity.

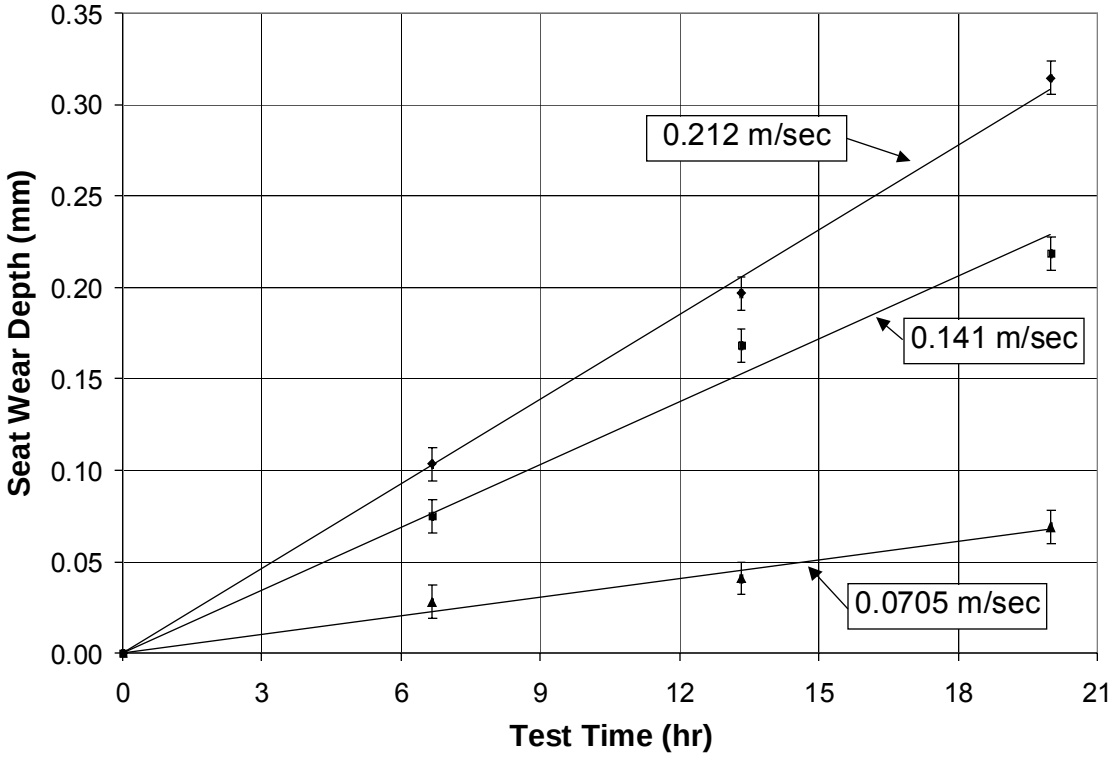

Figure 96: Effects of Contact Velocity on Seat Wear Depth Over Time with 2012 XT

Using the collected data, a correlation between the contact pressure, contact velocity and seat wear rate was constructed. This curve-fitted correlation for seat wear was in the form:

$$WR_S = C_S * P_C^{\alpha} * V_C^{\beta} \tag{28}$$

where α is the contact pressure correlation exponent, β the contact velocity correlation exponent for the stationary seat specimen seat wear rate. The proportionality constant, C_S, depends on units used. The values determined for the three parameters were: α = 1.31, β = 1.16 and $C_S = 3.9*10^{-4}$. This resulted in a final correlation for the 2012 XT seat wear rate given by:

$$WR_S\left[\frac{mm}{day}\right] = 3.9*10^{-4} * \left[P_C\left[kPa\right]\right]^{1.31} * \left[V_C\left[\frac{m}{\sec}\right]\right]^{1.16} \tag{29}$$

This correlation is shown graphically in Figure 97.

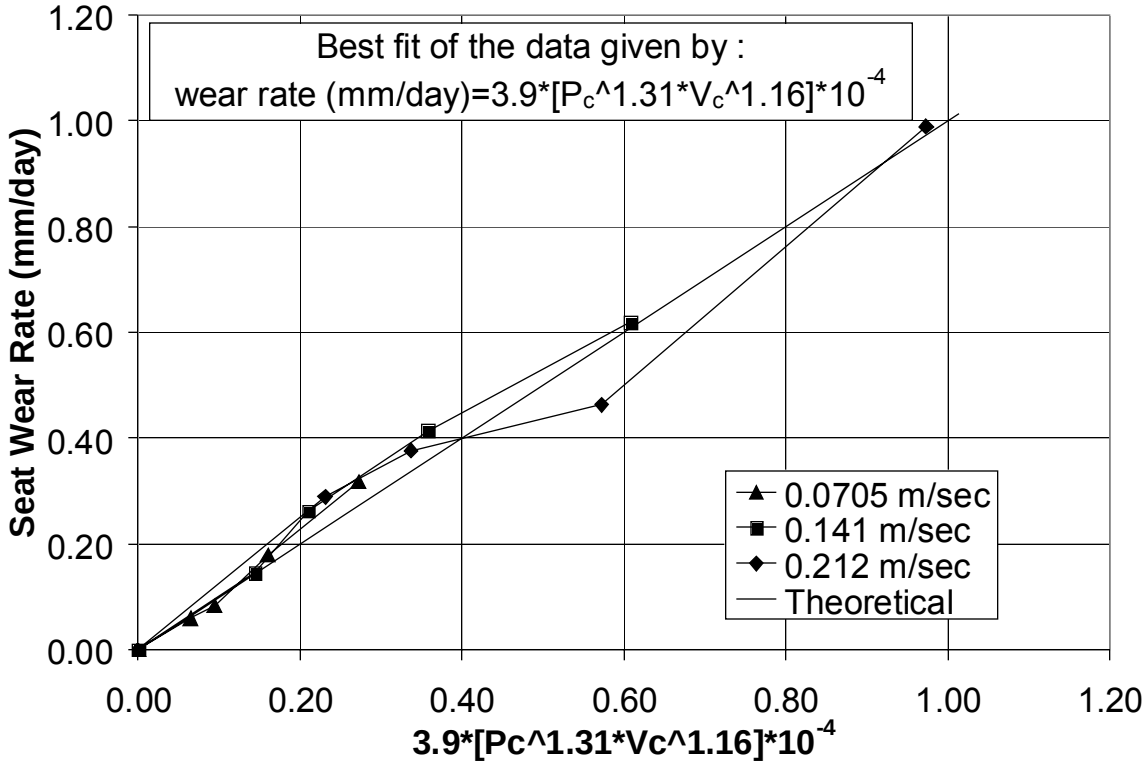

Figure 97: 2012 XT Seat Wear Rate as a Function of Contact Pressure and Contact Velocity

The seat mass wear rate, WR_{SM}, is also a function of contact pressure and contact velocity. The volume of the material lost on the stationary seat due to wear, V_{wear}, was calculated using

$$V_H = \frac{\pi * D_H^2}{4} * \left(H_{ball\,mill} - H_o \right) \tag{30}$$

Using the density of 2012 XT as provided by Supplier A of 0.008229-g/mm^3, the mass wear rate of the stationary seat was determined for each test according to equation 3.18. The calculated mass wear rate of the stationary seat specimen is shown in Table 20. This calculated mass wear rate relies only on the volume of material lost from the wear surface of the stationary seat specimen and does not include any mass lost or gained from the stationary seat specimen due to liquid metal corrosion by the galvanizing zinc.

The effect of contact pressure on mass wear rate of the stationary seat made of 2012 XT is shown in Figure 98. These tests were performed with contact pressures ranging from 517 to 1551 kPa and contact velocities ranging from 0.0705 to 0.212 m/sec. All tests lasted 20 hours and are labeled as tests M1 through M9, M12, M15 and M18 in Table 20. From this Figure, it shows that the mass wear rate of the seat is again a non-linear function of contact pressure. The best curve fit was to linearize wear rate is obtained with WR_{SM} proportional to $P_C^{1.57}$, as in Figure 99.

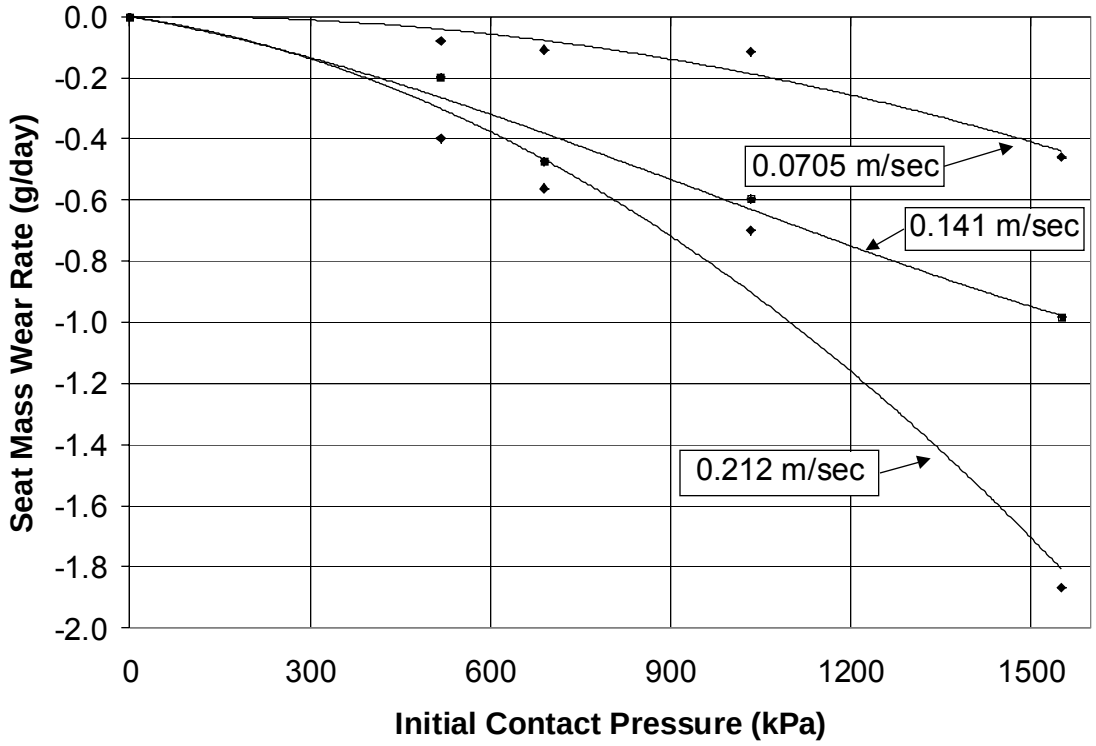

Figure 98: Mass Wear Rate of the 2012 XT Seat Sample as a Function of Contact Pressure

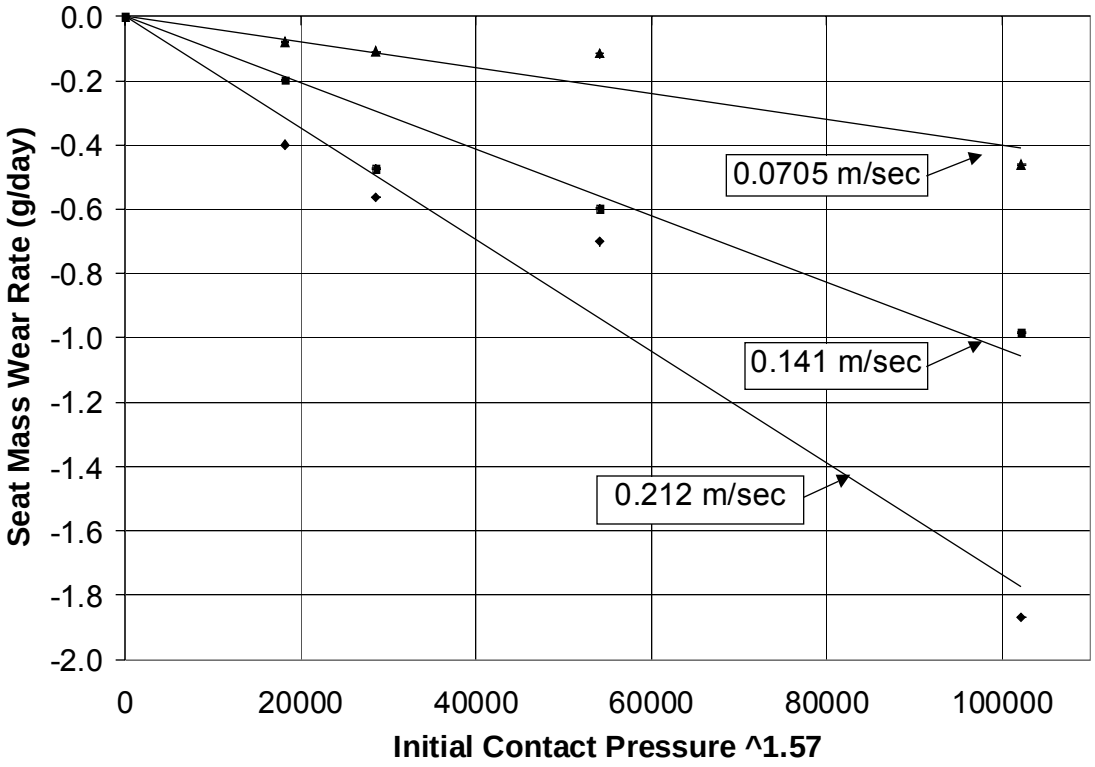

Figure 99: Mass Wear Rate of the 2012 XT Seat Sample as a Function of Contact Pressure Raised

to the Power of 1.57

The effect of contact velocity on the mass loss rate of the 2012 XT seat sample is shown in Figure 100. These results correspond to tests numbers M10 through M18 in Table 20. As seen in Figure 100, the mass loss rate on the stationary seat specimen is linear with time at a constant contact velocity, but non-linear over a range of contact velocities.

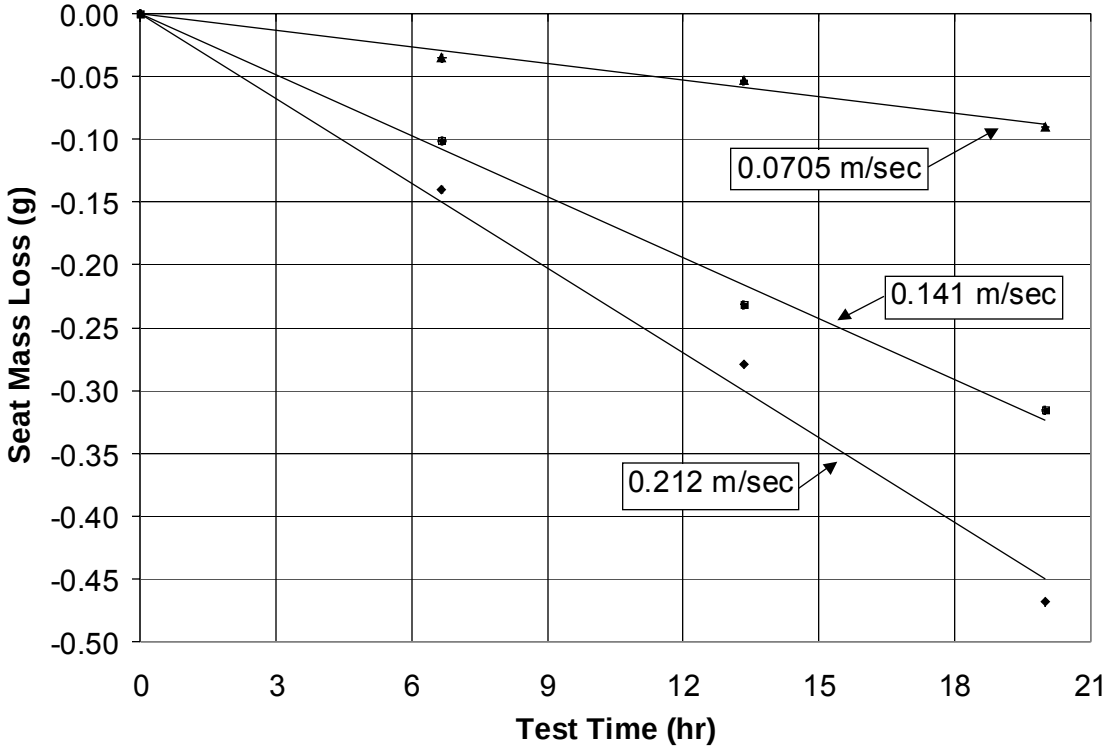

Figure 100: Effect of Contact Velocity Over Time on Mass Loss Rate of the 2012 XT Stationary Seat Sample

The fitted correlation relating seat specimen mass wear rate to the effects of contact pressure and contact velocity was in the form:

$$WR_{SM} = C_{SM} * P_C^{\alpha} * V_C^{\beta} \tag{31}$$

where α is the contact pressure correlation exponent for the seat specimen mass wear rate, β is the contact velocity correlation exponent for the seat specimen mass wear rate and C_{SM} is the proportionality constant for the seat specimen mass wear rate. The values determined for these constants were α = 1.57, β = 1.72 and $C_{SM} = -2.9*10^{-4}$. This relation is shown graphically in Figure 101. The final correlation for the seat specimen mass wear rate as a function of contact pressure and contact velocity was:

$$WR_{SM}\left[\frac{g}{day}\right] = -2.9*10^{-4} * \left[P_C\left[kPa\right]\right]^{1.57} * \left[V_C\left[\frac{m}{\sec}\right]\right]^{1.72} \tag{32}$$

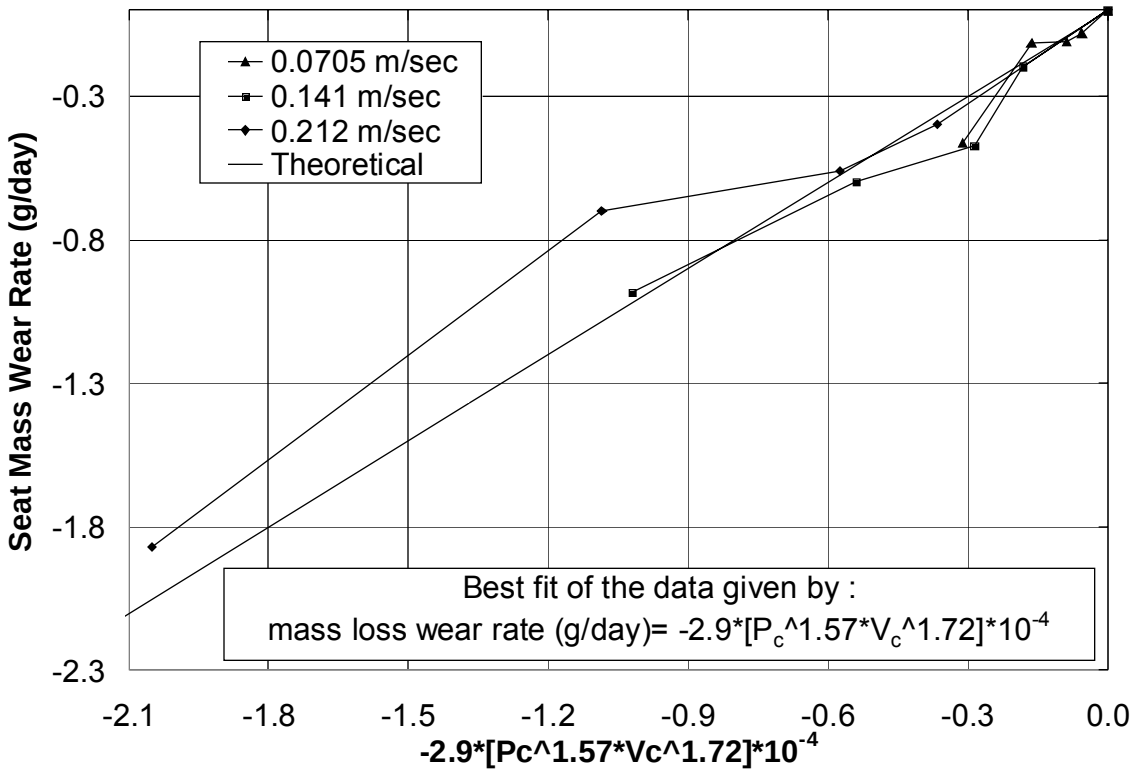

Figure 101: 2012 XT Seat Mass Wear Rate as a Function of Contact Pressure and Contact Velocity

With a correlation determined for the stationary seat specimen mass wear rate, the same type of correlation was constructed for the 2012 XT rotating ball specimens used in the tests in Table 20. The wear rate of the ball specimens could only be determined based on their mass lost during wear testing, due to the complexity of measuring the hemispherical wear surface for a linear wear rate. The mass wear rate of the ball sample, WR_B, was found using

$$Wear\ Rate\ (ball) = WR_B = \left(m_f - m_i\right)/t = \Delta m/t \tag{33}$$

Figure 102 shows the effect of contact pressure on the mass wear rate of the rotating ball sample, which appears to be a non-linear function. These tests are labeled as test numbers M1 through M9, M12, M15 and M18 in Table 20. This relation was fitted to a linear relation between contact pressure and mass wear rate of the ball sample to be: WR_B is proportional to $P_C^{1.66}$. This relation is shown in Figure 103.

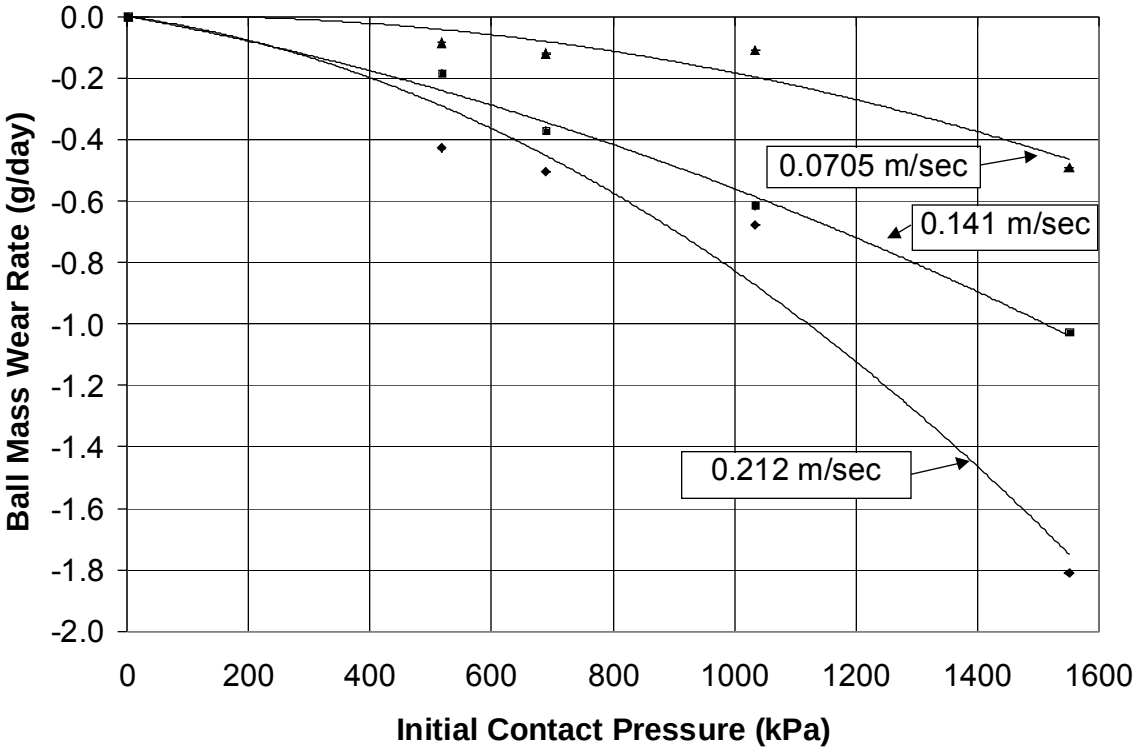

Figure 102: Effects of Contact Pressure on the 2012 XT Ball Sample Mass Wear Rate

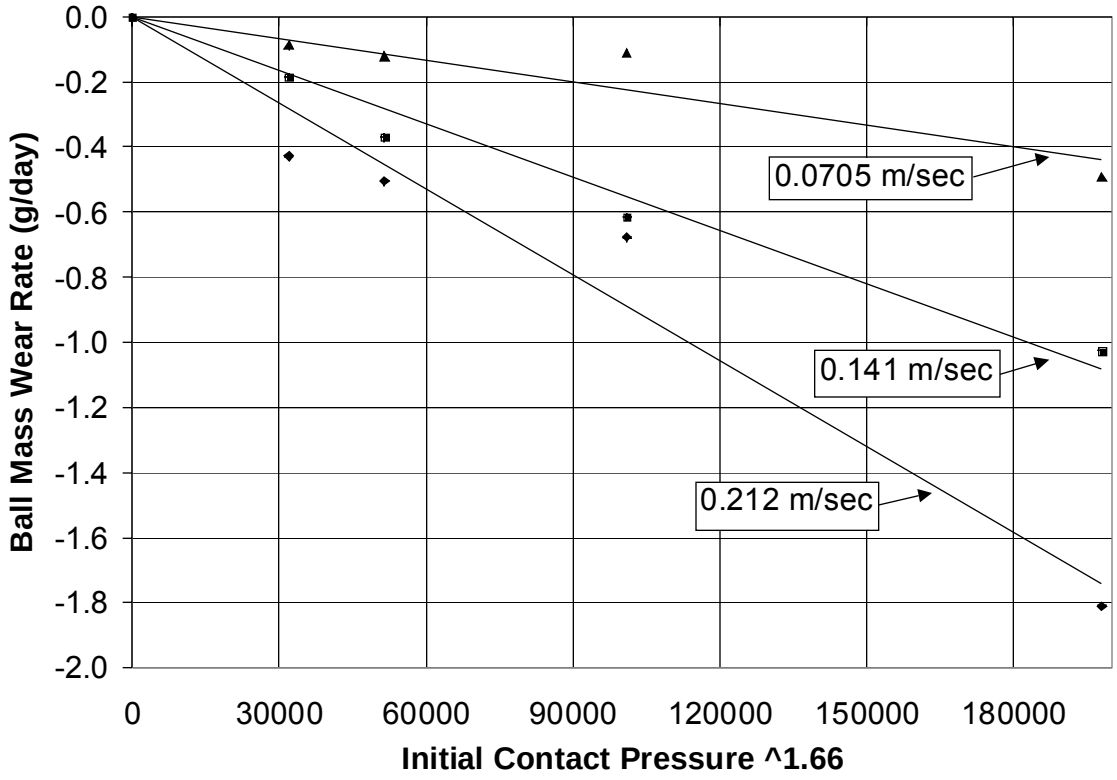

Figure 103: Mass Wear Rate of the 2012 XT Ball Sample as a Function of Contact Pressure Raised to the Power of 1.66

The effect of contact velocity on the mass loss rate of the 2012 XT rotating ball sample is shown in Figure 104. Tests were performed over constant time intervals at three different contact velocities at a constant contact pressure of 689-kPa and are labeled as test numbers M10 through M18 in Table 20. From Figure 104, the mass loss rate of the rotating ball sample is linear over time at a constant contact velocity, but non-linear over a range of contact velocities.

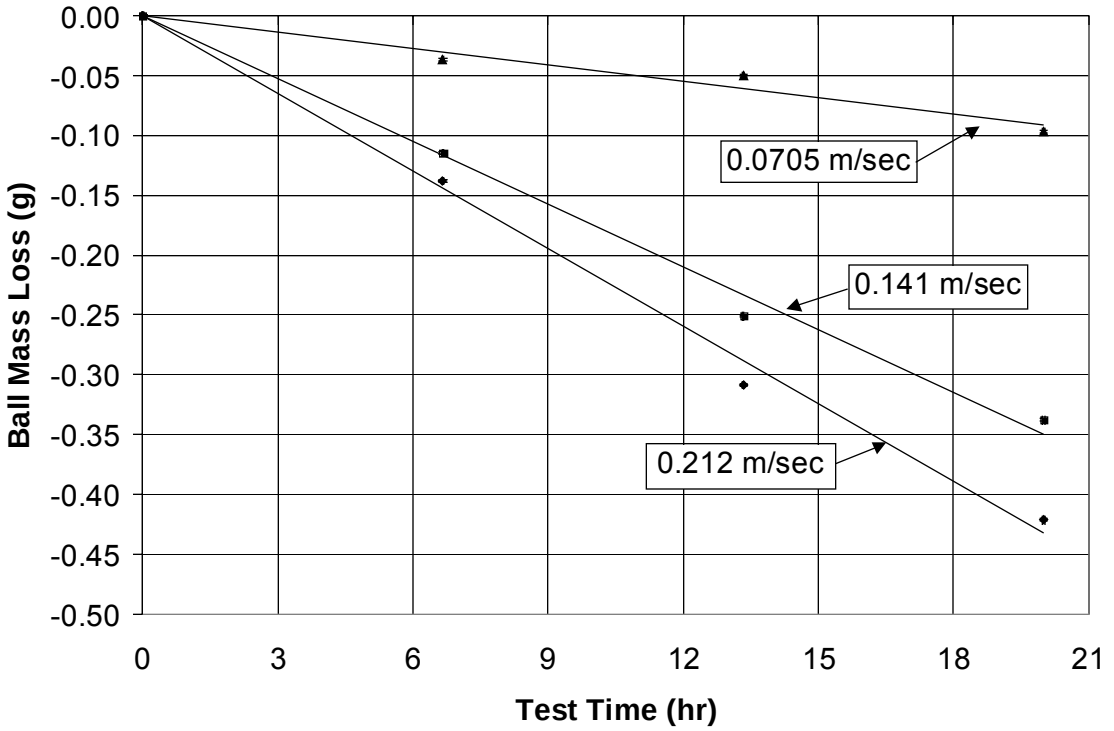

Figure 104: Effect of Contact Velocity Over Time on Mass Loss Rate of the 2012 XT Rotating Ball Sample

Using the above data for the mass wear rate of the 2012 XT ball sample, an overall correlation was derived between contact pressure and contact velocity as a function of mass wear rate. A correlation was applied of the form:

$$WR_B = C_B * P_C^{\alpha} * V_C^{\beta} \tag{34}$$

where α is the contact pressure correlation exponent for the rotating ball specimen mass wear rate, β is the contact velocity correlation exponent for the rotating ball specimen mass wear rate and C_B is the proportionality constant for the rotating ball specimen mass wear rate. The values determined for these constants were α = 1.66, β = 1.75 and $C_B = -1.6*10^{-4}$. This relation is shown graphically in Figure 105. The final correlation for the rotating ball sample mass wear rate as a function of contact pressure and contact velocity was:

$$WR_B\left[{}^{g}\!/_{day}\right] = -1.6*10^{-4} * \left[P_C\left[kPa\right]\right]^{1.66} * \left[V_C\left[{}^{m}\!/_{\sec}\right]\right]^{1.75} \tag{35}$$

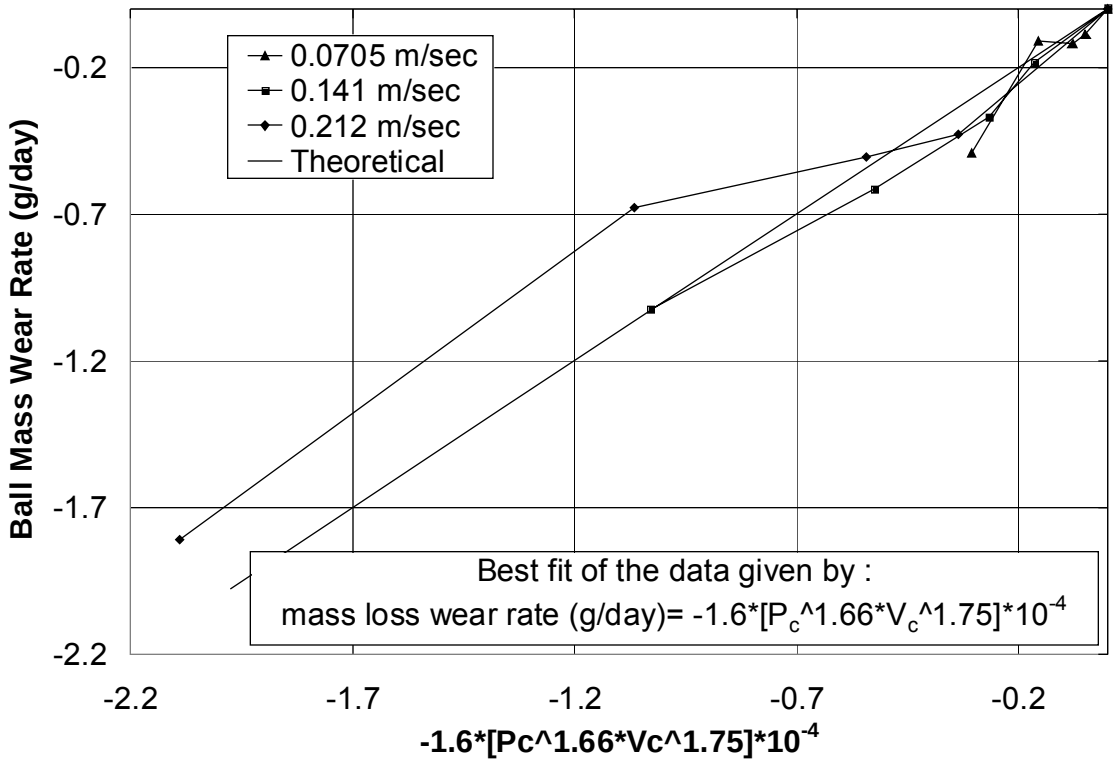

Figure 105: 2012 XT Ball Mass Wear Rate as a Function of Contact Pressure and Contact Velocity

An overall correlation for the wear pair, both rotating ball and stationary seat samples, was constructed using the mass wear rate of both the seat and ball samples. Both the stationary seat mass wear rate and rotating ball sample mass wear rate, found in Table 20, were added together to determine a mass wear rate for the wear pair, WR_{MP}. Figure 106 shows the mass wear rate of the wear pair as a function of contact pressure. The mass wear rate of the material pair is a non-linear function of the contact pressure, and a linear curve fit was applied to determine that mass wear rate of the material pair varies with $P_C^{1.64}$. The fitted linear relation between contact pressure and the mass wear rate of the material pair is shown in Figure 107.

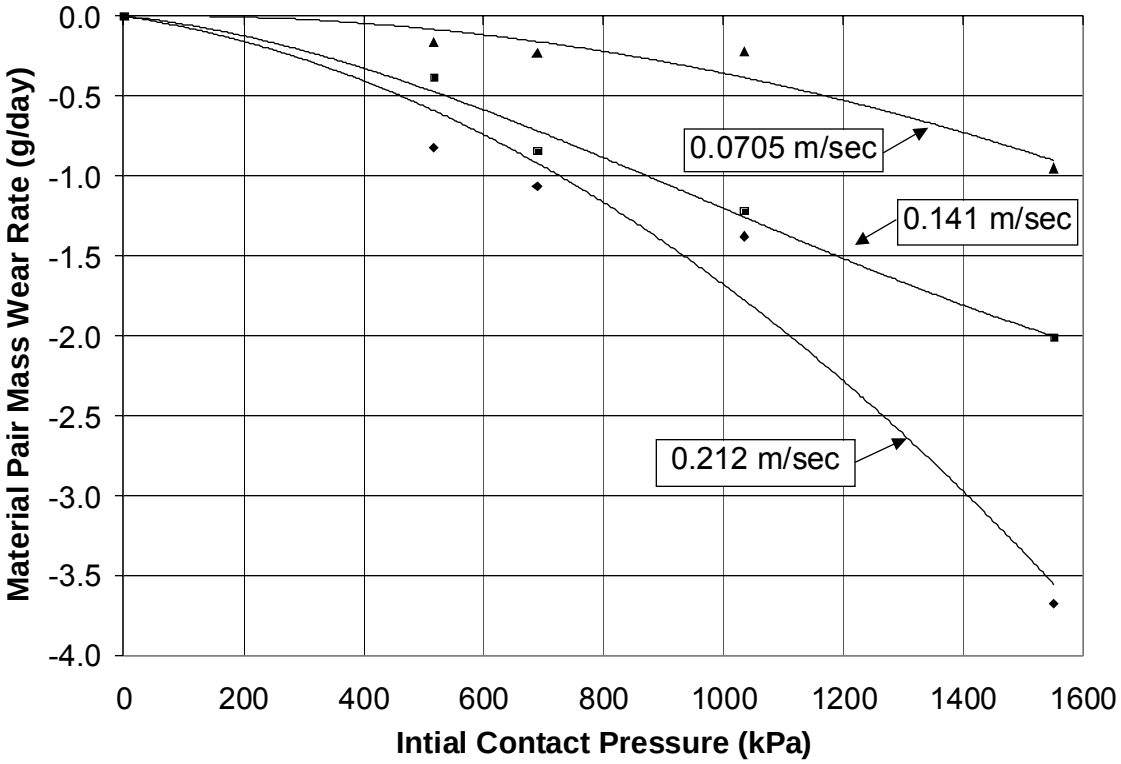

Figure 106: Effects of Contact Pressure on the Mass Wear Rate of the 2012 XT Material Pair

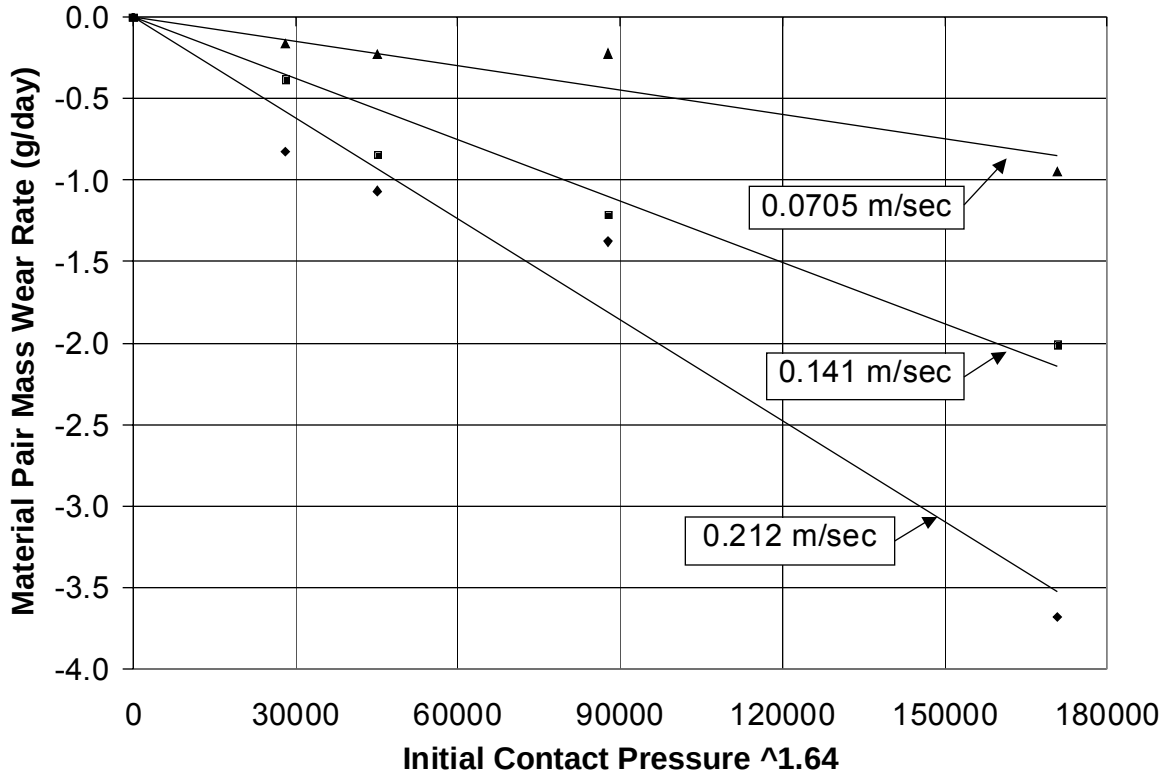

Figure 107: Mass Wear Rate of the 2012 XT Material Pair as a Function of Contact Pressure Raised to the Power of 1.64

The effects of contact pressure on the mass loss of the 2012 XT material pair over time is shown in Figure 108. These tests were performed at a constant contact pressure of 689 kPa and various contact velocities ranging from 0.0705 to 0.212-m/sec during three equal time intervals. From this Figure, it was evident that the mass loss of the material pair is linear over time with constant contact velocity, but non-linear over a range of contact velocities.

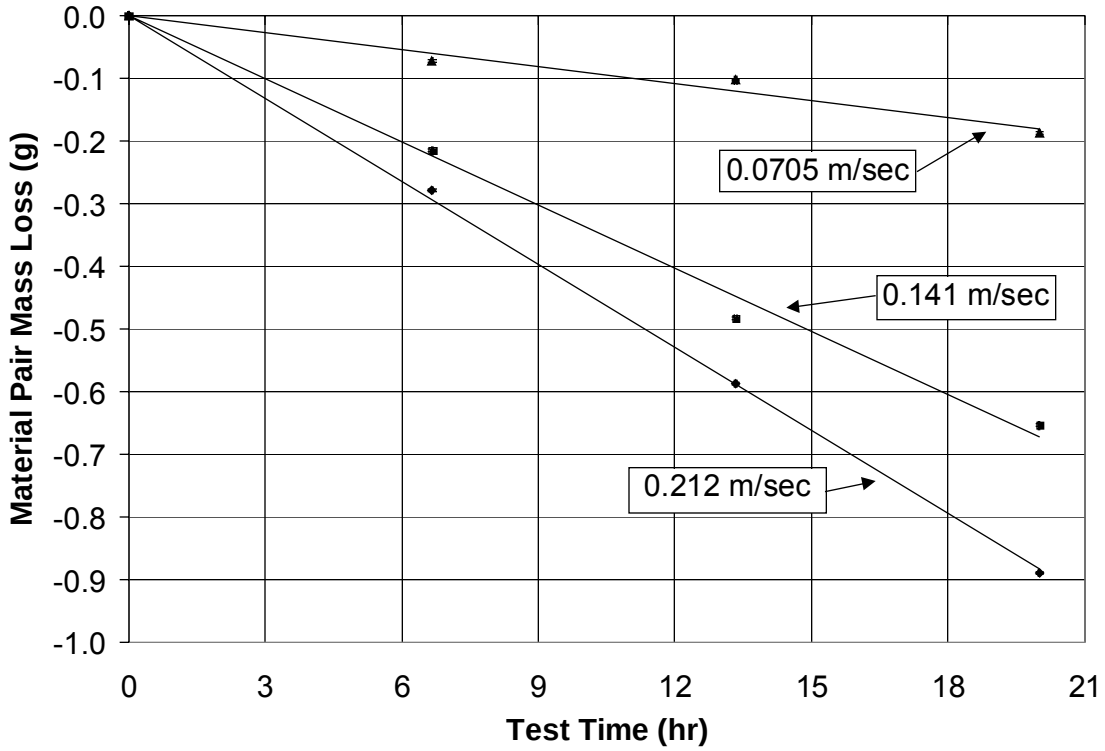

Figure 108: Effect of Contact Velocity Over Time on Mass Loss Rate of the 2012 XT Material Pair

Using the collected data for the mass wear rate of the 2012 XT material pair, an overall correlation for the mass wear rate of the material pair as a function of contact pressure and contact velocity was determined. The mass wear rate data was correlated and a fit was applied in the form:

$$WR_{MP} = C_{MP} * P_C^{\alpha} * V_C^{\beta} \tag{36}$$

where α is the contact pressure correlation exponent for the material pair mass wear rate, β is the contact velocity correlation exponent for the material pair mass wear rate and C_{MP} is the proportionality constant for the material pair mass wear rate. The values determined for these constants were α = 1.64, β = 1.70 and $C_{MP} = -3.4*10^{-4}$. This relation is shown graphically in Figure 109. The final correlated equation for the mass wear rate of the material pair as a function of contact pressure and contact velocity was:

$$WR_{MP}\left[{}^{g}\!/_{day}\right] = -3.4*10^{-4} * \left[P_C\left[kPa\right]\right]^{1.64} * \left[V_C\left[{}^{m}\!/_{\sec}\right]\right]^{1.70} \tag{37}$$

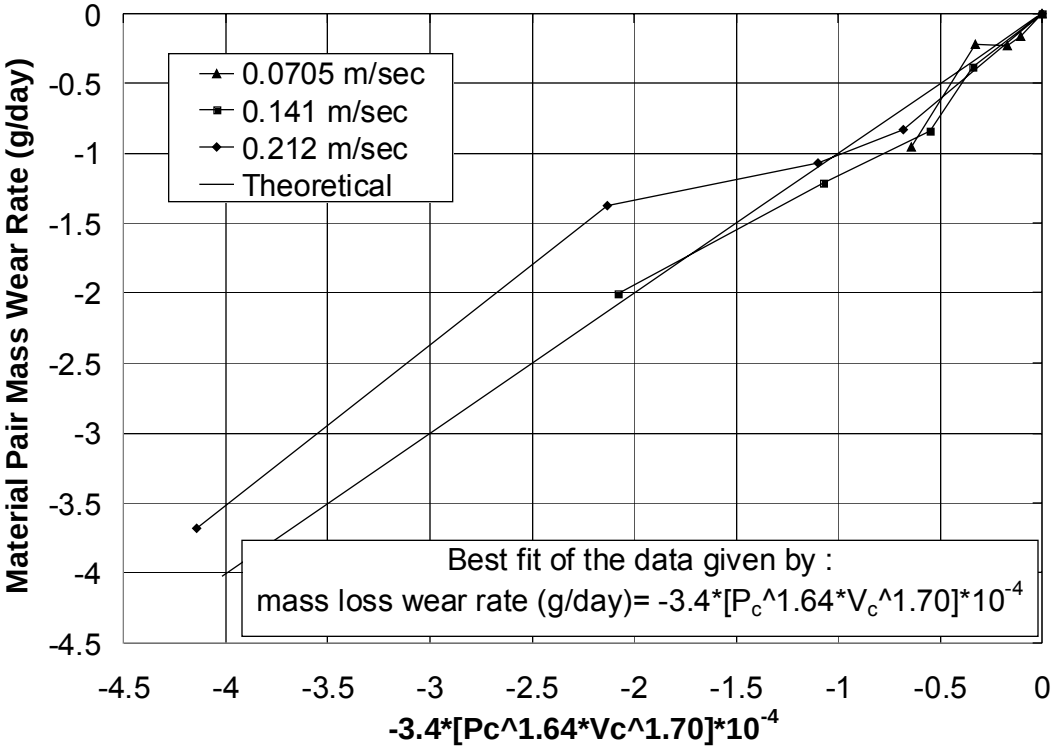

Figure 109: 2012 XT Material Pair Mass Wear Rate as a Function of Contact Pressure and Contact Velocity

For each test shown in Table 20, a sliding friction coefficient was calculated from the collected test data as outlined in Chapter 3. The collected friction coefficients for the contact pressure effects tests, test numbers M1 through M9, M12, M15 and M18 are shown in Figure 110 as a function of contact pressure at various contact velocities. As may be seen in this Figure, the sliding friction coefficients followed no trend as a function of contact pressure. Figure 111 shows the collected sliding friction coefficients for tests M10 through M18 as a function of time over various contact velocities. Once again, there appears to be no trend in the friction coefficient as a function of time at various contact velocities. The average friction coefficient based on test numbers M1 through M18 was 0.453. It appears that sliding friction coefficient follows no trend with contact pressure and contact velocity. Therefore, sliding friction coefficient was not incorporated into the correlations for wear rate as a function of contact pressure and contact velocity.

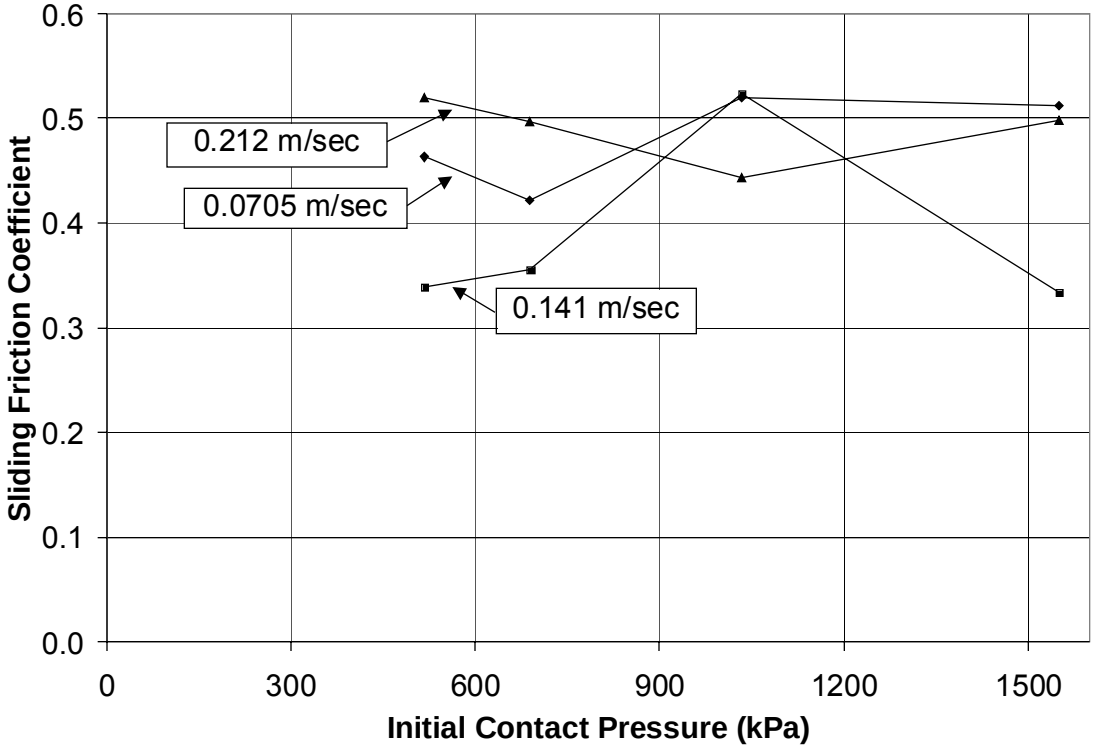

Figure 110: Sliding Friction Coefficient as a Function of Contact Pressure for 2012 XT

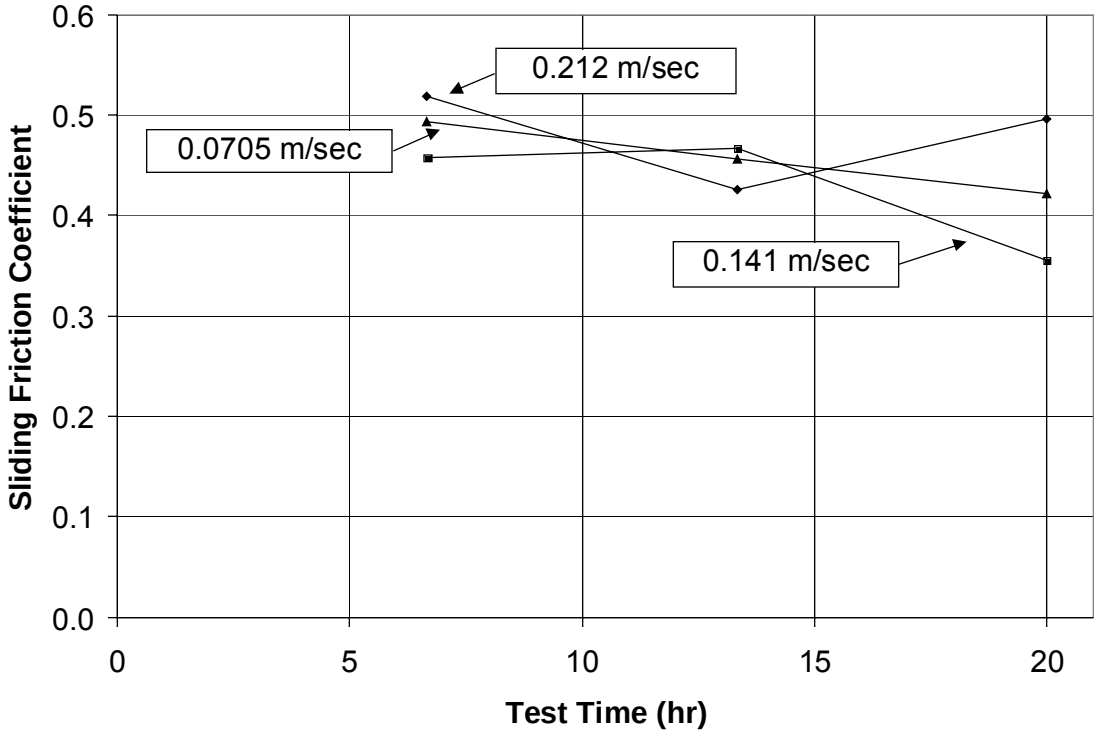

Figure 111: Sliding Friction Coefficient as a Function of Contact Pressure for 2012 XT

Sub-task 4.2.4 Series II Prototype-scale wear testing

The results of prototype-scale wear testing of series II material, Tribaloy-400 alloy, has been reported and compared with series I materials in the section of "Sub-task 4.1.4"

Sub-Task 4.3 Series III Testing

The following table details the materials selected for testing under Series III.

Series III Materials	Use
410 SS with T800 weld overlay	Bushing/sleeve material
410 SS with 2020 weld overlay	Bushing/sleeve material
316L SS with Aluminum weld overlay	Roll material

Table 21: Series II material table

Sub-task 4.3.1 Series III Lab scale corrosion testing

4.3.1 Series III Lab-Scale Corrosion Testing

Specimens were machined from the top, middle, and bottom part of the multiple pass weld of 2020 on type 316L. These specimens were tested in molten Zn-Al for 622 h. Figures 112 and 113 show two sides of the specimens removed from the Zn-Al both after 622-h exposure. These figures show that the specimens were the weld top were completely clean. However, the specimen from the middle and bottom of the weld had zinc stuck to them. Figures 114 and 115 showed the same specimens as shown in Figs. 112 and 113 after acid cleaning. It is to be noted that the middle sample had some part of the base metal on its one side. Similarly, the sample from the bottom had weld interface on its one side.

The weight change data on top, middle, and bottom samples from duplicate tests is plotted in Fig. 116. Data is also compared with monolithic 2020 and type 316L data. It is clear from this figure that the top of a multiple pass weld overlay of 2020 on type 316L can match the corrosion performance of a monolithic specimen of 2020. In addition to excellent corrosion performance, the multiple pass welds also shows good hardness value, which should perform well in wear conditions.

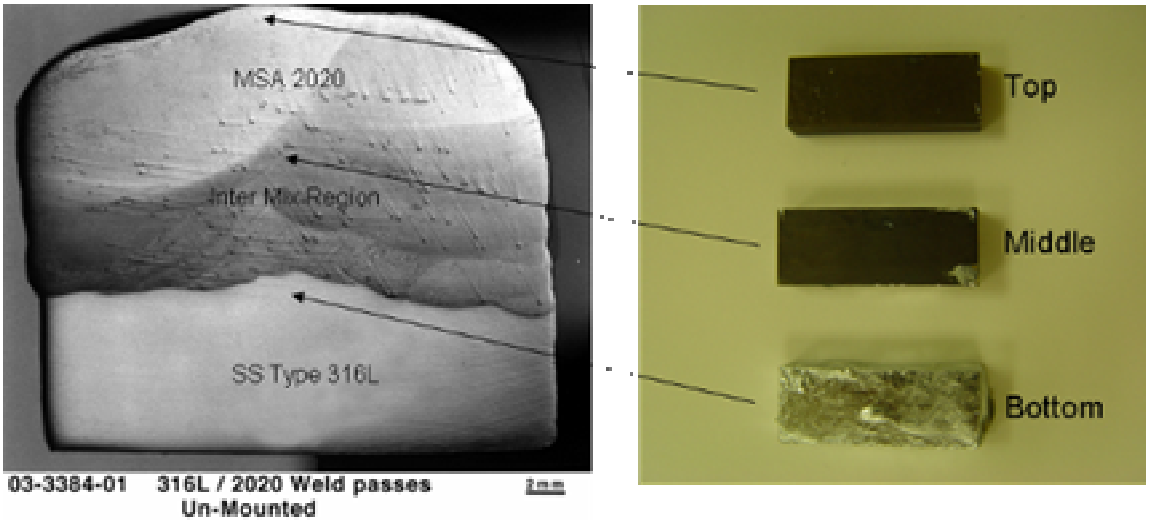

Figure 112: Top surfaces of multiple pass weld overlay samples of 2020 on stainless steel type 316L after 622 h in molten Zn-Al alloy at 465°C.

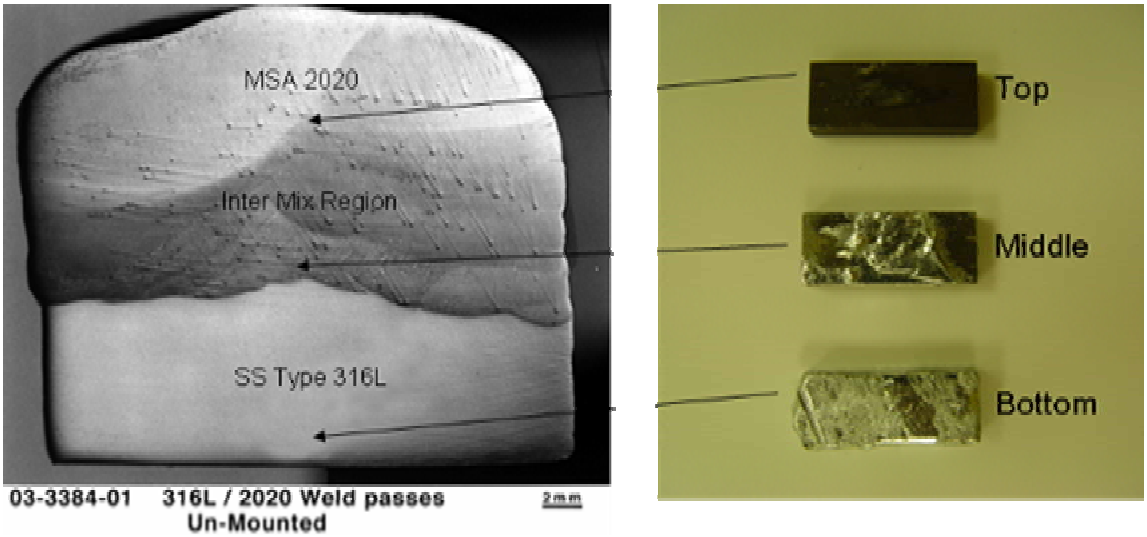

Figure 113: Bottom surfaces of multiple pass weld overlay samples of 2020 on stainless steel type 316L after 622 h in molten Zn-Al alloy at 465°C.

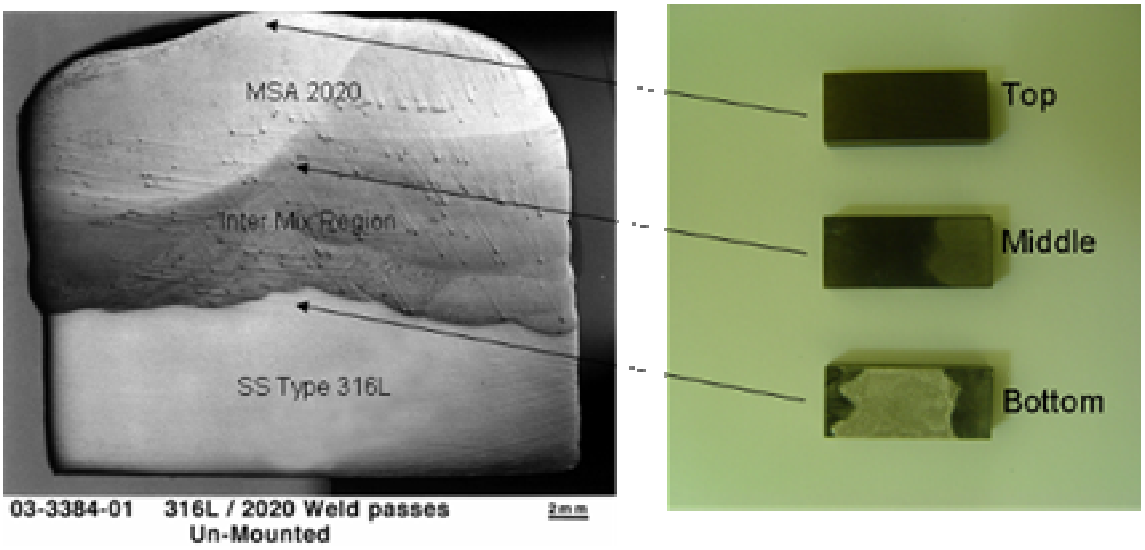

Figure 114: Top surface of multiple pass weld overlay samples of 2020 on stainless steel type 316L after 622 h in molten Zn-Al alloy at 465°C and after acid cleaning.

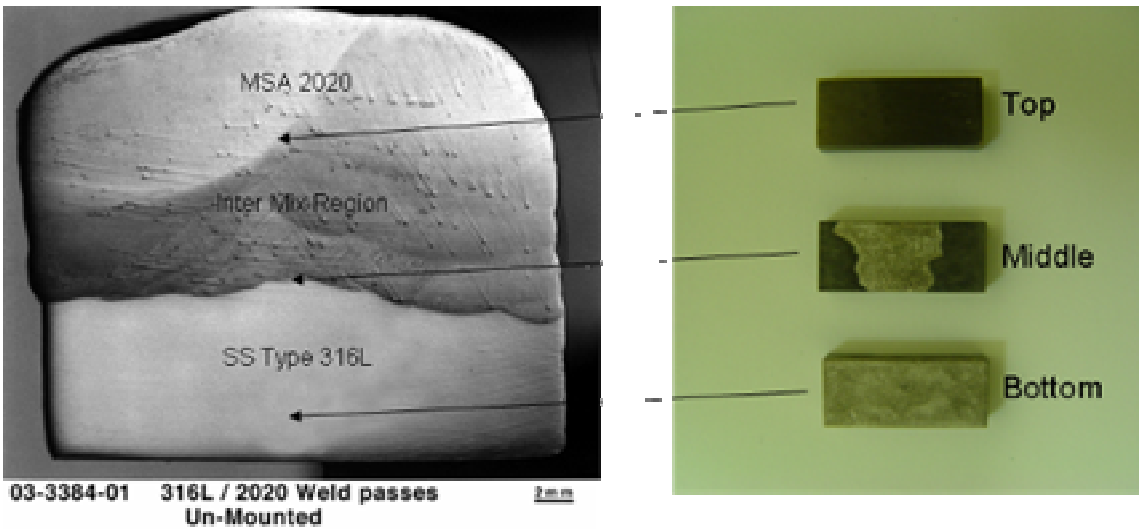

Figure 115: Bottom surfaces of multiple pass weld overlay samples of 2020 on stainless steel type 316L after 622 h in molten Zn-Al alloy at 465°C and after acid cleaning.

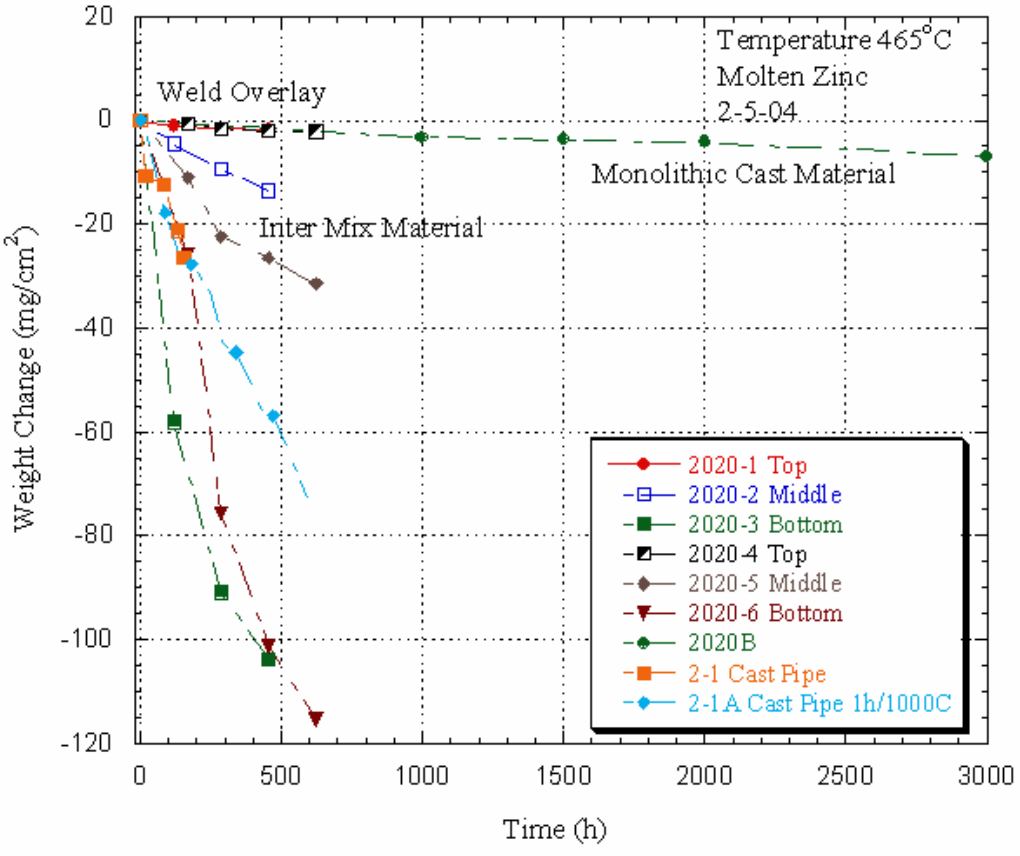

Figure 116: Multiple pass weld overlay of 2020 on stainless steel type 316L weight change vs. time plot.

Sub-task 4.3.2 Series III In-plant corrosion testing

Because of the difficulty in processing materials for in-plant testing, the section was unable to be effectively completely. Further developments will be made in the ongoing "Multifunctional Metallic & Refractory Materials for Energy Efficient Handling of Molten Metals" project, currently funded by DOE.

Sub-task 4.3.3 Series III Lab-scale wear testing

Material in this section is under patent application according to DOE case No. S-102,679.

The wear resistance of existing and new material combination for hot dip galvanizing line zinc pot roll bearings has been completed under this contract by Dr. John Loth and his PhD student James M. Snider II, who completed his dissertation[1] in December of, 2004. Dr. Snider collected zinc-pot wear and friction coefficient data on bearing material combinations provided by our industrial vendors, see Ref. 2. Snider used a laboratory scale zinc pot bearing material wear tester[3], developed at WVU for that purpose. Wear data are now available as a function of contact pressure and velocity for most commercially available zinc pot bearing material pairs. This vast amount of available wear data does not provide a simple answer to the operator on what bearing material to use for his or her specific application. The cost and performance of these bearing materials varies a great deal. Therefore their cost effectiveness becomes a complex function of pot chemistry, operating temperature, bearing surface contact pressure, contact velocity and preferred overhaul schedule. Most zinc pot bearing materials, share unique wear rate characteristics, which is that wear increases drastically with contact pressure, vibrations and misalignments but less so with contact velocity.

Most materials demonstrated a wear rate increasing with contact pressure as P_c^{α}, where the coefficient α ranged between 1.4 and 2, and with contact velocity as V_c^{β}, where the coefficient β was on the average equal 0.5. Reducing bearing contact pressure by a factor of 3 with $\alpha = 1.5$ may extend bearing life $3^{1..5}$ or 5 fold.

The currently used zinc pot roll has short-cantilevered shafts (length about equal diameter) welded to each end. Shaft diameter is small, ranging from 3" to 4", to minimize bearing friction torque relative to the roll driving torque provided by the sheet-roll contact friction. This is required to avoid roll stoppage. These shafts are short, ranging in length from about 4" to 5", to limit the root bending moment and the risk of the shaft breaking off.

Stabilizer rolls are about 8" in diameter and the larger sink rolls about 20" in diameter. Sometimes these rolls are used not only to guide the sheet through the zinc pot but also to control line tension and for sheet steering. These functions add significantly to roll bearing wear, as it locally increases contact pressure and cause bearing miss-alignment. In general bearing housings are welded rigidly to the roll hangar, which increases vibrations and adds to the wear problem. To prevent roll stoppage associated with bearing seizure, the bearing/shaft clearance is sometimes intentionally increased to about 0.5". This practice results in shaft/bearing line contact instead of surface contact,

which increases contact pressure and wear rate.

An order of magnitude increase in bearing life is possible with the WVU patent pending: "Bearing Life Extender for Conveyor Type Rollers." Its objective is to allow an increase in bearing length, for lower contact pressure, without increase in shaft diameter, bending moment or internal stress. Further it assures bearing alignment at all times and minimizes vibrations. To show how this is possible, the relationship between bearing load F, maximum bending moment M_{max} and shaft deflection y_{max} are shown below for three different configurations.

1) Rotating shaft of length L_1 supported from only one side, and thus cantilevered.
2) Non-rotating shaft of length L_2 rigidly supported from one side and with a simple support on the other side.
3) Non-rotating shaft of length L_3 rigidly supported on both sides.

The load per unit length is given by w. Then bearing of length L supports load: F = wL .

1) Cantilevered rotating shaft of length L_1:

$$M_{\max} = \frac{FL_1 = w_1 L_1^2}{2} \text{ and maximum deflection } y_{\max} = \frac{FL_1^3 = w_1 L_1^4}{8E.I}$$

2) Simple support at one end L_2:

$$M_{\max} = \frac{FL_2 = w_2 L_2^2}{8} \text{ and max. deflection } y_{\max} = \frac{FL_2^3 = w_2 L_2^4}{185E.I}$$

Rigidly supported on both ends of length L_3:

$$M_{\max} = \frac{FL_3 = w_3 L_3^2}{12} \text{ and max. deflection } y_{\max} = \frac{FL_3^3 = w_3 L_3^4}{384E.I}$$

The maximum tensile stress σ_{max} is proportional to the maximum bending moment M_{max} times radius D/2 and divided by moment of inertia I = pi*D^3/64 . Or $\sigma_{\max} = \frac{M_{\max}.D}{2I}$.

Replacing a conventional roll with its cantilevered bearings by a fixed shaft roll, enables one to increase the bearing length L significantly without increasing the maximum shaft bending moment M_{max} or maximum stress σ_{max}. This reduces bearing contact pressure and wear rate resulting in increased bearing life. Below is a comparison of bearing length L for same bearing load F and maximum bending moment M_{max} .

$\frac{L_1}{2} = \frac{L_2}{8} = \frac{L_3}{12}$ or $\frac{L_2}{L_1} = 4$ and $\frac{L_3}{L_1} = 6$. Increase in bearing length reduced contact pressure by: $\frac{p_2}{p_1} = \frac{1}{4}$ and $\frac{p_3}{p_1} = \frac{1}{6}$. Assuming bearing wear rate R proportional to $P_c^{\alpha = 1.5}$ then : $\frac{R_2}{R_1} = \left(\frac{1}{4}\right)^{1.5} = \frac{1}{8}$ and $\frac{R_3}{R_1} = \left(\frac{1}{6}\right)^{1.5} \cong \frac{1}{14}$.

Next compare bearing length L for the same bearing load F and maximum shaft deflection y_{max}, then the allowable increase in length is lower and given by:

$\frac{L_1^3}{8} = \frac{L_2^3}{185} = \frac{L_3^3}{384}$ or $\frac{L_2}{L_1} = \left(\frac{185}{8}\right)^{1/3} = 2.8$ and $\frac{L_3}{L_1} = \left(\frac{384}{8}\right)^{1/3} = 3.63$ and bearing wear rate R proportional to $\frac{R_2}{R_1} = \left(\frac{1}{2.8}\right)^{1.5} \cong \frac{1}{5}$ and $\frac{R_3}{R_1} = \left(\frac{1}{3.63}\right)^{1.5} \cong \frac{1}{7}$

Thus a fixed shaft roller can significantly increase bearing life by reducing the contact pressure without increase in deflection or bending moment. There are several additional advantages of using a fixed shaft roller over the conventional configuration.

1) By welding the bearing housing inside the roll ends, their alignment is assured under all loading conditions, even during sheet steering, when pushing harder on one end of the roll.
2) No need to weld bearing assembly to roll hangar, therefore reducing the transmission of vibrations from hangar to roll.
3) A fixed shaft does not suffer from flexing fatigue like a rotating shaft.
4) Depending on the increase in bearing length used, shaft deflection is reduced
5) Holes drilled inside the rotating bearing housing can act as a centrifugal pump causing zinc to flow out radially outward thereby cooling the bearing surfaces and flushing out dross and loosened hard wear particles.
6) By using the bearing inserts to serve both as radial and thrust bearing eliminates the need for the conventional roll type thrust bearing buttons.
7) In general the roll is non-buoyant, and a large clearance in the bearings can make a conventional roll stop as gravity wants it to turn into the direction opposite to that produced by the upward pull of the sheet. This can lead to roll stoppage and premature need for roll replacement. However the WVU patent pending fixed shaft roll with large clearance has gravity wanting it to turn in the same direction as produced by the upward pull of the sheet, thereby minimizing roll stoppage problems.

The patent pending fixed shaft roll must be fully assembled in a shop and when hung into the U shaped openings of the hangar arms will only need to be prevented from rotating or falling out. This is readily achieved by welding on two retainer plates thereby speeding up time required for roll exchange.

A proposed fixed shaft stabilizer roll is shown in Figure 117 with its components listed in Table 22. Figure 118 is an end view of the assembled roll, which was drawn by graduate student Vishnu Rachamalla. Within the roll ends are welded bearing housings, each of which contains five ACD Wearguard ceramic inserts measuring 5"x1.25"x1". In the future the bearing length may be doubled. The fixed shaft-end bearing sleeves are to be laser clad with a 50-mil thick layer of tungsten carbide. Steel partner D has expressed great interest in an on-line trial of the new fixed shaft stabilizer roll.

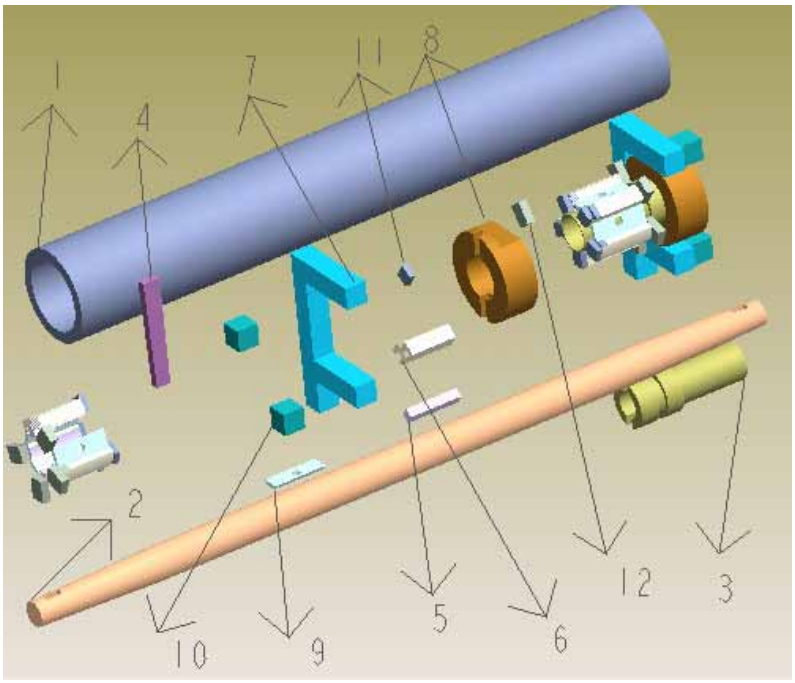

Figure 117: Exploded view of components making up a fixed shaft stabilizer roll

Part #	Description
1	Stabilizer roll 8" OD x 6" ID x 59.5" long
2	Fixed Shaft 3" ODx 72" long
3	Tungsten Carbide Coated shaft sleeve
4	Tapered Assembly retainer key 1" thick by 10" long
5	Vesuvius ACD Wearguard ceramic inserts 5"x1.25"x1"
6	Ceramic insert holders
7	Roll support hangar
8	Shaft collar made to fit hangar opening
9	Spacers for ceramic inserts
10	Retainers welded to hangar to lock shaft in place
11	Retainers to weld bearing housing to roll
12	Retainers to secure ceramic inserts in holders

Table 22: Roll parts list

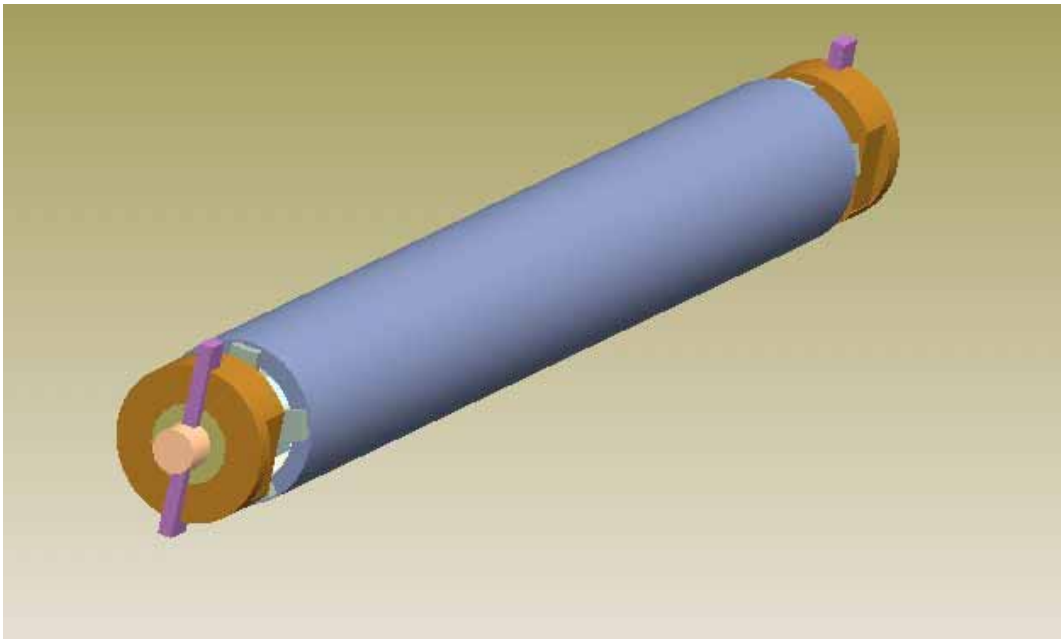

Figure 118: End view of stabilizer roll

Series III Prototype-scale wear testing

Since Series III materials development focuses on developing materials/coatings for dross resistance sink rolls and stabilizer rolls, it is not necessary to conduct the prototype-scale wear testing of these new materials.

Task 5 In-plant Testing and Trials

Sub-Task 5.1 Component testing

Trial of 2012 XT bearings at steel partner A

Component line trials are a culmination of research performed in the IMPH project to study the mechanisms of wear, corrosion, and dross buildup on materials tested under laboratory scale conditions at WVU and ORNL. From small-scale and prototype-scale testing, wear and corrosion measurements of various candidate materials have been made. WVU, ORNL have worked with steel partner A to conduct the trial of 2012 XT bearings as the sink roll and stabilizer roll bearings. The details of the trial are listed as following:

- Starting date: 04/26/05
- End date: 05/12/05
- Bath chemistry (average): 0.18% Al
- Bath temperature: 865 F
- Line speed (average): 430 fpm
- Total length of steel strip: 8,034,724 feet

Figure 119: Shaft/bearing assembly after trial at steel partner A

Figure 120: 2012 XT Stabilizer roll bearing after 16 days trial at steel partner A

Figure 121: Stellite 6 bearings after service.

Figure 119 shows the shaft/bearing assembly after the 16-day trial at steel partner A and figure 120 shows the close-up snapshot of the 2012 XT bearing itself. There have been 8,034,724 feet of steel strip passed through the galvanizing bath during the trial, which is more than twice of the conventional Stellite 6 bearing's service life. Figure 121 shows the conventional Stellite 6 bearings after one campaign. It is indicated that there are deep worn scratch on the Stellite bearing, as compared to the smooth surface of the 2012 XT bearing.

The detail examination of the bearing shows that only less than 1/3 of the total thickness of the 2012 XT bearing was worn after the trial, as compared to the Stellite 6 bearings were totally worn through after one campaign, which means that the bearing can be re-used two more times, to triple the service life of the bearing. Therefore, it is safe to conclude that as one of the results of this IMPH project, the newly 2012 XT bearings have **at least six times of the service life** than the conventional Stellite 6 bearings.

Task 6 Meetings and Reports

Sub-Task 6.1 List of presentations, publications, and patents

Conference Papers

Liu, Y.H., Tang, N-Y, Zhang, L., Denner, S.G. and Goodwin, F.E., "Dross Formation and Control During Transitions from Galvannealing to Galvanizing, " Proc. 44th Mechanical Working and Steel Processing Conference, Orlando, FL, Sept. 9-11, 2002, Iron & Steel Society, Warrendale, PA.

Goodwin, F.E., Chang, K-M and Sikka, V., "Development of a New Generation of Bath Hardware Materials," Galvanizers Assn. 94th Meeting, October 20-23, 2002, Dearborn, MI.

Barbero, E., Irwin, C., Liu, X., Sikka, V., and Goodwin, F.E., "Development of the Next Generation of Bath Hardware Materials", 2003 AISE Annual Convention, Pittsburgh, PA, October 1, 2003

Parthasarathy, V., Kang, B., Huet, K., Krishnaswamy, A., Barbero, E., Chang, K-M, Irwin C., and Goodwin, F.E., "Long-Term Performance of Pot Hardware on Continuous Galvanizing Lines", Proc. of Galvatech 04, Chicago, IL, April 4-7, 2004, Association for Iron & Steel Technology, Warrendale, PA.

Barbero, E.G., Liu, X., Loth, J., Snider, J., Damiani, T.M., Sikka, V.K., and Goodwin, F.E., "Current Research on Zinc Pot Hardware and Molten Metal Containment," Proceedings of Galvanizers Association 96th Annual Meeting, Charleston, SC, October 3-6, 2004.

Liu, X., Barbero, E., Irwin, C., V. Sikka, V., Hemrick, J., Headrick W., & Goodwin, F.: "Development of Next Generation of Metallic and Refractory Materials for Molten Metals Handling", AISTech 2005 Iron & Steel Technology Conference and Exposition,

Charlotte, NC

X. Liu, Barbero, E., Goodwin, F.: Progress on Improved Materials for Pot Hardware Project, in Galvanized Autobody Partership 2004, Charleston, SC

X. Liu et al.: "Corrosion of Several Alloys in Industrial Hot-dipping Baths", in Galvtech' 04, Chicago IL, ISS, 2004

Snider, J.M., Loth, J., Barbero, E., Kamil, R., Zinc-Pot Bearing Material Wear-Test Results Using the WVU Small-Scale Tester, Galvatech'04, Chicago 2004

Barbero, E. J., Sikka, V. and Goodwin, F. Performance Evaluation of Current Hot-dip Pot Hardware Materials, Galvanizers Association Annual Meeting, Monterrey, Mexico, October 2003.

Snider, J. M. II, "Zinc Pot Bearing Material Wear and Corrosion Characterization", PhD Dissertation, West Virginia University, Morgantown, WV, December 2004.

Snider, J. M. II and Loth J. L. "Empirical Wear Rate Modeling of Zinc Pot Bearing Materials Using the WVU Small-Scale Tester," Galvatech '04 Conference Chicago Il, April 2004.

Loth, J. L. "Zinc-Pot Roll Bearing Design Modification for Increased Life," Galvatech '04 Conference Chicago Il, April 2004.

Journals

Barbero, E.G., Irwin, C., Liu, X., Sikka, V., and Goodwin, F.E., "Development of the Next Generation of Bath Hardware Materials," Iron and Steel Technology, October 2004, pgs. 31-37.

Liu, X., Burris, M., Chang, K-M., Barbero, E.G. & Sikka, V.: "Liquid Metal Corrosion of 316L, Fe3Al and FeCrSi in Molten Zn-Al Baths", Metallurgical & Materials Transactions, Vol. 33A 2005, pgs. 2049-2058

Loth, J. L., Morris G. J. and Ware R. "Design Aspects of a New Material Wear Tester," Materials Characterization, WIT Press 2004, ISBN 1-85312-988-7

Patents

U.S. Patent Pending,# 0/695551-102803. "Bearing Life Extender for Conveyor Type or Zinc Pot Roll" DOE Case No. S-102,679 – Disclosure No. 193